Doctor of Philosophy Thesis

First principles study on effective on-site Coulomb interaction from linear response approach and application to metal complexes

Kenji NAWA

MIE UNIVERSITY

Graduate School of Engineering

Division of Materials Science

September 2017

Doctor of Philosophy Thesis

First principles study on effective on-site Coulomb interaction from linear response approach and application to metal complexes

線形応答理論による有効オンサイトクーロン相互作用の第一原理計算と金属錯体への応用

Kenji NAWA

MIE UNIVERSITY

Graduate School of Engineering

Division of Materials Science

September 2017

Abstract

In investigations on electronic structures of correlated materials such as transition-metal oxides, rare-earth compounds, and organometallic molecules, first-principles calculations based on density functional theory (DFT) play a central role. However, there is a problem remaining to deal with correlation effects in the DFT for correlated materials. On a practical level, DFT+U method that introduces Hubbard-model parameters to represent screened on-site Coulomb (U) and exchange (J) interaction is one of the powerful and conventional tools suitable for calculations of large systems without expensive costs. The values of U and J are commonly chosen to match experimental observations, but optimal values depend on which exchange-correlation functional is used and the calculated material properties are very sensitive to values of on-site U and J even in the ground state. More recently the parameters have been calculated directly from first-principles calculations, but they vary over wide ranges of values even for the same ionic state in a given material. Unfortunately, this implies that choosing "good" values is problematic.

In order to address this issue, here, non-empirical method for deriving scaled $+U$ parameters is developed and applied to the prototypical materials of correlated transition-metal monoxides and organometallic molecules. This dissertation consists of five chapters. After an introduction to electronic structures of correlated materials and general failures of the DFT-based first-principles calculations in chapter one, methodologies of the DFT and linear response approach to estimate an effective on-site Coulomb interaction, U_{eff}, of correlated elements are described in chapter two, where the U_{eff} values determined from the second derivative of the total energy with respect to the occupation numbers of localized d-electrons within the linear response theory. All calculations were carried out by means of the all-electron full-potential linearized augmented plane wave (FLAPW) method. Chapter three devotes to an application of this approach to the transition-metal monoxides, TMO (TM = Mn, Fe, Co, and Ni), where the variation of U_{eff} values by changing the muffin-tin (MT) sphere radius was examined. It is found that the U_{eff} value depends strongly on MT sphere size by more than 2 3 eV in all systems, for example, in MnO when the MT radius is 2.0 bohr, the U_{eff} value results in 10.1 eV but it decreases to 7.2 eV as the MT radius increases to 2.7 bohr. The same trend in the Ueff values was confirmed in other considered oxide systems. However, despite this large variation, essentially identical valence band structures are obtained, and I found an approximate scaling

of U_{eff} with regard to size of MT sphere. Thus, although simple transferability of the U_{eff} value among different calculation methods is not allowed, guidelines for estimating U_{eff} are proposed.

In chapter four, this approach was applied to ground-state electronic structure calculations of correlated organometallic metallocens, $TMCp_2$ (TM = V, Cr, Mn, Fe, Co, and Ni). In these complexes, however, an additional difficulty intrinsically related to various electronic configurations of d electrons that nearly degenerate is raised, which may numerically trap in one of multiple local energy minima corresponding to meta-stable electronic configurations, instead of a global minimum of the ground state. The changes due to the presence of the ligand field of molecules further complicate theoretical analysis so that the DFT+U calculations may fail to search a ground-state electronic configuration truly. To overcome this problem, I implemented the constraint DFT+U approach that controls electronic configurations by introducing Lagrange multipliers to the d electron density matrix. Thus, the total energies of all electronic configurations allowed by a symmetric group were calculated self-consistently with the Lagrange multipliers and then the ground electronic configuration was energetically determined. The predicted results demonstrate precisely the experimentally observed grand-states, i.e., $^4A_{2g}$, $^3E_{2g}$, $^6A_{1g}$, $^1A_{1g}$, $^2E_{1g}$, and $^3A_{2g}$ for VCp_2, $CrCp_2$, $MnCp_2$, $FeCp_2$, $CoCp_2$, and $NiCp_2$, respectively, while the stability between different electronic configurations is found to be very sensitive depending on the U_{eff} values. Thus, an utility of constraint DFT+U method combined with non-empirical U_{eff} values for analyzing properties of correlated systems was demonstrated.

Chapter five concludes the thesis that by using the proposed methodology opens a new avenue toward reliable predictions of structures and physical properties in strongly correlated metal complexes and gives suggestions for future calculations.

Acknowledgements

I would like to express my special deepest appreciation to my supervisor, Professor Kohji Nakamura at Department of Physics Engineering, Mie University. You have been a tremendous mentor for me for over five years since I started research activities as one of your group members. I would like to thank you for encouraging my research and for allowing me to grow as a physics researcher. You took me to many workshops and conferences in various fields, and gave me opportunities to get acquainted with researchers. I believe my research community has been extended, and thanks to you, I have collaborated with people of other research institutions. Without your persistent help, my publications and this dissertation would not have materialized. Your advice on both research as well as on my career and life have been priceless.

My heartfelt appreciation goes to Professors Tomonori Ito and Toru Akiyama for constant supports, guidance, and suggestions. For five years, they always encouraged me mentally. I would like to thank my colleagues, Koichi Hayashi, Toshio Sakai, Katsuya Masuda, Aiichiro Sugiyama, Yushi Ikeura, Shohei Takeda, Takahiro Ito, Kento Yamamoto, Kohei Nozaki, Takahiro Nomura, Keisuke Mobayashi at Nano-design laboratory, Department of Physics Engineering, Mie University, and Dr. Abdul-Muizz Tri Pradipto at Institute for Chemical Research (ICR), Kyoto University. I would like to express my gratitude to committee members for the peer review of this dissertation, Professors Ito, Nakamura, and Kazuhiro Sano, at Department of Physics Engineering, and Professor Kazumasa Hiramatsu at Department of Electrical and Electronic Engineering, Mie University. Suggestions and discussions from you were insightful and valuable moments.

Most of my research were done in collaborations. Dr. Yukie Kitaoka at Spintronics Research Center, National Institute of Advanced Industrial Science and Technology (AIST), has told and shown me a lot of things every time when, for example, discussing results, practicing presentations, writing abstracts and papers. I appreciate Dr. Hiroshi Imamura at AIST for giving insightful comments and advice for one of my publications. I would like to express my gratitude to Professor Tamio Oguchi at The Institute of Scientific and Industrial Research (ISIR), Osaka University, for his continuing support, suggestions, encouragement, and financial helps. Whenever I visit his group and talk my research progress, he provides in-depth discussion. I would like to offer my special thanks to Distinguished Professor Michael Weinert at University of Wisconsin-Milwaukee (UWM). I will never forget the day when he warmly welcomed me at

the airport in September 2014, and the photography book of city of the Milwaukee he gave me is irreplaceable to me. I deeply appreciate him giving many opportunities to learn from his expertise on physics. The study focusing on a relationship of the U_{eff} and MT sphere size was inspired from your suggestion. I am glad that this topic might be materialized as one of our publications, which will be the most interesting publication to me. Special thanks also for his gentleness and kindness including financial supports.

I am deeply grateful to Lecture Vlado K. Lazarov at University of York (UoY) for acceptance of my visiting. Works with him and his student, Arsham Ghasemi, are awesome to me because these studies have been first experience of close collaboration with experimentalists. I want to thank Professor Teruo Ono at ICR for joining his project of Grant-in-Aid for Specially Promoted Research. Professor Toyo Kazu Yamada at Chiba University gave me many chances to attend seminar, workshop, and domestic/international conferences. These were beneficial to talk my research progress to many people in a community of organic and organometallic molecule spintronics. I appreciate your warm encouragement too.

There are a lot of sweet memories of spending a long time of both study and drinking with many researchers and students: Professors Kunihiko Yamauchi, Hiroyoshi Momida, Dr. Masayuki Toyoda (currently Assistant Professor at Tokyo Institute of Technology), and students of Oguchi Laboratory at ISIR, Dr. Tomoki Yamashita at National Institute for Materials Science, Dr. Ming-Xing Chen, Dr. Tatsuya Shishidou and his family, and Mike's wife, Jane, of Weinert Group at UWM, Dr. Balati Kuerbanjiang and students, Arsham, Zlatko Nedelkoski, Genadi Naydenov, and Daniel Gilks of Vlado Group at UoY, and Kensho Tanaka, Takuya Taniguchi, and Michinari Kamiya of Ono Laboratory at ICR. I want to thank Ms. Cecilia Lowe who provided housing when I stayed York. I was very pleased to meet your "Thief Lane Family" including Barat, and serve Japanese style Sushi to them at Halloween party in 2015.

Special thanks to my colleagues, Yoshitaka Takemoto and Ayako Ito for fulfilling life in our laboratory for Bachelor and Master courses. I believe you guys were very precious to my student life, and the most impressive thing is so funny "Eringi party" at Gyukaku, Yoshitaka. I feel gratitude for helps in excessive paperwork from Ms. Harumi Iwano who is an administrative staff in Department of Physics Engineering, Mie University. Your smile makes always me happy.

My work was supported by the Research Fellowship of Japan Society for the Promotion of Science for Young Scientists, and Research Program for Next Generation Young Scientists

of "Dynamic Alliance for Open Innovation Bridging Human, Environment and Materials" in "Network Joint Research Center for Materials and Devices." Studies at UoY and UWM from September 2015 to February 2016 were supported by a scholarship program, the Regional development course, Japan Public-Private Partnership Student Study Abroad Program.

Finally, special words of tanks go to my family for their continuous help, moral support, warm encouragement in my whole life. I am forever indebted to my family for giving me the opportunities and precious experiences, and thanks to that, I have explored new directions and seek my own destiny. I also would like to express my deepest gratitude to my grandmother and late grandfather. I dedicate this dissertation to them.

September 2017,

Kenji Nawa

Contents

List of Tables

List of Figures

Chapter 1

Introduction

1.1 Density functional theory for correlated systems

The state-of-the-art *ab-initio* calculations based on density functional theory (DFT) [1–3] provide effective approaches to predict structural and electronic properties of condensed matters, for example, ground state electronic structures, crystal structures, phonon spectra, formation energies, electronic band structures, ionization potentials, superconducting properties, and exciting energy (by time-dependent DFT) in solid and molecules. In Kohn-Sham (KS) equation in the DFT, a problem of many-body interacting electrons is replaced by an one-particle non-interacting problem by using an effective potential. The effective potential can be expressed by three contributions, i) an external potential term like an attractive potential from nucleus, ii) Hartree term of classical interacting potential between electronics, and iii) exchange-correlation potential. The exchange-correlation potential may be given by a universal functional of the electron density [4], but the exact form is still unknown.

The exchange-correlation term contains all contributions that compensate the many-body effect from the non-interacting kinetic energy, the classical Hartree potential, and many-body approximations are proposed to the exchange-correlation potential in actual calculations. Most generally employed approximations are constructed as expansions around the homogeneous electron gas limit, i.e., local density approximation (LDA) and generalized gradient approximation (GGA). However, they often fail to obtain ground states, for example, band structures (band gap), magnetic moments, lattice constants, and so on, where most of them have difficulty

to demonstrate localizations of electrons. This problem arises from that these approximations generally provide quite poor descriptions of the ground state natures of N-electron system.

Much interest in correlated materials has been rapidly increased in novel engineering applications because of their unique physical properties. Among them are transition-metal monoxides, where TMs are Mn, Fe, Co, and Ni, that show Mott-type insulators [5,6]. However, there is a problem to treat these materials by the DFT calculations. The ground state is rock salt crystal structure. The spin magnetic moments of TM atoms exhibit an anti-ferromagnetic (AFM) II ordering, where the moments within the same (111) plane are parallel and they order antiparallel along the [111] direction, below their respective Néel temperatures. [7] The AFM II magnetic ordering is stabilized by super-exchange interaction via the oxygen atoms [8,9]. From the most literatures, even though it has been shown that many structural, magnetic, electronic properties may be described by the LDA- or GGA [7, 7, 10–20], the properties of band gap or photoemission spectra can not be described quantitatively or not at all within mean-field approximations [21]. In CoO and FeO, while insulating electronic structures were observed in experiments, the LDA (and GGA) calculations show a metallic state, where the partially occupied triplet t_{2g} state in minority channel electronic subshell results in a gapless state, in contrast to experiments. Even in MnO and NiO, whose minority t_{2g} orbital are empty or fully occupied, the LDA/GGA analysis underestimates the band gap compared to experimental values. These failures arise from an insufficient description of localize character of the TM-3d electrons in the LDA/GGA. The other examples includes in metal complexes: e.g., oxidized products, rare-earth (RE) compounds, organometallic molecules and so on [22–26]. Thus, for these reasons, an established method to capture the ground state properties for correlated materials has been strongly desired.

Efforts to go beyond the LDA (and GGA) have widely attempted so as to include the many-body effects, by using not only model Hamiltonians but also the DFT frameworks. The model Hamiltonian approach, which may be a simplest way to treat correlated materials, describes the localized electron behavior by using parameters characterizing electronic structures. For example, Hubbard model, which is one of the most used models, is based on two parameters for on-site Coulomb correlation and hopping terms [27–34]. In the DFT framework, several methods to introduce the many-body effects have been developed in the last decades. Dynamical mean field theory (DMFT) and reduced density matrix functional theory (RDMFT) are

known well as notable approaches to improve the description of correlated electron systems significantly. Hybrid functional method, in which the exchange-correlation function is combined by the exchange-correlation function of the DFT and the exchange term in Hartree-Fock (HF) approximation, is nowadays employed in organometallic molecule systems. Whereas, they have very huge computational costs extremely compared to the standard DFT calculations. Thus, an efficient approach must be required to extend to large systems consisting of a large number of atoms.

In complex systems, DFT+U method is one of the solutions, which has been practically used and comes very popular in the *ab-initio* calculation community. The total energy functional is formulated based on the DFT complemented with the Hubbard model [35–39]. Because of the simplicity of its expression, distinctive advantages are offered; for example, low computational costs, easy derivation of energy derivatives for atomic forces and stresses in structural optimizations, and second derivatives for atomic force constants or elastic constants. Moreover, since the DFT+U method introduces Hubbard-model parameters to represent screened on-site Coulomb (U) and exchange (J) interactions, rather clear and simple understandings of physical meaning in role of these parameters are given as a benefit.

1.2 Problems in density functional theory for correlated systems

Despite that the DFT provides a critical role to understand the electronic structures, most calculations approximated within the DFT has a serious problem. This section provides a critical imperfection of mean-field-based DFT, which is recognized as a popular failure: a derivative discontinuity [40–55]. This quantity may be corrected by the DFT+U method (this is indeed a primary target in this study) although the standard LDA and GGA functionals lose it mathematically.

Firstly, the a definition of fundamental energy gap, $E_{\rm gap}$, is overviewed from both experiments and DFT calculations. A central quantity of the $E_{\rm gap}$, is exactly defined by a difference between first ionization energy (IE) and electron affinity (A) as,

$$E_{\rm gap} = {\rm IE} - {\rm A}, \tag{1.1}$$

where IE and A correspond to the energies where an electron puts from vacuum level to energy levels of highest occupied (HO) and lowest unoccupied (LU) orbitals, respectively, as shown in Fig. 1.1 (a). However, the DFT solving eigenstates of a single particle moving in an effective potential gives an energy gap that differs from the fundamental gap of Eq. (1.1). For a given N-electron system, the gap must be computed by considering the Kohn-Sham (KS) system of both N and $(N+1)$ electrons, and be expressed in terms of the KS eigenvalues as follow:

$$E_{\rm gap} = \varepsilon^{N+1}(N+1) - \varepsilon^{N}(N), \tag{1.2}$$

where the $\varepsilon^{M}(j)$ indicates the j-th KS-orbital energy of the M-particle system.

In the KS system with the N electrons, Ewald term diverges due to charge neutrality breakdown because when an electron is added into the system, the energy gap is alternatively expressed

$$\begin{aligned} E_{\rm gap} &= \left[\varepsilon^{N}(N+1) - \varepsilon^{N}(N)\right] + \left[\varepsilon^{N+1}(N+1) - \varepsilon^{N}(N+1)\right] && (1.3)\\ &= \Delta_{\rm ks} + \Delta_{\rm xc} && (1.4) \end{aligned}$$

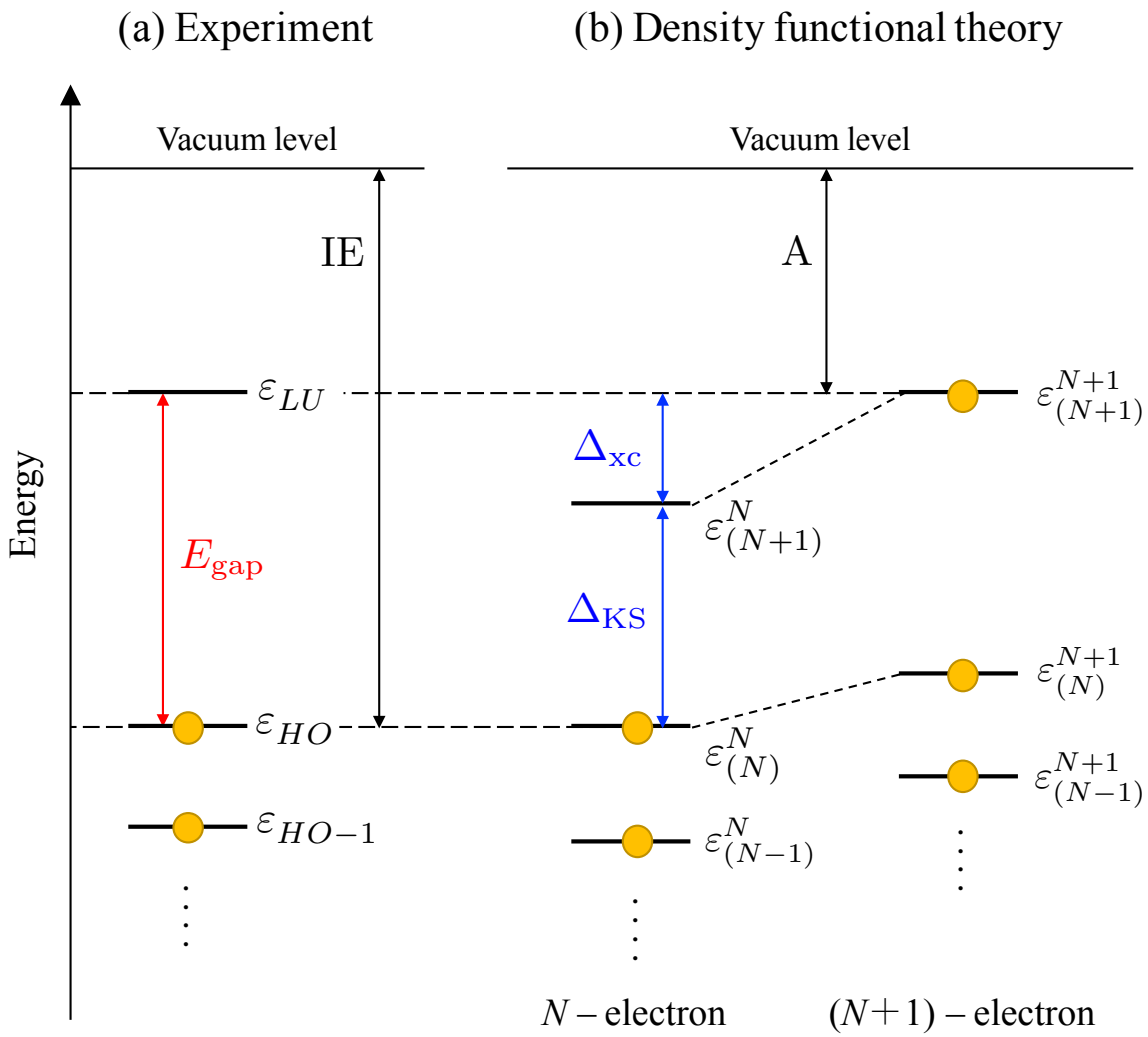

Figure 1.1: Schematics of energies of the highest occupied (HO), $\varepsilon_{\mathrm{HO}}$, and the lowest unoccupied (LU), $\varepsilon_{\mathrm{LU}}$, orbital states in experiment, compared to those of one-electron Kohn-Sham orbitals, $\varepsilon^{M}_{(i)}$, for N- and $(N+1)$-electron systems in density functional theory. The $\varepsilon^{M}_{(i)}$ denotes j-th eigenstates for M-electron system and yellow circles are electrons. The fundamental gap can be expressed using difference between the first ionization energy (IE) and the electron affinity (A) or summ of Δ_{ks} and Δ_{xc}; $E_{\mathrm{gap}} = \mathrm{IE} - \mathrm{A} = \Delta_{\mathrm{ks}} + \Delta_{\mathrm{xc}}$.

where N-electrons of non-interacting KS system eigenstates $\Delta_{\rm ks}$ are used but there is a correction term. [40–42, 56]. In the DFT (and even in Hartree-Fock approximation), when an additional electron is put in the LU orbital, $\varepsilon_{\rm LU}$, i.e., into $(N+1)$-electron system, all eigenstates of the one-electron orbitals (KS-orbitals) are shifted toward relatively higher in energy compared these in the N-electron system (see Fig. 1 (b)). This energy shift from the $\varepsilon^N(N+1)$ to the $\varepsilon^{N+1}(N+1)$ is the $\Delta_{\rm xc}$, which never knows from the N-electron KS problem. Most of approximation functions in the DFT, such as LDA and GGA, is approximately assumed to zero ($\Delta_{\rm xc} \approx 0$), thus,

$$E_{\rm gap} \approx \Delta_{\rm ks}. \tag{1.5}$$

However, the $\Delta_{\rm xc}$ is sometimes sizable in correlated systems [44, 57–60]. This fact is known as a "derivative discontinuity" problem in the computational field of correlated materials.

According to Perdew and coauthors [40], in a grand canonical ensemble that allows the number of electrons, N, to be fractional as well as an integer, the continuous behavior of the total energy with respect to the N is expressed using a fractional weight of ω as

$$E(N_0+\omega) = (1-\omega)E(N_0) + \omega E(N_0+1). \tag{1.6}$$

The N_0 denotes an integer and $0 \leq \omega \leq 1$. The curve itself is continuous while its derivative $\partial E/\partial N$ has discontinuities at integers of N, resulting in a series of straight line segments interpolating the energies corresponding to those of closed systems with integers of N, as shown in Fig. 1.2 (a) (red line).

Janak's theorem [61] gives an i-th eigenstate from the total energy derivative with respect to the weight of occupation n_i as

$$\frac{\partial E}{\partial n_i} = \varepsilon_i. \tag{1.7}$$

A further consideration of an eigenstate of HO orbital, $\varepsilon_{\rm HO}$, for N- and $(N+1)$-electron systems give IE and A as

$$\frac{\partial E^N}{\partial n_{\rm HO}} = \varepsilon^N_{\rm HO} = -{\rm IE}, \tag{1.8}$$

$$\frac{\partial E^{N+1}}{\partial n_{\mathrm{HO}}} = \varepsilon_{\mathrm{HO}}^{N+1} = -\mathrm{A}, \tag{1.9}$$

respectively (thanks to ionization potential (IP) theory [62]). Figure 1.2 (b) shows the dependence of $\varepsilon_{\mathrm{HO}}$ on the N. Based on the Eq. (1.1) and the IP theorem, the fundamental gap is the difference of $\varepsilon_{\mathrm{HO}}^{N_0+1}$ and $\varepsilon_{\mathrm{HO}}^{N_0}$, corresponding to a magnitude of the step (Δ) in Fig. 1.2 (b) [63,64]. Thus, a definition of the fundamental gap must be concluded as a "discontinuity" (step, Δ) of the slope of $\varepsilon_{\mathrm{HO}}$ which, equals to the total energy "derivative", at N_0.

In the fundamental gap given by Eq. (1.4), note that the Δ_{ks} must be obtained from a non-interacting kinetic energy term and Δ_{xc} from exchange-correlation term in the Kohn-Sham Hamiltonian, respectively, while a classical Hertree potential and an external potential do not contribute to the derivative discontinuity behaviors. Thus, this Δ_{xc}, being missed by the LDA and GGA, should be what to be corrected precisely. As described previously, the total energy of the standard (approximate) DFT calculation is parabola as a function of the N because a variable $n(\mathbf{r})$ varies analytically and continuously, while exact total energy should be a piecewise-linear with an integer variable N. Hence, the DFT+U method is expected to recover the quadratic curve of approximate DFT to fit the exact one. In other words, the DFT+U method plays a role to reintroduce the derivative discontinuity into the mean-field Kohn-Sham potential: approximately $\Delta_{\mathrm{xc}} \approx U_{\mathrm{eff}}$. Importantly, this additional term is expected to contribute to not only the fundamental gap but also ground state electronic structures and other physical properties.

1.3 DFT+U method for correlation correction

The DFT+U method, which is required to solve the derivative discontinuity problem, is one of powerful and conventional tools suitable for calculations of large systems without expensive computational costs [29, 37, 38, 65–67]. Further, it has been used to successfully calculate electronic structures, magnetic and optical properties that agree with experiments. For example, Yang *et al.* [68] have demonstrated that in bulk fcc Ni Coulomb correlations treated within the +U method (U=1.9 eV, J=1.2 eV) push degenerate d states away from the Fermi level, and that this behavior stabilizes the magnetic anisotropy along the [111] direction in agreement with experiments, [69, 70] but contrary to $U = 0$ calculations. The +U method was also suc-

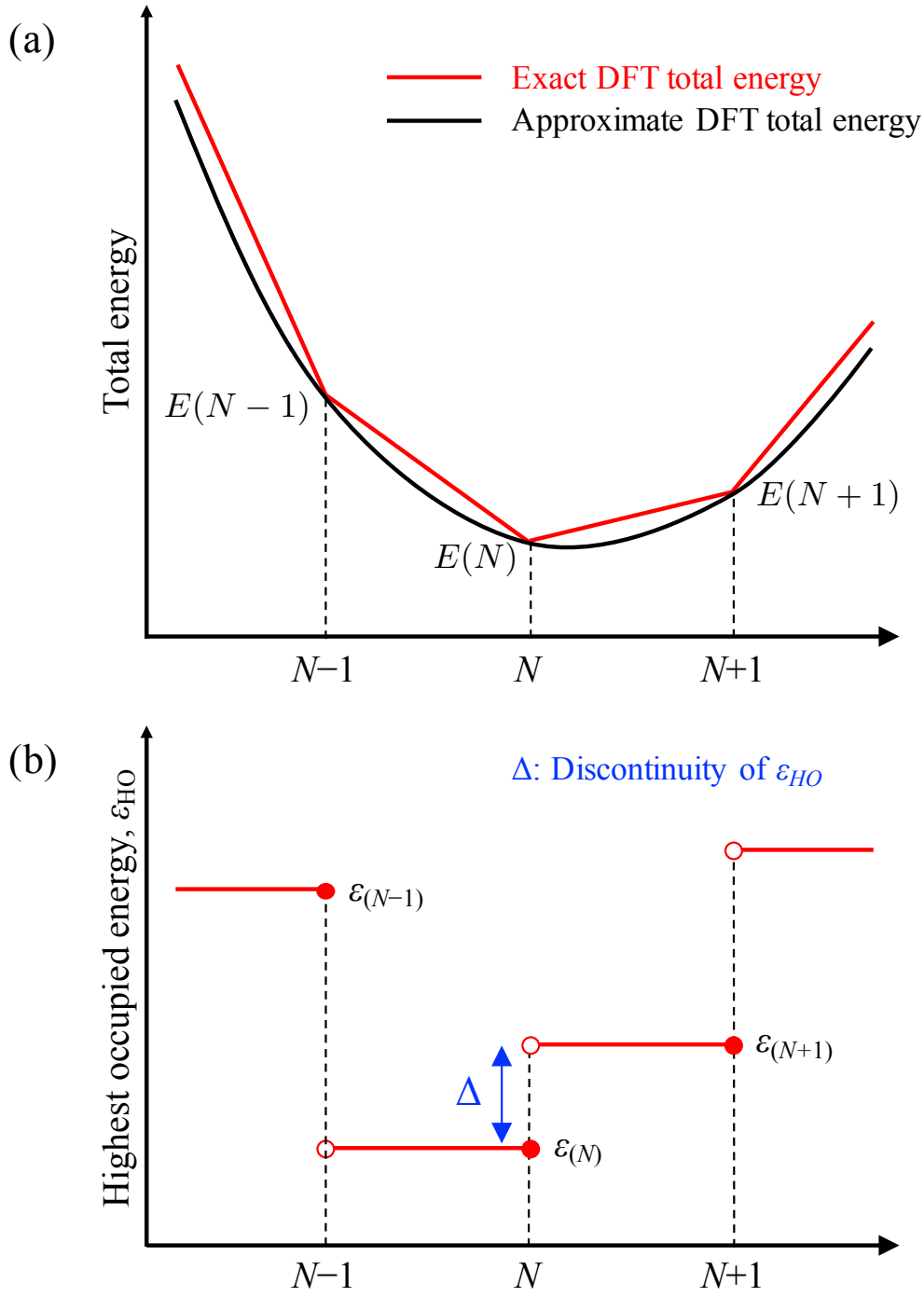

Figure 1.2: (a) Total energy profile with respect to number of electrons at a site where the electrons are localized. If an effective potential in Kohn-Sham Hamiltonian is given by exactly correct form, the total energy corresponds to a series of straight lines interpolating the energies of closed systems with integer number of electrons, N (see red line), but otherwise it is a parabola (see black line). (b) The highest occupied energy, $\varepsilon_{\mathrm{HO}}$, depending on the N for the exact total energy functional.

cessfully applied [71] to explain the experimentally observed magnetic switching phenomenon at the $BaTiO_3$–Fe interface: The trend of the polarization versus the +U parameters was used to clarify the magneto-electricity mechanism at the interface. The +U approach has been essential in the other areas, including studies of the band gap and phase stability in polymorphic TiO_2 [72] the structural and optical properties of diluted magnetic semiconductors, [73] and the ground state electronic configuration in organometallic molecules. [74]

However, because a magnitude of the correlation correction for a given model is generally unknown, in the most studies using the +U method, typically the values of on-site Coulomb and exchange interaction parameters are empirically determined. One may often regard the U and J as adjustable parameters. This analysis plays a crucial role to understand a tendency of physical or chemical properties, but still reliable values are not clear. Also, one may set their magnitudes to match experimental observations, for example, band gaps and magnetic moments, but, in this case, it is impossible to predict a novel discovery of physical phenomena in advance of the experimental studies. Alternatively, the U and J values of a bulk state are employed for systems that are characterized by reduced symmetry, low dimensionality, or symmetry such as nanoparticle, cluster, molecule, alloys, surfaces or interfaces [75–82]. It has been reported that the value of Hubbard U and J for an atom in bulk solid is several times smaller than that for a free atom [83], and the parameters at metals or insulator surfaces are different from their bulk values because of a competition of surface electronic state and effective band narrowing [84]. Thus, this assumption must be unsatisfactory and may mislead conclusions.

Over the years, a number of researchers has pointed out an importance of a choice of the on-site +U parameter for reproducing experimental observations, but the optimal value depend on which exchange-correlation functional is used [85] and the calculated material properties are very sensitive to the values of the on-site Coulomb and exchange terms even in the ground state. From the viewpoint of theoretical material design by using DFT+U method, importantly, the optimal and reliable +U parameters are necessary to obtain true ground state where the electron correlation described by mean-field approximation is replaced by the Hubbard model.

More recently, determination of the parameters from *ab-initio* calculations has been attempted and various non-empirical method for calculations of these values of both "bare" and "screened" versions have been developed. Table 1.3 summarizes previous theoretically calcu-

lated effective on-site Coulomb parameters, $U_{\text{eff}} = U - J$. For Mn in MnO, Anisimov and co-workers [36] obtained $U_{\text{eff}} = 6.04$ eV by a constrained LDA approach using an orthonormalized LMTO basis set, whereas Pickett *et al.* [86] extracted a value of 3.6 eV using a LCAO basis. The parameters have also been calculated within the constrained random phase approximation (cRPA). [87–89] For PAW or Wannnier (MLWF) basis sets, U_{eff} values are of relatively similar magnitude (around 4 eV) for FeO, but differ more significantly in other systems, particularly NiO. [87–89] In 2005, Cococcioni and de Gironcoli [90,91] proposed a minimally extended methodology from the limited LDA scheme based on linear response theory and the constrained DFT method implemented using plane wave pseudopotentials; a major accomplishment was that the derived parameter excludes energy contributions of one electron kinetic term. Their calculated values are also listed in Table 1.3. However, these calculated values vary over a wide ranges of values even for the same ionic state in a given material.

Comparison of absolute values of U_{eff} is not meaningful since theoretically determined parameters can significantly depend on the computational setup, e.g., basis sets and projection operators. [92] Unfortunately, this implies that choosing "good" parameters for a specific computational method is problematic. Nevertheless, there is no prescription to select a proper value in calculations. In this respect, systematical investigations of the U_{eff} values in different computational methods are strongly desired.

Table 1.1: Literature's values of the effective on-site Coulomb interaction, $U_{\text{eff}} = U - J$ (in eV), for TM atom (TM = Mn, Fe, Co, Ni) of transition-metal monoxides. The first and second columns give the basis sets and method used to calculate U_{eff}, respectively.

Basis set	Method	MnO	FeO	CoO	NiO	Ref.
LMTO[a]	Constrained LDA	6.04	5.91	6.88	7.05	[36]
LCAO[b]	Constrained LDA	3.6	4.6	5.0	5.1	[86]
PAW[c]	cRPA	4.0	4.0	3.3	6.4	[87]
		3.9	4.0	3.4	6.0	[88]
MLWF[d]	cRPA	5.6	4.8	6.3	5.6	[89]
PW[e]	Linear response	5.25	4.3	6.1	5.77	[90, 91]
UHF-MO[f]	[g]	-	3.7	-	-	[93]

[a] LMTO: Linear muffin-tin orbital.
[b] LCAO: Linear combination of atomic orbitals.
[c] PAW: Projected augmented wave.
[d] MLWF: Maximally localized Wannier function.
[e] PW: Plane wave.
[f] UHF-MO: Un-restricted Hartree-Fock molecular orbitals.
[g] The U_{eff} is determined from a relationship between the parameters and Coulomb and exchange integrals.

1.4 Purpose and contents of thesis

On the basis of previous introductions, here, a methodology to derive the effective on-site Coulomb interaction has been developed using full-potential linearized augmented plane wave method. The linear response approach is employed to achieve the derivation of the U_{eff}. Then, this methodology is applied to prototypical correlated materials of transition-metal monoxides, TMO, and organometallic metallocene molecules, $TMCp_2$, to solve following issues; (i) getting a reliable Hubbard U_{eff} and extracting an essential ingredient to choose the proper correction, and (ii) analyzing an effect of on-site correlated interaction to electronic configuration in d-orbital electrons for organometallic complex.

This dissertation is organized as follow. In Chapter 2, details of theory for calculations of the on-site +U parameters and computational theory are presented. After introduced the DFT+U method, the calculation procedures to obtain the effective +U values, $U_{\text{eff}} = U - J$ in this study, from linear response approach is presented. In this, all-electron full-potential linearized augmented plane wave method based on the constraint DFT, in which Lagrange multiplier method is introduced to control the d-electron density matrix, is used. An application of the present method to transition-metal monoxides is devoted in Chapter 3, where an intrinsic origin of the discrepancy among calculated U_{eff} values from different methodologies is considered. In Chapter 4, this method is further applied to analysis of ground-state electronic structures of correlated organometallic metallocenes, where the various electronic configurations of d-electrons are energetically degenerated. The conclusion of the thesis is given in Chapter 5.

Chapter 2

Theory and computational method

2.1 Density functional theory

2.1.1 Background of density functional theory

In quantum mechanics, motions of electrons having two characters of particle and wave simultaneously, are basically formulated by Schrödinger equation [94] as,

$$H\Psi(\mathbf{r}_i, t) = E\Psi(\mathbf{r}_i, t), \tag{2.1}$$

where Hamiltonian H consists of kinetic and potential operators for electrons and nuclei. The $\Psi(\mathbf{r}_i, t)$ is many-body wave function of all particles, denoted as index i, at position $\mathbf{r}_i$ at time t, and E is eigenvalues of many-body systems corresponding to orbital energies. For analysis of behaviors of electrons and nuclei that interact in their electrostatic Coulomb interaction, it is impossible to solve the Eq. (2.1) except for hydrogen atom where only one electron and one proton interact each other. To solve the Schrödinger equation of Eq. (2.1) for many-body system, several approaches have been established and one of the most famous approaches is Born-Oppenheimer approximation which assumes that the movement of nuclei is too slow compared to that of electrons [95]. As a result, the Hamiltonian of Schrödinger equation

becomes

$$H = \sum_{i=1}^{N} \left(-\frac{1}{2}\nabla_i^2 \right) + \frac{1}{2} \sum_{j \neq i} \frac{1}{|\mathbf{r}_i - \mathbf{r}_j|} - \sum_{i=1}^{N} \sum_{\sigma} \frac{Z_\alpha}{|\mathbf{r}_i - \mathbf{R}_\alpha|}. \tag{2.2}$$

The first term is sum of the kinetic operators for all electrons in the system, the second one is sum of the Coulomb repulsive potential of electron-electron, and the third, sum of the electron-nucleus Coulomb interaction, respectively. The $\mathbf{r}_i$ is the position of i-th electron from the α-th nucleus (Z_α) at position $\mathbf{R}_\alpha$.

Many numerical methods for solving the Schrödinger equation under the Born-Oppenheimer approximation have been developed so far. Among them are density functional theory (DFT), developed by Hohenberg and Kohn in 1964 [1], which states ground state properties can be obtained from the ground state electron charge densities. It importantly has an advantage: the degree of freedom is significantly reduced to only 3 from $3N$ dimensions.

2.1.2 The Hohenberg-Kohn theorem

The DFT was developed semiclasically by Tohmas and Fermi in 1920's [96,97]. In the model proposed by them, total energy for electrons is given by a functional of the charge density of "uniform" electrons. In 1964, Hohenberg and Kohn succeeded to formulate the total energy as a function of the charge density for a given "external" potential for N-electron system. [1] This is known as the Hohenberg-Kohn theorem. This theorem states:

1. *The ground state total energy, E, (for a non-spin-polarized system) is given exactly as a function of the ground state charge density, $n(\mathbf{r})$, as*

$$E = E[n]. \tag{2.3}$$

2. *The true ground state charge density minimized the $E[n]$ (variational principle), and other ground state properties are also functionals of the ground state charge density.*

For a spin-polarized system, the total energy and the other properties at ground state are given by functional of spin densities. Generally, the spin densities are expressed as four-component

spinors, but more simply like in collinear magnetic system, the total energy of spin-up and -down densities, $n^{\uparrow}$ and $n^{\downarrow}$, may be given by

$$E = E[n^{\uparrow}, n^{\downarrow}]. \tag{2.4}$$

According to this theorem, the total energy of the considered system is

$$E[n] = T[n] + E_{\mathrm{H}}[n] + V_{\mathrm{ext}}[n] + (\text{non-classical term}), \tag{2.5}$$

where the first term, $T[n]$, is the kinetic energy of the interacting electrons, the second one, $E_H[n]$, is Hartree energy which counts the Coulomb interaction of electron charge density including the contribution from itself, and the third one, $V_{\mathrm{ext}}[n]$, is external potential given by

$$V_{\mathrm{ext}}[n] = \int n(\mathbf{r}) v_{\mathrm{ext}}(\mathbf{r}) d\mathbf{r}. \tag{2.6}$$

However, the Hohenberg-Kohn theorem could not provide an exact form of the total energy functional, particularly, the kinetic term of interacting electrons. Therefore, the utility of the DFT would depend on the discovery of sufficient and accurate approximations. This problem was solved by Kohn and Sham one year after Hohenberg and Kohn proposed their theorem.

2.1.3 The Kohn-Sham equation

Kohn and Sham, in 1965, had succeeded to solve the remaining problem in Hohenberg-Kohn theorem, i.e., kinetic energy of interacting electrons. [2, 3] They replaced this kinetic contributions of interacting electrons with those of non-interacting ones by assuming a system, where the electrons move freely but feel an effective potential. Even in this bold assumption, the non-interacting kinetic term includes the most part of exact $T[n]$ in Eq. (2.5) and can be calculated acculately.

To strictly formulated total energy, which has unknown part, $E_{\mathrm{xc}}[n]$, is expressed by

$$E[n] = T_{\mathrm{s}}[n] + E_{\mathrm{H}}[n] + V_{\mathrm{ext}}[n] + E_{\mathrm{xc}}[n]. \tag{2.7}$$

The $T_{\rm s}[n]$ denotes the kinetic energy under the non-interacting assumption,

$$T_{\rm s}[n(\mathbf{r})] = \sum_{i=1}^{N} \left\langle \psi_i(\mathbf{r}) \left| -\frac{1}{2}\nabla_i^2 \right| \psi_i(\mathbf{r}) \right\rangle \tag{2.8}$$

which is diagonalized by a single particle wave functions, $\psi_i(\mathbf{r})$. The $T_{\rm s}$ is a functional of density and satisfies Pauli principle, so the density is obtained from

$$n(\mathbf{r}) = \sum_{i=1}^{N} |\psi_i(\mathbf{r})|^2 . \tag{2.9}$$

The $V_{\rm ext}[n]$ given in Eq. (2.6) is an external potential that is usually introduced as an attractive interaction of electron-nucleus. The Hartree component of the electron-electron interaction, $E_{\rm H}[n]$, is given by

$$E_{\rm H}[n] = \frac{e^2}{2} \int\int \frac{n(\mathbf{r})n(\mathbf{r}')}{|\mathbf{r}-\mathbf{r}'|} d\mathbf{r}d\mathbf{r}'. \tag{2.10}$$

The unknown part, $E_{\rm xc}[n]$, corresponds to the exchange-correlation energy to correct to the interacting system.

As a result, by replacing the external potential $V_{\rm ext}[n]$ in Eq. (2.6) to the potential from nuclei, $v_{\rm nucl}(\mathbf{r})$, the total energy is finally written as

$$E[n] = T_{\rm s}[n] + \frac{e^2}{2} \int\int \frac{n(\mathbf{r})n(\mathbf{r}')}{|\mathbf{r}-\mathbf{r}'|} d\mathbf{r}d\mathbf{r}' + \int n(\mathbf{r}) v_{\rm nucl}(\mathbf{r}) d\mathbf{r} + E_{\rm xc}[n]. \tag{2.11}$$

From the variational princple under a constraint condition to conserve the electrons as a constant N,

$$N = \int n(\mathbf{r}) d\mathbf{r}, \tag{2.12}$$

the one-electron equation is derived as follow:

$$\left[-\frac{1}{2}\nabla_i^2 + V_{\rm eff}(\mathbf{r}) \right] \psi_i(\mathbf{r}) = \varepsilon_i \psi_i(\mathbf{r}). \tag{2.13}$$

The effective potential, $V_{\text{eff}}(\mathbf{r})$, is

$$V_{\text{eff}}(\mathbf{r}) = v_{\text{nucl}}(\mathbf{r}) + \int \frac{n(\mathbf{r}')}{|\mathbf{r} - \mathbf{r}'|} d\mathbf{r} + \mu_{\text{xc}}(\mathbf{r}). \tag{2.14}$$

The Eq. (2.13) and (2.14) are well-known the Kohn-Sham equations in which the final solution of energy eigenvalues, ε_i, and one-particle wave function, $\psi_i(\mathbf{r})$, are determined by self-consistent field using the charge density, $n(\mathbf{r})$, of Eq. (2.9). Thus, a problem of finding the ground state of many-body Schrödinger equation (Eq. (2.1) and (2.2)) turns to solving the Kohn-Sham one-particle problem.

The exchange-correlation potential is given by

$$\mu_{\text{xc}}(\mathbf{r}) = \frac{\delta E_{\text{xc}}[n(\mathbf{r})]}{\delta n(\mathbf{r})}, \tag{2.15}$$

and the functional $E_{\text{xc}}[n]$ should include a non-classical contribution of the kinetic energy and the Coulomb repulsion, in other words, include quantum many-body effects. In principle, this is expressed from Eq. (2.11) as

$$E_{\text{xc}}[n] = F[n] - T_{\text{s}}[n] - \frac{e^2}{2} \int \int \frac{n(\mathbf{r})n(\mathbf{r}')}{|\mathbf{r} - \mathbf{r}'|} d\mathbf{r} d\mathbf{r}' - \int n(\mathbf{r}) v_{\text{nucl}}(\mathbf{r}) d\mathbf{r}', \tag{2.16}$$

here the Kohn-Sham total energy functional $E[n]$ is rewritten by universal functional $F[n]$. However, the exact form of the $E_{\text{xc}}[n]$ is still unknown, and approximated approaches are necessary to perform numerical calculations on practical level.

2.1.4 Approximation for exchange-correlation functional

The most widely used approximation for the μ_{xc} is constructed on an assumption that the charge density $n(\mathbf{r})$ is slowly varying so that the μ_{xc} can be estimated locally by homogeneous electron gas. This is called as local density approximation (LDA) and given by

$$E_{\text{xc}}[n(\mathbf{r})] \approx \int \varepsilon_{\text{xc}}(n) n(\mathbf{r}) d\mathbf{r}, \tag{2.17}$$

where the $\varepsilon_{\rm xc}$ is exchange-correlation energy density which is functional of the density at a position $\mathbf{r}$. The exchange-correlation potential in Eq. (2.14) is then expressed as

$$\mu_{\rm xc}(\mathbf{r}) = \left.\frac{d\varepsilon_{\rm xc}(n)n}{dn}\right|_{n=n(r)} = \left.\left(1 + n\frac{\delta}{\delta n}\epsilon_{\rm xc}(n)\right)\right|_{n=n(r)}. \tag{2.18}$$

Several useful functionals for LDA have been proposed by, e.g., Hedin and Lundqvist [98], von Barth and Hedin [99], and Gunnarsson and Lundqvist [100].

For a spin polarized system, this functional is rewritten by separating the majority (spin-up) and minority (spin-down) states as,

$$E_{\rm xc}[n^{\uparrow}(\mathbf{r}), n^{\downarrow}(\mathbf{r})] = \int \left(n^{\uparrow}(\mathbf{r}) + n^{\downarrow}(\mathbf{r})\right) \varepsilon_{\rm xc}[n^{\uparrow}(\mathbf{r}), n^{\downarrow}(\mathbf{r})] d\mathbf{r}. \tag{2.19}$$

The energy density $\varepsilon_{\rm xc}[n^{\uparrow}(\mathbf{r}), n^{\downarrow}(\mathbf{r})]$ is also derived by an assumption locally at each position, $\mathbf{r}$, by using the homogenous electron gas description with a spin polarization $\mathbf{m}(= n^{\uparrow}(\mathbf{r}) - n^{\downarrow}(\mathbf{r}))$. The exchange-correlation potential depends on the spin direction; e.g., for spin-up,

$$\begin{aligned} \mu^{\uparrow}_{\rm xc}(\mathbf{r}) &= \frac{\delta E_{\rm xc}[n_{\uparrow}(\mathbf{r}), n_{\downarrow}(\mathbf{r})]}{\delta n_{\uparrow}(\mathbf{r})} & (2.20) \\ &= \varepsilon_{\rm xc}[n_{\uparrow}(\mathbf{r}), n_{\downarrow}(\mathbf{r})] + n(\mathbf{r})\left.\frac{\delta \varepsilon_{\rm xc}(n_{\uparrow}, n_{\downarrow})}{\delta n}\right|_{n_{\uparrow}=n_{\uparrow}(\mathbf{r}), n_{\downarrow}=n_{\downarrow}(\mathbf{r})} & (2.21) \end{aligned}$$

and same way for the spin-down. Here, the $n^{\uparrow}(\mathbf{r}) + n^{\downarrow}(\mathbf{r})$ is simplified by $n(\mathbf{r})$. Then, the Kohn-Sham equation is rewritten as

$$\left[-\frac{1}{2}\nabla_i^2 + V^{\sigma}_{\rm eff}(\mathbf{r})\right] \psi_{i,\sigma}(\mathbf{r}) = \epsilon_{i,\sigma}\psi_{i,\sigma}(\mathbf{r}), \tag{2.22}$$

where the effective potential is rewritten using spin index σ as,

$$V^{\sigma}_{\rm eff}(\mathbf{r}) = v_{\rm nucl}(\mathbf{r}) + \int \frac{n(\mathbf{r}')}{|\mathbf{r} - \mathbf{r}'|} d\mathbf{r}' + \mu^{\sigma}_{\rm xc}(\mathbf{r}), \tag{2.23}$$

with

$$n^{\sigma}(\mathbf{r}) = \sum_{i=1}^{N} |\psi_{i,\sigma}(\mathbf{r})|^2. \tag{2.24}$$

Generalized gradient approximation (GGA) provides better results than the LDA in pre-

dictions of bond lengths, binding energies of molecules, and crystal lattice constants, especially for the system where the electron density vary rapidly. In the GGA, in which spatial gradients of the charge density, $\nabla n(\mathbf{r})$, are further introduced, the definition of the exchange-correlation energy functional for the spin polarized case is form of

$$E_{\mathrm{xc}}^{\mathrm{GGA}}[n^{\uparrow}(\mathbf{r}), n^{\downarrow}(\mathbf{r})] = \int \left(n^{\uparrow}(\mathbf{r}) + n^{\downarrow}(\mathbf{r})\right) \varepsilon_{\mathrm{xc}}[n^{\uparrow}(\mathbf{r}), n^{\downarrow}(\mathbf{r}), |\nabla n^{\uparrow}(\mathbf{r})|, |\nabla n^{\downarrow}(\mathbf{r})|] d\mathbf{r}. \tag{2.25}$$

There are most widely used GGA functionals proposed by Becke (B88) [101] and Perdew *et al.* [102]. In this study, a highly parametrized functional reported by Perdew, Burke, and Ernzerhof (PBE) [103] was employed. Note that although the GGA results are rather correct compared to the LDA calculations typically, sometimes the GGA overcorrects the LDA, for example, in ionic crystals. Furthermore, both the LDA and GGA give different predictions from the experiments particularly for the localized and strongly correlated materials. Thus, the DFT+U method which is one of approximations beyond the LDA and GGA are necessary. The DFT+U method is described in section 2.3.

2.2 Method of calculations

2.2.1 Generalized eigenvalue problem

An one-electron wave function $\psi(\mathbf{r})$ is expanded in terms of basis functions $\phi(\mathbf{r})$. For a system with translational symmetry with reciprocal lattice vectors, $\mathbf{G}_j$, the $\psi(\mathbf{r})$ is expressed using Bloch's theorem as

$$\psi_{\mathbf{k},b}(\mathbf{r}) = \sum_j c_{\mathbf{k_j},b}\phi_{\mathbf{k_j}}(\mathbf{r}), \tag{2.26}$$

where b is a band index and $c_{\mathbf{k}_j,b}$ are expansion coefficients. For a simplicity, $\mathbf{k} + \mathbf{G}_j = \mathbf{k}_j$ is used. The number of basis functions $\phi_{\mathbf{k}_j}(\mathbf{r})$ is truncated up to finite j, corresponding to that within the cut-off energy, on practical level. To compute numerically, the set of basis function $\{\phi_{\mathbf{k}_j,b}(\mathbf{r})\}$ is necessary. The $c_{\mathbf{k}_j,b}$ are determined from a secular equation by Rayleigh-Ritz principle [104],

$$\sum_j \left[H_{jj'}(\mathbf{k}) - \varepsilon_{\mathbf{k},b}S_{jj'}(\mathbf{k})\right] c^j_{\mathbf{k},b} = 0. \tag{2.27}$$

The matrix elements of the Hamiltonian, $H_{jj'}(\mathbf{k})$, and overlap integral, $S_{jj'}(\mathbf{k})$, are

$$H^\sigma_{jj'}(\mathbf{k}) = \int_\Omega \phi^{\sigma,*}_{\mathbf{k}_j}\left[-\frac{1}{2}\nabla^2 + V^\sigma_{\text{eff}}\right]\phi^\sigma_{\mathbf{k}_{j'}} d^3\mathbf{r}, \tag{2.28}$$

and

$$S^\sigma_{jj'}(\mathbf{k}) = \int_\Omega \phi^{\sigma,*}_{\mathbf{k}_j}\phi^\sigma_{\mathbf{k_{j'}}} d^3\mathbf{r}. \tag{2.29}$$

The integrations are carried out over the volume of the unit cell, Ω. Employing a plne wave basis set offers significant advantages: e.g., orthogonality and diagonality in momentum. The DFT-based electronic structure methods are classified according to the representation that are for the density, potential, and KS-orbital. The choice of basis set has possibility to minimize the computational and human (programming) costs of calculations, while maintaining sufficient accuracy.

In the DFT, the coefficients $c_{\mathbf{k}_j,b}$ and the charge density $n(\mathbf{r})$ are determined separately:

in this case, the solution of coefficients are repeatedly obtained by solving the Kohn-Sham equation Eq. (2.13) (or Eq. (2.22) for spin-polarized system) for fixed charge density. When the basis set is given, the Eq. (2.27) can be solved at each **k**-point in the irreducible wedge of the Brillouin zone. Figure 2.1 shows a calculation flowchart, in which this process is known as self-consistent field (SCF) calculations.

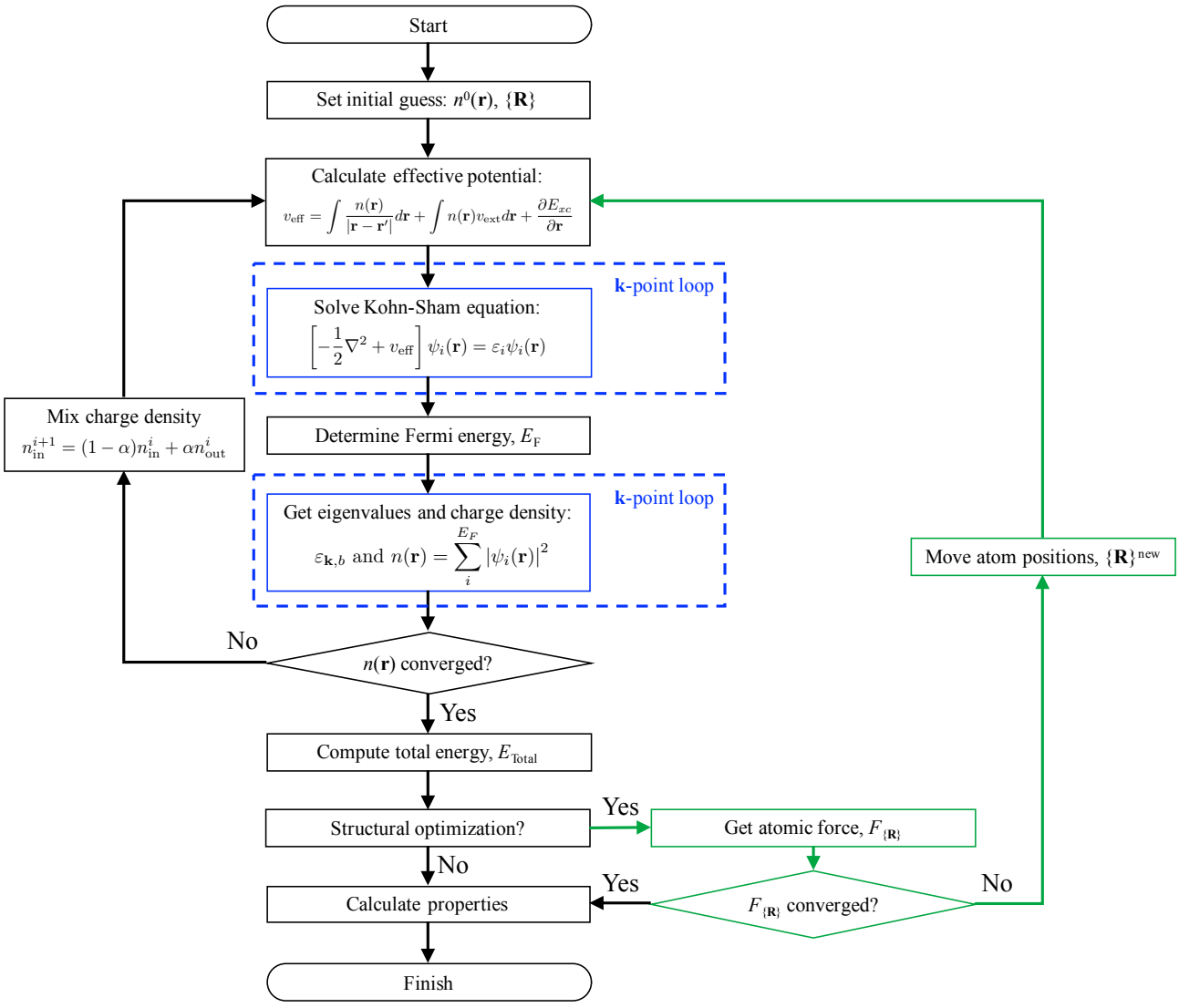

Figure 2.1: DFT-based calculation flowchart for the self-consistent field, beginning from setting initial charge density, $n^0(\mathbf{r})$ and atomic position $\{\mathbf{R}\}$. When geometric structure optimization is considered, the procedure in green color region is considered until atomic force is converged.

2.2.2 Augmented plane wave (APW) method to linearized APW method

In calculations based on the DFT, several approaches have been proposed, depending on choices of potential term (i.e., Hamiltonian) and bases set of wave functions. The choices may be of crucial importance to solve the Kohn-Sham equations with reducing computational costs and highly precision. This section presents augmented plane wave method (APW) and extension to linearized APW (LAPW) method.

In a condensed matter, the potential varies continuously but approximately it may be natural to divide two regions for a space: muffin-tin (MT) regions closes to a positive ion site (atomic nucleus) and interstitial region for the other space. This is known as a MT approximation and schematic of the potential is shown in Fig. 2.2 (a). The crystal potential, $V_{\mathrm{MT}}(\mathbf{r})$, is defined in two regions separately as

$$V_{\mathrm{MT}}(\mathbf{r}) = \begin{cases} V(r_\alpha) & (r_\alpha < S : \text{inside MT sphere}) \\ V_{\mathrm{MTZ}} & (r_\alpha > S : \text{interstitial}). \end{cases} \tag{2.30}$$

The local position vector $\mathbf{r}_\alpha$ is given as $\mathbf{r}_\alpha = \mathbf{r} - \mathbf{R}_\alpha$, where $\mathbf{r}$ is the position, and $\mathbf{R}_\alpha$ is the center of the MT sphere α with its sphere radius S (see Fig. 2.3).

When the $\mathbf{r}_\alpha$ is outside the MT sphere, the potential is assumed as a constant value that corresponds to muffin-tin zero (MTZ). A solution of non-interacting electron gas in the constant potential is mathematically described by simple plane wave, $e^{i\mathbf{k}\cdot\mathbf{r}}$, which satisfies Bloch's condition. Inside the MT spheres, on the other hand, the solution of an eigenstate is expressed by a product of radial and angular functions as

$$u_\ell(r_\alpha; E) Y_{\ell m}(\hat{\mathbf{r}}), \tag{2.31}$$

where $Y_{\ell m}(\hat{r})$ is the spherical harmonics function of angular and magnetic quantum numbers ℓ and m with an radial of the local vector, $\hat{\mathbf{r}}_\alpha$. The $u_\ell(\mathbf{r}_\alpha; E)$ is the radial function that is derived from the radial Schrödinger equation for the spherical potential $V_{\mathrm{s}}(\mathbf{r})$ in Eq. (2.30),

$$-\frac{1}{2}\frac{d}{dr}\left(r^2\frac{du_\ell}{dr}\right) + \left[\frac{\ell(\ell+1)}{r^2} + V_{\mathrm{s}}(r)\right] u_\ell = E u_\ell. \tag{2.32}$$

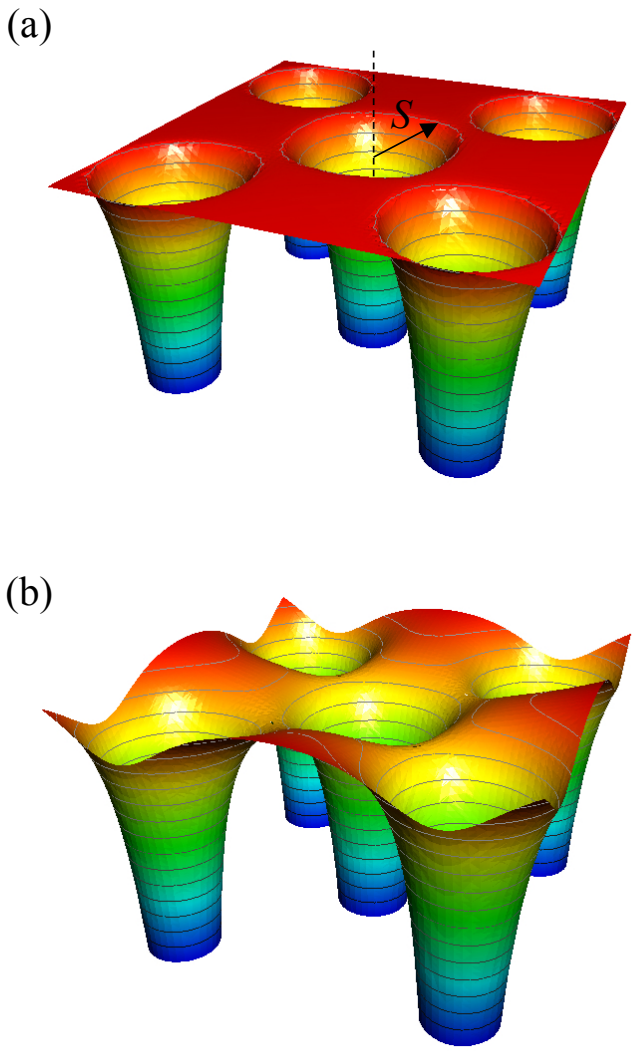

Figure 2.2: Schematics of the potential for (a) MT approximation and (b) full potential that removes the MT shape approximation. The S indicate the size of the MT sphere.

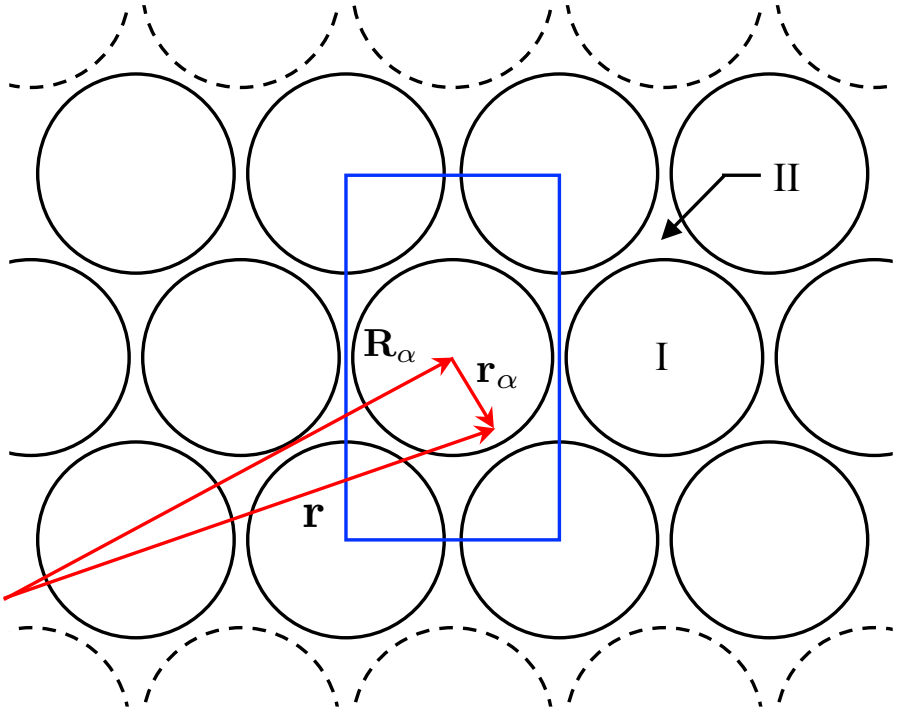

Figure 2.3: Local coordination of $\mathrm{r}_\alpha = \mathrm{r} - \mathrm{R}_\alpha$ in the divided regions into (I) inside MT sphere and into (II) interstitial. Blue square indicate the unit cell for a 3D-bulk system. Dotted spheres are replaced by vacuum layer for a 2D-film system: slab model.

In 1937, using this approximation, Slater [105] developed an augmented plane wave (APW) method. The concept of this method is that the plane wave inside the spheres are augmented by a linear combination of the solution of Eq. (2.31). The one-electron wave function is constructed using basis function $\phi_{\mathbf{k}_n}(\mathbf{r})$ with expansion coefficients $c_{\mathbf{k}_n}$ as

$$\psi_{\mathbf{k},b}(\mathbf{r}) = \sum_n c_{\mathbf{k}_n} \phi_{\mathbf{k}_n}(\mathbf{r}). \tag{2.33}$$

The summation is taken for reciprocal lattice vector $\mathbf{G}_n$, where $\mathbf{k}_n = \mathbf{k} + \mathbf{G}_n$. The resulting APW wave functions are

$$\phi^{\mathrm{APW}}_{\mathbf{k}_n}(\mathbf{r}) = \begin{cases} \frac{1}{\sqrt{\Omega}}\, e^{i\mathbf{k}_n \cdot \mathbf{r}} & \text{(interstitial)} \\ \sum_\alpha \sum_{\ell=0}^{\infty} \sum_{m=-\ell}^{\ell} A^{\alpha,n}_{\ell m} u_\ell(r_\alpha; E) Y_{\ell m}(\hat{\mathbf{r}}) & \text{(inside MT sphere).} \end{cases} \tag{2.34}$$

The volume of the unit cell is denoted by Ω. It is not guaranteed by the dual representations in Eq. (2.34) that they are contentious on the sphere boundary. Accordingly, it is necessary to impose a constraint: defining the coefficient $A^{\alpha,n}_{\ell m}$ through the spherical harmonics expansion of the plane wave.

A plane wave can be expanded by Bessel function j_ℓ,

$$e^{i\mathbf{k}_n\cdot\mathbf{r}} = e^{i\mathbf{k}_n\cdot(\mathbf{r}_\alpha+\mathbf{R}_\alpha)} \tag{2.35}$$

$$= e^{i\mathbf{k}_n\cdot\mathbf{R}} 4\pi \sum_{\ell m} i^\ell Y^*_{\ell m}(\mathbf{k}_n) j_\ell(k_n r_\alpha) Y_{\ell m}(\hat{\mathbf{r}}_\alpha), \tag{2.36}$$

where the two summations with respect to the ℓ and m are simplified into $\sum_{\ell m}$. Boundary condition of contentious connection of Eq. (2.34) provides the coefficients $A^{\alpha,n}_{\ell m}$ using Bessel function expansion of Eq. (2.36) as

$$A^{\alpha,n}_{\ell m} = \frac{1}{\sqrt{\Omega}} e^{i\mathbf{k}_n\cdot\mathbf{R}_\alpha} 4\pi i^\ell Y^*_{\ell m}(\hat{\mathbf{k}}_n) \frac{j_\ell(k_n S)}{u_\ell(S;E)}. \tag{2.37}$$

The Bessel function is approximately defined as

$$j_\ell(x) \approx \frac{1}{x}\sin x - \frac{\ell x}{2}. \tag{2.38}$$

Finally, the eigenvalues using APW basis functions are obtained from the Eq. (2.27).

If the energy parameter E_ℓ were taken as a fixed parameter, this APW method would offer a simple use of APW as a basis, resulting in a standard secular problem.Unfortunately, however, this is problematic due to a non-workable scheme. The APW functions are solutions of the Scrödinger equation inside MT spheres, but this is not achieved unless at the energy E_ℓ. They miss variational freedom to allow for changes in eigenstates when the band energy deviates from this reference, E_ℓ. Accordingly, the E_ℓ must be equal to the corresponding band energy, otherwise the eigenstates at a fixed **k**-point can not be obtained by a single diagonarization. This non-linear problem due to the u_ℓ depending on the band energy reference demands a much more computationally expensive procedures.

A further difficulty within the APW framework [106, 107] is that it is hard (but not impossible) to extend it beyond the warped MT approximation, which would be more real shape (non-spherical) potential in interstitial rather than constant like MT approximation, but a spherical potential inside the spheres. This is because, in this case, the optimal variational choice of the E_ℓ is no longer given by setting E_ℓ to the band energy. Particularly, in general, different eigenstates have different orbital characters inside sphere, e.g., d_{z^2} v.s. $d_{x^2-y^2}$, and so on. Whereas, in the non-spherical potential, these orbitals should experience different effective

potentials, which differ from the spherical averaged potential being used to determine the radial function u_ℓ.

For solving these difficulties, several modifications of the APW method had been proposed prior to 1975, for example by Bross and co-workers [108,109], Köelling [110], and Marcus [111]. In order to overcome the problem in APW method as well as providing a flexible and accurate band structure calculation method, Andersen [112, 113] proposed the linearized augmented plane wave (LAPW) method. This is the method employed in this study. Additional variational freedom being missed in the APW is included to the basis function inside the MT sphere so that it is not necessary to set the E_ℓ equal to the corresponding band energy. This is done by introducing the derivative of basis function with respect to the energy. This extension from APW can be regarded as a "linearization."

Because in the APW basis, the radial functions, u_ℓ, depend on the band energy, it can be seen as functions of r and ε, thus, the u_ℓ can be expanded into a Taylor-series around a certain E_ℓ,

$$\begin{aligned} u_\ell(r:\varepsilon) &= u_\ell(r:E_\ell) + \dot{u}_\ell(r:E_\ell)(\varepsilon - E_\ell) + \cdots \\ &= u_\ell(r:E_\ell) + \dot{u}_\ell(r:E_\ell)(\varepsilon - E_\ell) + O\left[(\varepsilon - E_\ell)^2\right]. \end{aligned} \tag{2.39}$$

The $\dot{u}_\ell$ is energy derivative of u_ℓ, $\dot{u}_\ell = \partial u_\ell/\partial\varepsilon$, and $O\left[(\varepsilon - E_\ell)^2\right]$ denotes errors that are quadratic in the energy difference.

In contrast to the APW basis, the LAPW method has errors of order $(\varepsilon - E_\ell)^2$ in the wave function, resulting in that of order $(\varepsilon - E_\ell)^4$ in calculated band energies due to the variational principle. Owing to the high order of this errors, the LAPWs can construct a well-described basis set over the broad regions, and all valence bands may typically be treated by a single energy parameter sufficiently.

The basis functions of the LAPW method are formed on the same way of the APW functions but with a different augmentation inside MT sphere region,

$$\phi^{\mathrm{LAPW}}_{\mathbf{k}_n}(\mathbf{r}) = \begin{cases} \frac{1}{\sqrt{\Omega}}\, e^{i\mathbf{k}_n\cdot\mathbf{r}} & \text{(interstitial)} \\ \sum_\alpha \sum_{\ell m} \left[A^{\alpha,n}_{\ell m} u_\ell(r_\alpha; E_\ell) + B^{\alpha,n}_{\ell m} \dot{u}_\ell(r_\alpha; E_\ell)\right] i^\ell Y_{\ell m}(\hat{\mathbf{r}}) & \text{(inside MT sphere),} \end{cases} \tag{2.40}$$

where an extra term of $B_{\ell m}^{\alpha,n}\dot{u}_\ell(r;E_\ell)$ is introduced in radial part compared to APW. The energy derivative functions of scalar relativistic radial functions $\dot{u}_\ell(r)$ are calculated from a radial Schrödinger equation derived by taking the energy derivative of Eq. (2.32),

$$\left[-\frac{1}{2}\frac{d^2}{dr^2}+\frac{1}{2}\frac{\ell(\ell+1)}{r^2}+V(r)-E_\ell\right]r\dot{u}_\ell(r)=ru_\ell(r). \tag{2.41}$$

In any cases, the radial $u_\ell(r)$ is required the normalization inside the MT sphere of darius S,

$$\langle u_\ell|u_\ell\rangle_S=\int_0^S u_\ell^2(r)r^2d\mathbf{r}=1. \tag{2.42}$$

Orthogonality of u_ℓ and $\dot{u}_\ell$ is easily obtained from the derivative of Eq. (2.42) with respect to the energy,

$$\langle u_\ell|\dot{u}_\ell\rangle_S=\langle\dot{u}_\ell|u_\ell\rangle_S=0. \tag{2.43}$$

Rewritting the radial part of Eq. (2.40) as

$$\varphi_{\ell m}^n=\left[A_{\ell m}^{\alpha,n}u_\ell(r_\alpha;E_\ell)+B_{\ell m}^{\alpha,n}\dot{u}_\ell(r_\alpha;E_\ell)\right]i^\ell Y_{\ell m}(\hat{\mathbf{r}}), \tag{2.44}$$

integrations in the α-th MT sphere, α, are summarized with $\dot{\varphi}_{\ell m}^n$ as its energy derivative:

$$\begin{aligned}
\langle\varphi_{\ell m}|\varphi_{\ell' m'}\rangle_S &= E_\ell\delta_{\ell\ell'}\delta_{mm'}, &(2.45)\\
\langle\varphi_{\ell m}|\dot{\varphi}_{\ell' m'}\rangle_S &= 0, &(2.46)\\
\langle\dot{\varphi}_{\ell m}|\varphi_{\ell' m'}\rangle_S &= 0, &(2.47)\\
\langle\dot{\varphi}_{\ell m}|\dot{\varphi}_{\ell' m'}\rangle_S &= N_\ell\delta_{\ell\ell'}\delta_{mm'}. &(2.48)
\end{aligned}$$

The matrix elements of one-electron Hamiltonian, H, are

$$\begin{aligned}
\langle\varphi_{\ell m}|H|\varphi_{\ell' m'}\rangle_S &= E_\ell\delta_{\ell\ell'}\delta_{mm'}, &(2.49)\\
\langle\varphi_{\ell m}|H|\dot{\varphi}_{\ell' m'}\rangle_S &= \delta_{\ell\ell'}\delta_{mm'}, &(2.50)\\
\langle\dot{\varphi}_{\ell m}|H|\varphi_{\ell' m'}\rangle_S &= 0, &(2.51)\\
\langle\dot{\varphi}_{\ell m}|H|\dot{\varphi}_{\ell' m'}\rangle_S &= E_\ell N_\ell\delta_{\ell\ell'}\delta_{mm'}, &(2.52)
\end{aligned}$$

where the $\langle|\rangle$ indicates a integral of inside sphere and N_ℓ is given by

$$N_\ell = \int_0^S \left[\dot{u}_\ell(r; E_\ell)\right]^2 r^2 d\mathbf{r}. \tag{2.53}$$

The coefficients $A_{\ell m}^{\alpha,n}$ and $B_{\ell m}^{\alpha,n}$ in Eq. (2.40) is determined by requirements that not only the value of the wave function but also their derivative with respect to the r are continuous on the sphere boundaries. Using an identity of Eq. (2.36), they are written as

$$\begin{aligned} A_{\ell m}^{\alpha,n} &= 4\pi S^2 a_\ell^n Y_{\ell m}^*(\hat{\mathbf{k}}_n), & (2.54)\\ B_{\ell m}^{\alpha,n} &= 4\pi S^2 b_\ell^n Y_{\ell m}^*(\hat{\mathbf{k}}_n), & (2.55) \end{aligned}$$

where

$$\begin{aligned} a_\ell^n &= k_n j_\ell'(k_n S)\dot{u}_\ell(S; E_\ell) - j_\ell(k_n S)\dot{u}_\ell'(S; E_\ell), & (2.56)\\ b_\ell^n &= k_n j_\ell'(k_n S) u_\ell(S; E_\ell) - j_\ell(k_n S) u_\ell'(S; E_\ell). & (2.57) \end{aligned}$$

The u_ℓ' is derivative function with respect to the r, $u_\ell' = \partial u_\ell / \partial r$.

To end, introducing the one-particle wave function, $\psi_{\mathbf{k},b}(\mathbf{r})$, in Eq. (2.33) expanded using the LAPW basis set $\phi_{\mathbf{k}_n}^{\mathrm{LAPW}}$ of Eq. (2.40) into one-electron equation

$$H\psi_{\mathbf{k},b}(\mathbf{r}) = E\psi_{\mathbf{k},b}(\mathbf{r}), \tag{2.58}$$

the secular equation is given in matrix representation,

$$\mathbf{HC} = \mathbf{SCE}. \tag{2.59}$$

The Hermitian matrix elements of the Hamiltonian and overlap integral are

$$\begin{aligned} \{\mathbf{H}\}_{nn'} &= \langle \phi_{\mathbf{k}_n}^{\mathrm{LAPW}} | H | \phi_{\mathbf{k}_{n'}}^{\mathrm{LAPW}} \rangle \\ &= (\mathbf{k}_n \cdot \mathbf{k}_{n'})\, U\,(\mathbf{k}_n - \mathbf{k}_{n'}) \\ &\quad + \frac{4\pi S^2}{\Omega} \sum_\ell (2\ell+1) P_\ell(\mathbf{k}_n \cdot \mathbf{k}_{n'}) \left(E_\ell \mathbf{s}_{\ell,nn'} + \gamma_{\ell,nn'}\right), \end{aligned} \tag{2.60}$$

$$\begin{aligned}\{\mathbf{s}\}_{nn'} &= \langle\phi^{\mathrm{LAPW}}_{\mathbf{k}_n}|\phi^{\mathrm{LAPW}}_{\mathbf{k}_{n'}}\rangle \\ &= U\left(\mathbf{k}_n - \mathbf{k}_{n'}\right) + \frac{4\pi S^2}{\Omega}\sum_{\ell}(2\ell+1)P_\ell(\mathbf{k}_n\cdot\mathbf{k}_{n'})\mathbf{s}_{\ell,nn'}. \end{aligned} \tag{2.61}$$

Here, $U(\mathbf{G})$, $\mathbf{s}_{\ell,nn'}$, and $\gamma_{\ell,nn'}$ are defined as

$$U(\mathbf{G}) = \delta_{\mathbf{G}} - \frac{4\pi S^2}{\Omega}\frac{j_\ell(GS)}{G}, \tag{2.62}$$

$$\mathbf{s}_{\ell,nn'} = a^n_\ell a^{n'}_\ell + b^n_\ell b^{n'}_\ell N_\ell, \tag{2.63}$$

$$\gamma_{\ell,nn'} = \dot{u}_\ell u'_\ell\{k_j j'_{\ell,n} j_{\ell,n'} + j_{\ell,n}k_{n'}j'_{\ell,n}\} - \{\dot{u}_\ell u'_\ell j_{\ell,n}j_{\ell,n'} + \dot{u}_\ell u_\ell k_n j'_{\ell,n}k_{n'}j'_{\ell,n'}\}, \tag{2.64}$$

with the simplification of $j_{\ell,n} = j_\ell(k_n S)$, respectively.

Numerical difficulties, i.e., non-linear secular equation problem, in the APW method are overcome by constructing the LAPW basis set, in which a set of energy parameters equal to corresponding band energies is no longer necessary and the eigenstates are computed from a single diagonarization of Hamiltonian matrix. Because the LAPW basis is introduced a greater flexibility than tha APW method inside spheres, i.e., freedom of two radial functions in LAPWs while only one in APWs, it is expected that the LAPW method can be extended to treat potentials that beyond non-spherical ones. This method is overviewed in next subsection.

2.2.3 Full-potential method and slab calculations

The accuracy of the different shape approximations depends strongly on the system considered. The approach which divides into two spaces of inside MT spheres and the others, i.e., interstitial region, is quite good for close-packed metals. However, it may be difficult to justify its validity for crystals with open structures such as semiconductors and perovskites, reduced symmetry solids such as surfaces and interfaces, or the localized electrons in the oxides and molecules. The full-potential LAPW (FLAPW) method that removes the remaining the MT shape approximation (Fig. 2.2 (b)) is expected to be ideally suited for treating electronic structures of low symmetry and strongly correlated systems.

The FLAPW method is based on the fact that the potential of interstitial region, $V_{\mathrm{int}}(\mathbf{r})$, is

given by the expansion of multipole moment, $q_{\ell m}$, as [114]

$$V_{\rm int}(\mathbf{r}) = \sum_{\ell m} \frac{4\pi}{2\ell+1} q_{\ell m} \frac{Y_{\ell m}(\mathbf{r})}{r^{\ell+1}}, \tag{2.65}$$

where

$$q_{\ell m} = \int_S Y^*_{\ell m}(\mathbf{r}) r^\ell n(\mathbf{r}) d^3\mathbf{r}, \tag{2.66}$$

and on the Dirichlet problem for a sphere.

The potential for the interstitial region depends on only the charge density through the $q_{\ell m}$ in Eq. (2.65), then what we need to get this potential is only the Fourier expansion of the smooth interstitial charge density which is of convergent very well and the multipole moments of the charge density in the MT spheres. According to Weinert [115], because of the fact that the multipole moments do not define a charge density uniquely, true charges in the MT spheres can be replaced with a pseudo-charge density of the same multipole moments, but importantly, the Fourier representation of this pseudo-charge requires to converge rapidly. The pseudo-charge density provides the Coulomb potential everywhere in the interstitial and on the spheres, then, the potential inside the spheres is determined from solving the Dirichlet boundary-value problem using the real charge density in this region. This approach is known as a pseudo-charge method proposed by Weinert in 1981 [115].

In this subsection, the charge density that corresponds to a solution of Poisson's equation solved by Weinert's method and the potential constructed by the obtained charges are summarized. Since this method will be applied to isolated organometallic molecules within the slab model in Chapter 4, the FLAPW formulations extended to two dimensional (2D) film calculations [116–118] is focused.

The solution of the charge density for the 2D slab model (see Fig. 2.3) is given by

$$n(\mathbf{r}) = \begin{cases} \sum\limits_{n} \sum\limits_{s}^{G_{max}} n^{\rm PW}_{\mathbf{k}_n,s} \cos(k_n z) \Phi_s(\mathbf{r}) & \text{(interstitial)} \\ \sum\limits_{\nu} n^{\rm MT}_{\nu}(\mathbf{r}_\alpha) K_{\nu,\alpha}(\hat{\mathbf{r}}_\alpha) - 2Z_\alpha \delta(\mathbf{r}_\alpha) & \text{(inside MT sphere)} \\ \sum\limits_{s}^{G_{max}} n_s(z) \Phi_s(\mathrm{r}) & \text{(vacuum).} \end{cases} \tag{2.67}$$

Here, a 2D pane-wave star function used for the interstitial representation has the full 2D symmetry of the film and is expressed as

$$\Phi_s(\mathbf{r}) = \frac{1}{n_{\text{op}}} \sum_R e^{i\hat{R}\mathbf{G}_s\cdot(\mathbf{r}-\mathbf{t}_R)}, \tag{2.68}$$

where $\mathbf{G}_s$ is a 2D star representative reciprocal lattice vector and summed up to the cut-off G_{max}, $\hat{R}$ are the rotational components of the space group operations, $\{\mathbf{R}|\mathbf{t}_R\}$, $\mathbf{t}_R$ is a non-primitive 2D translation vector, and n_{op} is the number of the space-group operations. Lattice harmonics used for the sphere representation have a form of

$$K_{\nu,\alpha}(\hat{r}) = \sum_m C^{\alpha}_{\nu,m} Y_{\ell_\nu m}(\hat{r}), \tag{2.69}$$

where coefficients $C^{\alpha}_{\nu,m}$ are determined by requirements of non-invariant of the lattice harmonics under the rotations corresponding to the site symmetry and being real functions and orthonormal. The lattice harmonics can be rotated by appropriate rotation matrices,

$$\mathbf{D}(\mathbf{R}) = (-1)^1 P\mathbf{D}(\alpha,\beta,\gamma), \tag{2.70}$$

where α, β, γ are the Euler angles and P is the determinant of $\mathbf{R}$ (1 or -1). The matrices of the $\mathbf{D}(\alpha,\beta,\gamma)$ are given by (see for example Ref. [119])

$$D_{mm'}(\alpha,\beta,\gamma) = e^{-im\alpha} d_{mm'}(\beta) e^{-im'\gamma}, \tag{2.71}$$

where

$$d_{mm'}(\beta) = \sum_t (-1)^t \frac{\sqrt{(\ell+m)!(\ell-m)!(\ell+m')!(\ell-m')!}}{(\ell+m-t)!(\ell-m'+t)!t!(t+m'-m)!} \times \cos^{2\ell+m-m'-2t}\left(\frac{\beta}{2}\right) \sin^{2\ell+m'-m}\left(\frac{\beta}{2}\right) \tag{2.72}$$

with a summation of t that requires non-negative restriction of the factorials in the denominator. The rotations are applied to the real spherical harmonics and summation is carried out over

the operators $\mathbf{R}$ in the local site symmetry,

$$C_m^{(M)} = \begin{cases} \sum_{\mathbf{R}} \left[D_{mM}(\mathbf{R}) + (-1)^M D_{m\bar{M}}(\mathbf{R}) \right] & (M \geq 0) \\ \sum_{\mathbf{R}} i \left[D_{mM}(\mathbf{R}) - (-1)^M D_{m\bar{M}}(\mathbf{R}) \right] & (M < 0). \end{cases} \tag{2.73}$$

The $C^{(M)}$ satisfy the Gramm-Schmidt orthonormalization. Finally, the coefficients except for the zero-norm or linearly dependent values are discarded, then remaining $C^{(M)}$ result in the $C_{\nu,m}$, where ν is a numbering of the survivors [120].

Since the pseudo-charge method is inspired by the fact that the potential outside the MT spheres is not affected by the actual shape of the charge density inside spheres but only on the multipole moments, the violently fluctuated charge inside the MT spheres can be replaced by smoother charge (full pseudo-charge density) with no changes in the potential for the other regions. The charge density expressed by a rapidly converged Fourier expansion of this smooth pseudo charge can be resulted in

$$n(\mathbf{r}) = \sum_G n_G(\mathbf{z}) \Phi_s(\mathbf{r}), \tag{2.74}$$

which may be extremely desired form in an aspect of fast convergence. Once the charge density is obtained from the Poisson's equation, the potential everywhere outside and on the MT spheres are correctly given. Then, description of this potential is extended to the lattice harmonics expansion on the sphere boundaries. This expansion for the potential inside spheres is found from Green's function method using the original charge density and obtained potential on the sphere as a manner of the boundary condition problem. The Coulomb potential for interstitial region is finally obtained as the expansion of [117, 121]

$$V_C(\mathbf{r}) = \sum_G \sum_s^{G_{max}} \tilde{V}_{G,s} \cos(k_n z) \Phi_s(\mathbf{r}) + \sum_{s \neq 0} d_s \cosh(G_s z) \Phi_s(\mathbf{r}). \tag{2.75}$$

Finally, the total potential is given. By performing least-squares fits of the Coulomb potential of Eq. (2.75) and exchange-correlation potential, a three dimensional (3D) or 2D star-function expansion and a lattice harmonics expansion are obtained, respectively. As a result,

the total potential is represented in an analogous manner to the total charge density as

$$V(\mathbf{r}) = \begin{cases} \sum_{n} \sum_{s}^{G_{max}} V^{\mathrm{PW}}_{\mathbf{k}_n,s} \cos(k_n z)\Phi_s(\mathbf{r}) & \text{(interstitial)} \\ \sum_{\nu} V^{\mathrm{MT}}_{\nu}(\mathbf{r}_\alpha) K_{\nu,\alpha}(\hat{\mathbf{r}}_\alpha) - 2Z_\alpha \delta(\mathbf{r}_\alpha) & \text{(inside MT sphere)} \\ \sum_{s}^{G_{max}} V_s(z)\Phi_s(\mathrm{r}) & \text{(vacuum).} \end{cases} \tag{2.76}$$

2.3 +U method for correlation correction

2.3.1 The formulations for DFT+U method

While the LDA and GGA have achieved great successes for describing the electronic behaviors of s and p orbitals, they have found to be insufficient to predict correct electronic and magnetic structures of localized electrons such as d and f orbitals. Particularly, the $3d$ and $4f$ orbitals do not form large (strong) overlaps with the surrounding ligand orbitals and more localized near the corresponding atoms. The orbital energies of $3d$ and $4f$ orbitals may suffer from self-interaction error in the LDA and GGA calculations. As a result, this leads to problematic situation, where the LDA and GGA incorrectly predict ground state, i.e., misunderstanding band gaps, magnetic moments, lattice constants, and so on.

In order to improve this issue, the DFT+U methodology has been first proposed [36] whose basis idea is in the Hubbard model [29–34]. In the Hubbard model, the electron-electron repulsion on a certain atom (site) is quantified by so-called Hubbard on-site Coulomb parameter. Further, Anderson model [66] has been proposed to study magnetic properties of impurity in non-magnetic system based on the Hubbard model. Inspired by these successes, Anisimov *et al.* [36] suggested an additional energy correction term, which is orbital dependent, to the standard DFT energy functional. This originates the DFT+U functionals, in which a screened Hartree-Fock type electron-electron interaction is introduced for localized $3d$ and $4f$ electrons.

So far, in solid state electronic structure community, several implementations for the DFT+U method have been presented, for example, in linear muffin-tin orbitals [36], projector augmented-wave [122], pseudopotential plane-wave [123], full-potential local orbital [124], and linear-combination of pseudo-atomic-orbital [125] methods. In this study, the formulations implemented into the FLAPW method [126] presented by Shick *et al.* was employed.

Total energy functional of the DFT+U in variational form is taken as [67]

$$E_{\rm Total}[n(\mathbf{r}),\hat{n}] = E_{\rm DFT}[n(\mathbf{r})] + E_{\rm ee}(\hat{n}) - E_{\rm dc}(\hat{n}). \tag{2.77}$$

The first term is the usual total energy in the DFT, i.e., LDA or GGA, that is a function of the total electron spin densities with spin index, σ ($\sigma =\uparrow$ or $\downarrow$), as given in Eq. (2.24). $E_{\rm ee}(\hat{n})$ is an electron-electron interaction energy, and $E_{\rm dc}(\hat{n})$ is "double-counting" term that subtracts the electron-electron interaction energy already included in the mean-field approximation.

According to the multiband Hubbard model for d (f) electrons, the $E_{\rm ee}(\hat{n})$ is formed by

$$\begin{aligned} E_{\rm ee}(\hat{n}) = \frac{1}{2} \sum_{m_1,m_2,m_3,m_4} \sum_{\sigma,\sigma'} \quad & n^{\sigma}_{m_1 m_2} \left[\langle m_1, m_3 | V_{\rm ee} | m_2, m_4 \rangle \right. \\ & \left. - \langle m_1, m_3 | V_{\rm ee} | m_2, m_4 \rangle \delta_{\sigma\sigma'} \right] n^{\sigma'}_{m_3 m_4}, \end{aligned} \tag{2.78}$$

where the $V_{\rm ee}$ is an effective on-site Coulomb interaction, and $\langle \ | \ \rangle$ takes over an angular component. The $n^{\sigma}_{m_1 m_2}$ is density matrix for the d (f) orbital at an on-site. Matrix elements of the electron-electron interaction in Eq. (2.78) is expressed in terms of complex spherical harmonics,

$$\langle m_1, m_3 | V_{\rm ee} | m_2, m_4 \rangle = \sum_k a_k(m_1, m_2, m_3, m_4) F^{(k)}, \tag{2.79}$$

where k of $0 \geq k \geq 2\ell$, and

$$a_k(m_1, m_2, m_3, m_4) = \frac{4\pi}{2k+1} \sum_{q=-k}^{k} \langle Y_{\ell m_1} | Y_{kq} | Y_{\ell m_2} \rangle \langle Y_{\ell m_3} | Y^*_{kq} | Y_{\ell m_4} \rangle. \tag{2.80}$$

One can use the Gaunt coefficients

$$\begin{aligned} \langle Y_{\ell m_1} | Y_{kq} | Y_{\ell m_2} \rangle = (-1)^m & \left[\frac{(2\ell+1)(2\ell'+1)(2\ell''+1)}{4\pi} \right]^{1/2} \\ & \times \begin{pmatrix} \ell & \ell' & \ell'' \\ 0 & 0 & 0 \end{pmatrix} \begin{pmatrix} \ell & \ell' & \ell'' \\ -m & m' & m'' \end{pmatrix}. \end{aligned} \tag{2.81}$$

The Slater integral $F^{(k)}$ [127–129] is given by

$$F^{(k)} = \int_0^\infty r_1^2 r_2^2 R_{n\ell}^2(r_1) R_{n\ell}^2(r_2) \frac{r_<^k}{r_>^{k+1}} dr_1 dr_2, \tag{2.82}$$

where $r_>$ and $r_<$ indicate $\max\{r_1, r_2\}$ and $\min\{r_1, r_2\}$, respectively. Here, $R_{n\ell}(r)$ simplifies the radial part of the LAPW basis in Eq. (2.40). Note that, in the $E_{\rm ee}(\hat{n})$ of Eq. (2.78), if $m_1 = m_2 = m_3 = m_4$ and $\sigma = \sigma'$ are satisfied, the self-interaction in the first term is exactly canceled by the exchange interaction in the second term, which is one of the important natures of the DFT+U method.

In the atomic limit, the double-counting energy term is expressed as

$$E_{\rm dc}(\hat{n}) = \frac{U}{2} n(n-1) - \frac{J}{2} \sum_\sigma n^\sigma (n^\sigma - 1), \tag{2.83}$$

where on-site Coulomb interaction U and exchange interaction J parameters may be given by

$$U = \frac{1}{(2\ell+1)^2} \sum_{m_1, m_3} \langle m_1, m_3 | V_{\rm ee} | m_1, m_3 \rangle, \tag{2.84}$$

$$J = U - \frac{1}{2\ell(2\ell+1)} \sum_{m_1, m_3} \left[\langle m_1, m_3 | V_{\rm ee} | m_1, m_3 \rangle - \langle m_1, m_3 | V_{\rm ee} | m_1, m_3 \rangle \right]. \tag{2.85}$$

For the d electrons, only $F^{(0)}$, $F^{(2)}$, and $F^{(4)}$ of Slater integrals are needed to identify the effective on-site U and J in Hartree-Fock-like atomic limit: simply one obtains the U and J through the relations of

$$U = F^{(0)}, \tag{2.86}$$

$$J = \frac{F^{(2)} + F^{(4)}}{14}, \tag{2.87}$$

$$\frac{F^{(2)}}{F^{(4)}} \approx 0.625. \tag{2.88}$$

In Eq. (2.83), the $n^\sigma = {\rm Tr}(\hat{n^\sigma}) = {\rm Tr}(n^\sigma_{mm'})$, and $n = \sum_\sigma n^\sigma$ is a total d (f) on-site occupation numbers. In this study, a simplified scheme corresponding to a limit of $J = 0$ is adopted, or alternatively, the J effects are mimicked redefining the on-site parameters as effective on-site Coulomb interaction, $U_{\rm eff} = U - J$ [130].

2.3.2 Implementation to (F)LAPW method

Using the wave function of Eq. (2.33), with the LAPW basis set given in Eq. (2.40), the spin density is

$$n^{\sigma}(\mathbf{r}) = \sum_{\mathbf{k},b} f_{\mathbf{k},b} \left|\phi^{\sigma}_{\mathbf{k},b}\right|^2, \tag{2.89}$$

where $f_{\mathbf{k},b}$ is the occupations of the state. Matrix elements of density matrix is taken from the projection of the wave function onto $Y_{\ell m}$ subspace,

$$\begin{aligned} n^{\sigma}_{\ell m,\ell' m'} &= \sum_{\mathbf{k},b} f_{\mathbf{k},b} \sum_{\mathbf{G}_{n'},\mathbf{G}_n} c^{\sigma,*}_{\mathbf{G}_n,b} c^{\sigma}_{\mathbf{G}_{n'},b} \\ &\times \int [a^{*,\mathbf{G}_{n'}}_{\ell' m} u^{\sigma}_{\ell'}(r_i) + b^{*,\mathbf{G}_{n'}}_{\ell' m} \dot{u}^{\sigma}_{\ell'}(r_i)] \\ &\times [a^{\mathbf{G}_n}_{\ell m} u^{\sigma}_{\ell}(r_i) + b^{\mathbf{G}_n}_{\ell m} \dot{u}^{\sigma}_{\ell}(r_i)] r^2 dr. \end{aligned} \tag{2.90}$$

Since this expression indicate that the density matrix is not to be diagonal in ℓ, keeping only $\ell' = \ell$ becomes the density matrix as

$$n^{\sigma}_{mm'} = \sum_{\mathbf{k},b} f_{\mathbf{k},b} \sum_{\mathbf{G}_{n'},\mathbf{G}_n} c^{\sigma,*}_{\mathbf{G}_{n'},b} c^{\sigma}_{\mathbf{G}_n,b} \left[a^{\ell m,*}_{\mathbf{G}_{n'}} a^{\ell m}_{\mathbf{G}_n} + b^{\ell m,*}_{\mathbf{G}_{n'}} b^{\ell m}_{\mathbf{G}_n} \langle \dot{u}_{\ell} | \dot{u}_{\ell} \rangle, \right] \tag{2.91}$$

where radial part is integrated. Finally, Eq. (2.91) can be rewritten as

$$n^{\sigma}_{mm'} = \sum_{\mathbf{k},b} f_{\mathbf{k},b} \left[\langle u^{\sigma}_{\ell} Y_{\ell m} | \phi^{\sigma}_{\mathbf{k},b} \rangle \langle \phi^{\sigma}_{\mathbf{k},b} | u^{\sigma}_{\ell} Y_{\ell m'} \rangle + \frac{1}{\langle \dot{u}_{\ell} | \dot{u}_{\ell} \rangle} \langle \dot{u}^{\sigma}_{\ell} Y_{\ell m} | \phi^{\sigma}_{\mathbf{k},b} \rangle \langle \phi^{\sigma}_{\mathbf{k},b} | \dot{u}^{\sigma}_{\ell} Y_{\ell m'} \rangle \right]. \tag{2.92}$$

From the minimization of the defined total energy (Eq. 2.77) with respect to $\psi^{*,\sigma}_i$ using Eq. (2.92) and orthogonality of wave functions [131],

$$\frac{\delta E}{\delta \psi^{*,\sigma}_i} - \frac{\delta \sum e_j f_j \langle \phi^{\sigma}_j | \phi^{\sigma}_j \rangle}{\delta \psi^{*,\sigma}_i} = 0, \tag{2.93}$$

the Kohn-Sham equation for the DFT+U method is formed as

$$\left[-\frac{1}{2}\nabla^2 + V_{\text{eff}} \right] \psi^{\sigma}_i(\mathbf{r}) + \sum_{mm'} V^{\sigma}_{mm'} \frac{\delta n^{\sigma}_{mm'}}{\delta \psi^{*,\sigma}_i} = e^{\sigma}_i \psi^{\sigma}_i(\mathbf{r}). \tag{2.94}$$

The effective potential V_{eff} is the LDA- or GGA-based one-particle potential, and $V^{\sigma}_{mm'}$ which acts only on $Y_{\ell m}$ subspace of the d (f) electron is

$$V^{\sigma}_{mm'} = \sum_{p,q}\sum_{\sigma'} \left(\langle m,p|V_{\text{ee}}|m',q\rangle - \langle m,p|V_{\text{ee}}|q,m'\rangle\delta_{\sigma\sigma'}\right) n^{\sigma'}_{pq} \\ -\delta_{mm'}U\left(n-\frac{1}{2}\right) + \delta_{mm'}J\left(n^{\sigma}-\frac{1}{2}\right). \tag{2.95}$$

Further consideration with Eq. (2.92) provides

$$\frac{\delta n^{\sigma}_{mm'}}{\delta\psi^{*,\sigma}_{i}} = \langle u^{\sigma}_{\ell}Y_{\ell m'}|\psi^{\sigma}_{i}\rangle u^{\sigma}_{\ell}Y_{\ell m'} + \frac{1}{\langle\dot{u}_{\ell}|\dot{u}_{\ell}\rangle}\langle\dot{u}^{\sigma}_{\ell}Y_{\ell m}|\psi^{\sigma}_{i}\rangle\dot{u}^{\sigma}_{\ell}Y_{\ell m'} \tag{2.96}$$

$$= \left[|u^{\sigma}_{\ell}Y_{\ell m'}\rangle\langle u^{\sigma}_{\ell}Y_{\ell m}| + \frac{1}{\langle\dot{u}_{\ell}|\dot{u}_{\ell}\rangle}|\dot{u}^{\sigma}_{\ell}Y_{\ell m'}\rangle\langle\dot{u}^{\sigma}_{\ell}Y_{\ell m}|\right]\psi^{\sigma}_{i} \tag{2.97}$$

where the $\hat{P}^{\sigma}_{mm'}$ is regarded as a projection operator onto mm' subspace.

2.3.3 Second variation procedure

The Kohn-Sham equation in Eq. (2.94) can be solved efficiently by adapting a second variation approach [126]. First of all, one may introduce an auxiliary orthogonal basis set $\{\varphi_{\mathbf{k},b}\}$ which satisfies the standard DFT-based band Hamiltonian within the LDA/GGA,

$$\left[-\frac{1}{2}\nabla^2 + V^{\sigma}_{\text{eff}}\right]\varphi^{\sigma}_{\mathbf{k},b}(\mathbf{r}) = e^{\sigma}_{\mathbf{k},b}\varphi^{\sigma}_{\mathbf{k},b}(\mathbf{r}). \tag{2.98}$$

Note that the function $\varphi_{\mathbf{k}}$ seems to be DFT wave functions, but the charge density made by them never goes into V^{σ}_{eff}, thus, this function differs from the DFT eigenstates. In the second variation method, a solution of the DFT+U at i-th state, $\psi^{i}_{\mathbf{k}}$, can be expanded by auxiliary functions, $\varphi_{\mathbf{k}}$, as

$$|\psi^{i}_{\mathbf{k}}\rangle = \sum_{j} d^{i}_{j}|\varphi_{\mathbf{k},j}\rangle. \tag{2.99}$$

In term with the basis of Eq. (2.99), the Kohn-Sham equation is transformed from Eq. (2.94) to the following:

$$\sum_j \varepsilon_j d_j^i |\varphi_j\rangle + \sum_j d_j^i \sum_{mm'} [V_{mm'}^\sigma \langle u_\ell^\sigma Y_{\ell m}|\varphi_j\rangle \dot{u}_\ell^\sigma(r) Y_{\ell m'}(r) + \langle \dot{u}_\ell^\sigma Y_{\ell m}|\varphi_j\rangle u_\ell^\sigma(r) Y_{\ell m'}(r) / \langle \dot{u}_\ell|\dot{u}_\ell\rangle] = e_i \sum_j d_j^i |\varphi_j\rangle, \tag{2.100}$$

Here, the second-variation Hamiltonian that satisfies a secular equation

$$\sum_j (H_{\mathrm{DFT+U}})_{jj'} d_{j'}^i = e_i d_{j'}^i, \tag{2.101}$$

is of form as

$$(H_{\mathrm{DFT+U}})_{jj'}^\sigma = \varepsilon_j \delta_{j'j} + \sum_{mm'} [\langle \psi_{j'}|u_\ell^\sigma Y_{\ell m'}\rangle V_{mm'}^\sigma \langle u_\ell^\sigma Y_{\ell m'}|\psi_{j'}\rangle + \langle \psi_{j'}|\dot{u}_\ell^\sigma Y_{\ell m'}\rangle V_{mm'}^\sigma \langle \dot{u}_\ell^\sigma Y_{\ell m'}|\psi_{j'}\rangle / \langle \dot{u}_\ell^\sigma|\dot{u}_\ell^\sigma\rangle]. \tag{2.102}$$

The orthogonality relation $\langle \psi_i|\psi_j\rangle = \delta_{ij}$ is used.

A flowchart for solving the DFT+U-based Kohn-Sham equations by second variation procedure is shown in Fig. 2.4. The self-consistent solution of Eq. (2.94) is calculated as follows.

(i) To get an orthogonal and auxiliary basis set, the Eq. (2.98) for a given DFT effective potential is solved.

(ii) By employing this basis set, one solves the Eq. (2.100) (and Eq. (2.101)) where the DFT+U Hamiltonian is expressed by Eq. (2.102) to obtain the variational coefficients d_j^i. This d_j^i is needed in Eq. (2.99) to constructs the solution of DFT+U.

(iii) The new DFT+U wave function is projected back to the LAPW basis set to calculate the charge and spin densities up to achieving a self-consistent solution at the end.

2.4 Linear response calculations using constraint density functional theory

As it was explained in Chapter 1, several methods have been proposed to determine the (effective) on-site Coulomb (and exchange) interaction [36, 86–88, 90, 91, 93, 132–134]. In this thesis, a linear response approach, presented by Cococcioni and de Gironcoli [90, 135], is employed. This approach is minimally extended from the limited LDA scheme and accomplishes that the derived parameter excludes energy contributions of one-electron kinetic term. In this method, which was inspired originally by the linear response scheme studied by Pikett and coworkers [86], the d-electron occupations are constrained to vary around the unconstrained LDA- or GGA-result to calculate the U_{eff} value.

Firstly, the mean-field total energy as a function of the total d (f)-orbital occupancy at localized site α, $E[\{n_d^\alpha\}]$, is considered. Then, the second derivative of the total energy with respect to the d-occupancy, $\partial E^2[\{n_d^\alpha\}]/\partial \left(n_d^\alpha\right)^2$, is numerically calculated. However, this quantity does not correspond to the U_{eff} because it includes a non-related one-electron kinetic contribution. [90,135,136] The kinetic energy contribution is not originated from the electron-electron interaction, and it also includes a quadratic behavior of non perturbed sites, i.e., re-hybridization of atomic orbitals and/or possible itinerant valence electrons. Strictly speaking, it is correctly taken into account in LDA (GGA) and not a quantity to be corrected by the +U method. Thus, including it into the on-site U_{eff} leads to a double counting error.

Accordingly, in this approach, the effective on-site Coulomb interaction U_{eff} is calculated from the difference between the second derivatives of the total energies as

$$U_{\text{eff}} = \frac{\partial^2 E[\{n_d^\alpha\}]}{\partial \left(n_d^\alpha\right)^2} - \frac{\partial^2 E^{\text{KS}}[\{n_d^\alpha\}]}{\partial \left(n_d^\alpha\right)^2}, \tag{2.103}$$

where $E[\{n_d^\alpha\}]$ and $E^{\text{KS}}[\{n_d^\alpha\}]$ are the self-consistent-field (SCF) and non-interacting (non-self-consistent) Kohn-Sham (KS) total energiges. The second term subtracts the contributions for the non-interacting Kohn-Sham problem from the SCF result because the derivative of $E[\{n_d^\alpha\}]$ includes a part that does not related to electron-electron interaction but attributing tod a kinetic contribution. [90, 135, 136]

The evaluation of the U_{eff} for the d electron is obtained in constraint DFT (CDFT) ap-

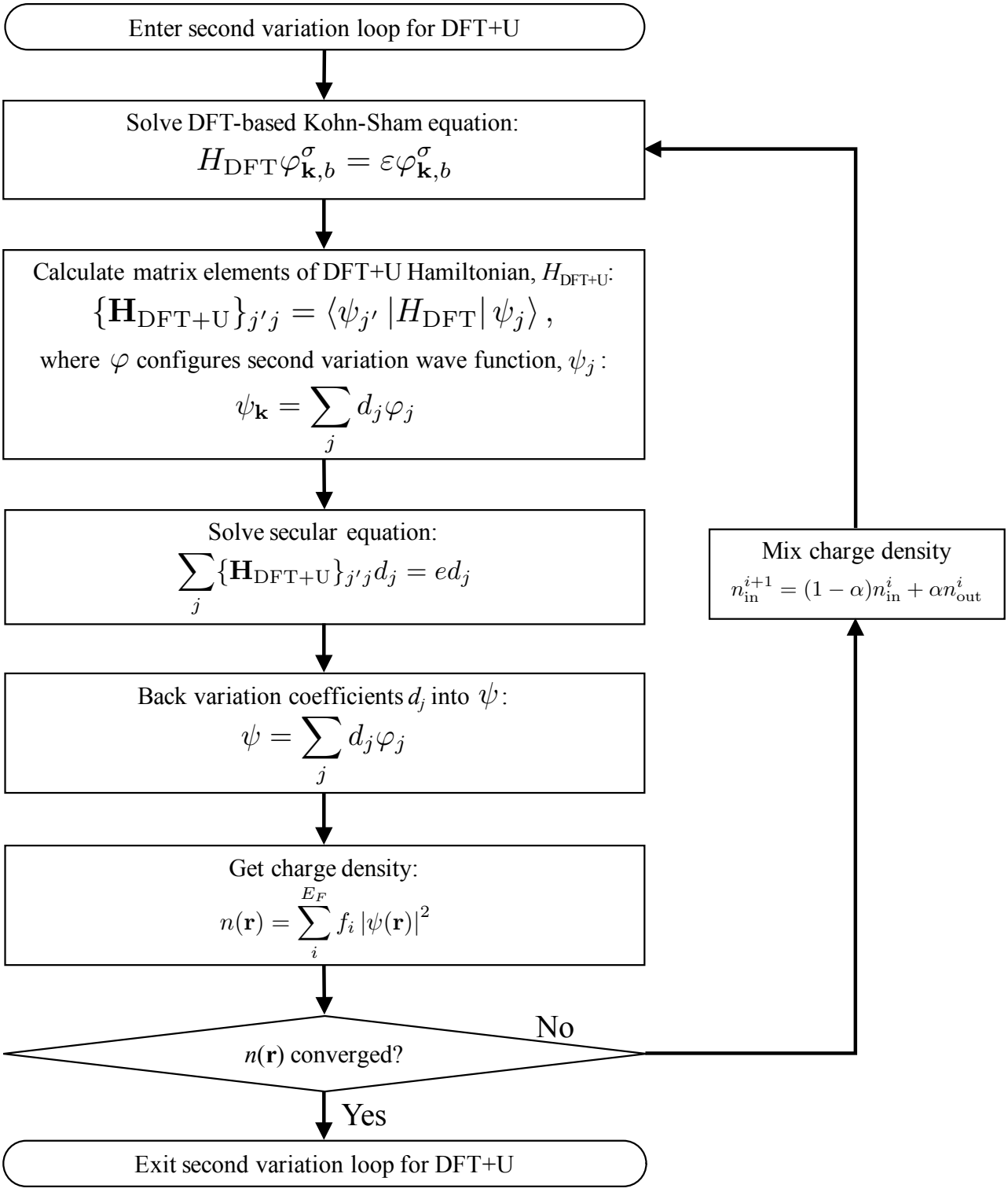

Figure 2.4: Flowchart of the second variation method for DFT+U calculations.

proach [74, 137–139]. By adding a general constraint

$$n^{\alpha}_{mm} = N^{\alpha}_{mm}, \tag{2.104}$$

a total energy functional for the CDFT is formed as

$$E_{\mathrm{CDFT}}[n(\mathbf{r}), n^{\alpha}_{mm}] = E_{\mathrm{DFT}}[n(\mathbf{r})] + \sum_{m} \mu^{\alpha}_{mm} \left(n^{\alpha}_{mm} - N^{\alpha}_{mm}\right), \tag{2.105}$$

where a constraint field (Lagrange multiplier), μ^{α}_{mm}, that can be denoted as a field to constrain the density matrix is introduced. The m is magnetic quantum number of $-2 \sim 2$ for the d orbital. The $E_{\mathrm{DFT}}[n(\mathrm{r})]$ is the total energy functional in the DFT, n^{α}_{mm} is a standard density matrix of the d orbitals of an atom α, and N^{α}_{mm} is a desired occupation number that should be constrained.

In order to derive the U_{eff}, the DFT total energy as a function of the d-orbital occupation numbers at site α, $E[\{n^{\alpha}_{d}\}]$ is constructed. Instead of calculating the $E[\{n^{\alpha}_{d}\}]$, in the present study, we calculate directly the energy difference with respect to a reference state, i.e., ground state. By taking an advantage from Hellmann-Feynman theorem [140, 141], derivation of the total energy $E[\{n^{\alpha}_{d}\}]$ is obtained as

$$\frac{\partial E[\{n^{\alpha}_{d}\}]}{\partial n^{\alpha}_{d}} = -\mu, \tag{2.106}$$

and, in the same way, the KS term is

$$\frac{\partial E^{\mathrm{KS}}[\{n^{\alpha}_{d}\}]}{\partial n^{\alpha}_{d}} = -\mu^{\mathrm{KS}}. \tag{2.107}$$

Further derivative gives

$$\frac{\partial^2 E[\{n^{\alpha}_{d}\}]}{\partial n^{\alpha}_{d}} = -\frac{\partial \mu}{\partial n^{\alpha}_{d}}, \tag{2.108}$$

$$\frac{\partial^2 E^{\mathrm{KS}}[\{n^{\alpha}_{d}\}]}{\partial n^{\alpha}_{d}} = -\frac{\partial \mu^{\mathrm{KS}}}{\partial n^{\alpha}_{d}}. \tag{2.109}$$

In practice, the interaction and non-interaction density matrices,

$$\chi_{\beta\alpha} = \frac{\partial n_\beta}{\partial \mu_\alpha}, \tag{2.110}$$

$$\chi^{\mathrm{KS}}_{\beta\alpha} = \frac{\partial n_\beta}{\partial \mu^{\mathrm{KS}}_\alpha} \tag{2.111}$$

are introduced, where n_β is the occupation number at site β when constraint μ_α is applied at site α. The derivatives are numerically computed; χ^{KS}, which does not include screening, is obtained from the first iteration in the self-consistent calculation loop starting from the DFT self-consistent charge density. Then the U_{eff} in Eq. (2.103) is estimated as

$$U^\alpha_{\mathrm{eff}} = -\frac{\partial \mu_\alpha}{\partial n^\alpha_d} - \left(-\frac{\partial \mu^{\mathrm{KS}}_\alpha}{\partial n^\alpha_d}\right) = \left(\chi^{-1}_{\mathrm{KS}} - \chi^{-1}\right)_{\alpha\alpha}. \tag{2.112}$$

The U^α_{eff} value at site α should be calculated by considering a large enough number of neighbor atoms from the corresponding perturbed site to exclude artifacts arising from periodic boundary condition and implicity in the calculations of the inverse of response function matrices. [90, 135, 136] Practically, super-cells with increasing size, i.e., repeating the linear response calculations for larger and lager unit- or super-cells, are introduced up to the U_{eff} value reasonably converged. This means that, as shown in Fig. 2.5, the charge re-distribution dominating the screening from more and more distant non-perturbed neighbors can be treated.

Further, it is useful to include any other overall charge behaviors, for example, that of precise s and p states of the strongly correlated Hubbard site and the possible itinerant electrons in the interstitial region, as well as that of the localized-orbital occupation numbers of non-perturbed sites. [136] This can be easily done by introducing one more column and one more row in the linear response matrices. In this context, the size of matrix of both χ and χ^{KS} are built with $(M+1)\times(M+1)$ matrix, but not $M \times M$, in which M denotes the number of Hubbard atom site under consideration in the employed unit- or super-cell. A schematic of this is shown in Fig. 2.6. These additional degrees of freedom are determined by a requirement that a charge neutrality preserves in whole the space: thus, $\sum_\alpha(\partial n_\beta/\partial\mu_\alpha) = \sum_\beta(\partial n_\beta/\partial\mu_\alpha) = 0$. Note that, from the viewpoint of mathematics, a simple strategy is needed to avoid ill-defined inversion matrices of $(M+1)\times(M+1)$-sized χ and χ^{KS}. Briefly, a same amount of γ is added to all matrix elements to shift the null eigenvalue (see Ref. [136] for more detail).

Now, the variation principle is applied to the total energy in Eq. (2.105). To minimize the $E_{\mathrm{CDFT}}[n(\mathbf{r}), n^{\alpha}_{mm}]$ under the orthonormality $\langle\psi_i|\psi_j\rangle = \delta_{ij}$, according to the general procedure, another Lagrange multiplier, ε_i, is used to built a function

$$\tilde{E} = E_{\mathrm{CDFT}}[n(\mathbf{r}), n^{\alpha}_{mm}] - \sum_{i}^{N} \varepsilon_i \left(\langle\psi_i|\psi_j\rangle - \delta_{ij}\right) \tag{2.113}$$

$$= E_{\mathrm{DFT}}[n(\mathbf{r})] + \sum_{m} \mu^{\alpha}_{mm}(n^{\alpha}_{mm} - N^{\alpha}_{mm}) - \sum_{i}^{N} \varepsilon_i \left(\langle\psi_i|\psi_j\rangle - \delta_{ij}\right). \tag{2.114}$$

Then, eigencondition $\delta\tilde{E}/\delta\psi^*_i = 0$ gives

$$\frac{\delta\tilde{E}}{\delta\psi^*_i} = \frac{\delta E_{\mathrm{DFT}}[n]}{\delta\psi^*_i} + \frac{\delta}{\delta\psi^*_i}\sum_{m} \mu^{\alpha}_{mm}(n^{\alpha}_{mm} - N^{\alpha}_{mm}) - \frac{\delta}{\delta\psi^*_i}\sum_{i}^{N} \varepsilon_i \left(\langle\psi_i|\psi_j\rangle - \delta_{ij}\right) \tag{2.115}$$

$$= H_{\mathrm{DFT}}\psi_i + \sum_{m} \mu^{\alpha}_{mm}\frac{\delta n^{\alpha}_{mm}}{\delta\psi^*_i} - \varepsilon_i\psi_i = 0 \tag{2.116}$$

Thus, the Kohn-Sham equations can be written in the form

$$\left[H_{\mathrm{DFT}} + \sum_{m} \mu^{\alpha}_{mm}\hat{P}^{\alpha}_{mm}\right]\psi_i = \varepsilon_i\psi_i, \tag{2.117}$$

where the projection operator onto the mm subspace in the LAPW basis is given, in the same way as Eq. (2.97), by

$$\hat{P}^{\alpha}_{mm} = |u^{\alpha}_{\ell}Y_{\ell m}\rangle\langle u^{\alpha}_{\ell}Y_{\ell m}| + \frac{1}{\langle\dot{u}_{\ell}|\dot{u}_{\ell}\rangle}|\dot{u}^{\alpha}_{\ell}Y_{\ell m}\rangle\langle\dot{u}^{\alpha}_{\ell}Y_{\ell m}|, \tag{2.118}$$

and the density matrix n^{α}_{mm} is

$$n^{\alpha}_{mm} = \sum_{\mathrm{k},b} f_{\mathrm{k},b}\langle\psi_{\mathrm{k},b}|\hat{P}^{\alpha}_{mm}|\psi_{\mathrm{k},b}\rangle. \tag{2.119}$$

In practice, we specify a set of constrained fields μ^{α}_{n} along the direction of the eigenvectors of n^{α}_{mm}. Then, the μ^{α}_{mm}s, which are rotated back from the μ^{α}_{n}s are introduced in Eq. (2.117), and the corresponding n^{α}_{mm}s are determined self-consistently. The total energy is calculated using Eq. (2.105) with $N^{\alpha}_{mm} = n^{\alpha}_{mm}$. Figure 2.7 finally summarizes procedures to compute the U_{eff} in the linear response calculations.

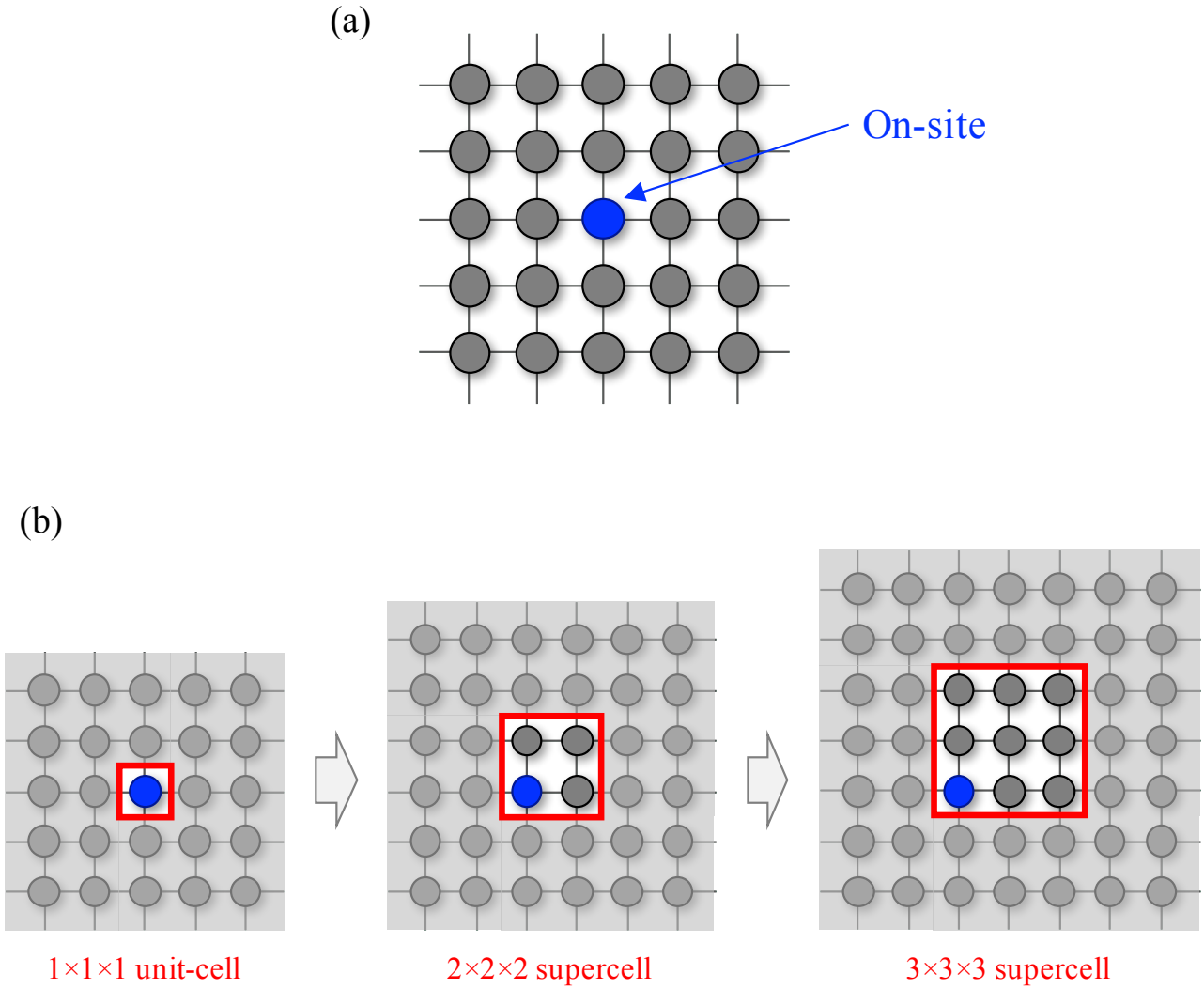

Figure 2.5: (a) On-site atom in periodic system. Blue circle shows an on-site atom, where d electrons are localized, and gray circles show itinerant electron sites which is preferred by non-metal atoms possessing s and p electrons. (b) Schematics of the supercells which eliminates periodic boundary condition effects from on-site atom used in the calculations of the U_{eff}. Red squares are considered unit cells in $1 \times 1 \times 1$ (left panel), $2 \times 2 \times 2$ (center), and $3 \times 3 \times 3$ (right), respectively.

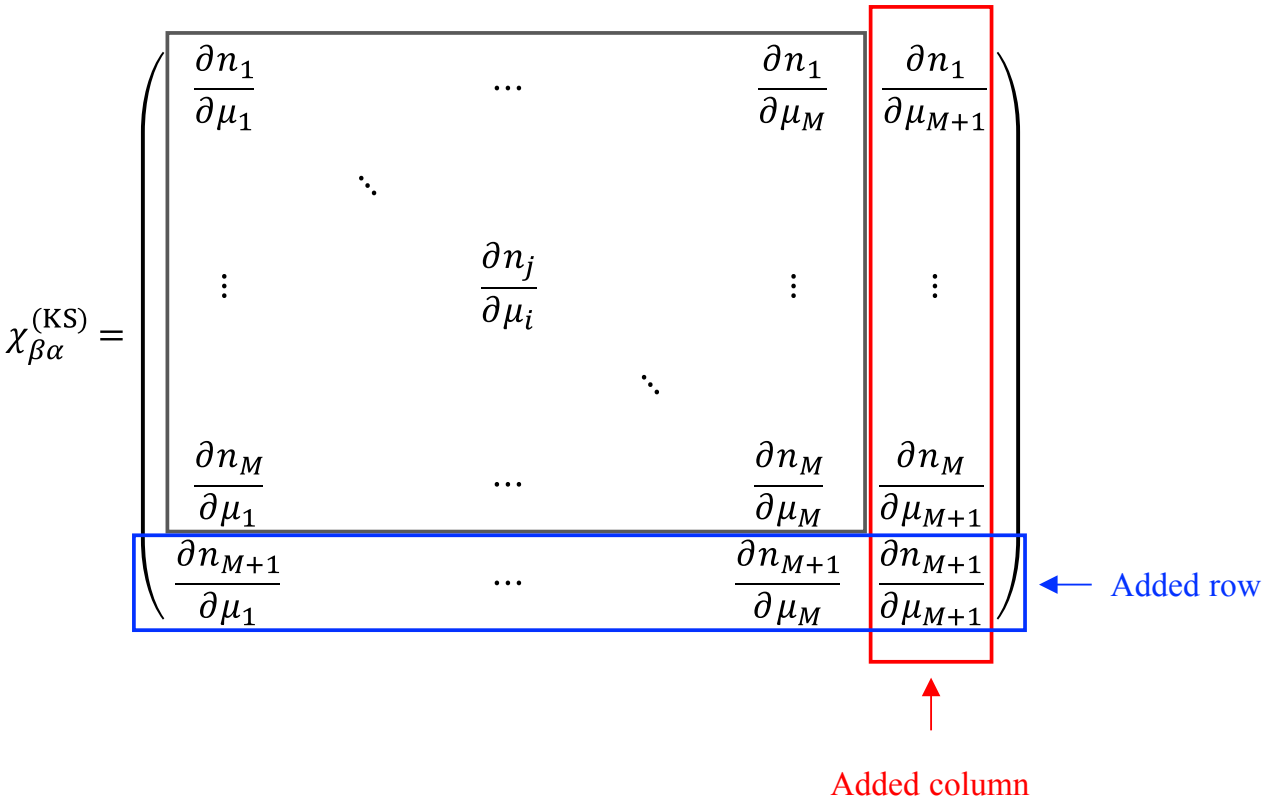

Figure 2.6: Schematic of matrix elements for response matrices, $\chi^{(\mathrm{KS})}$. The $(M+1) \times (M+1)$ matrix is constructed by adding one more column (red square) and one more row (blue) for efficient calculations considering effects from the non-Hubbard atom sites.

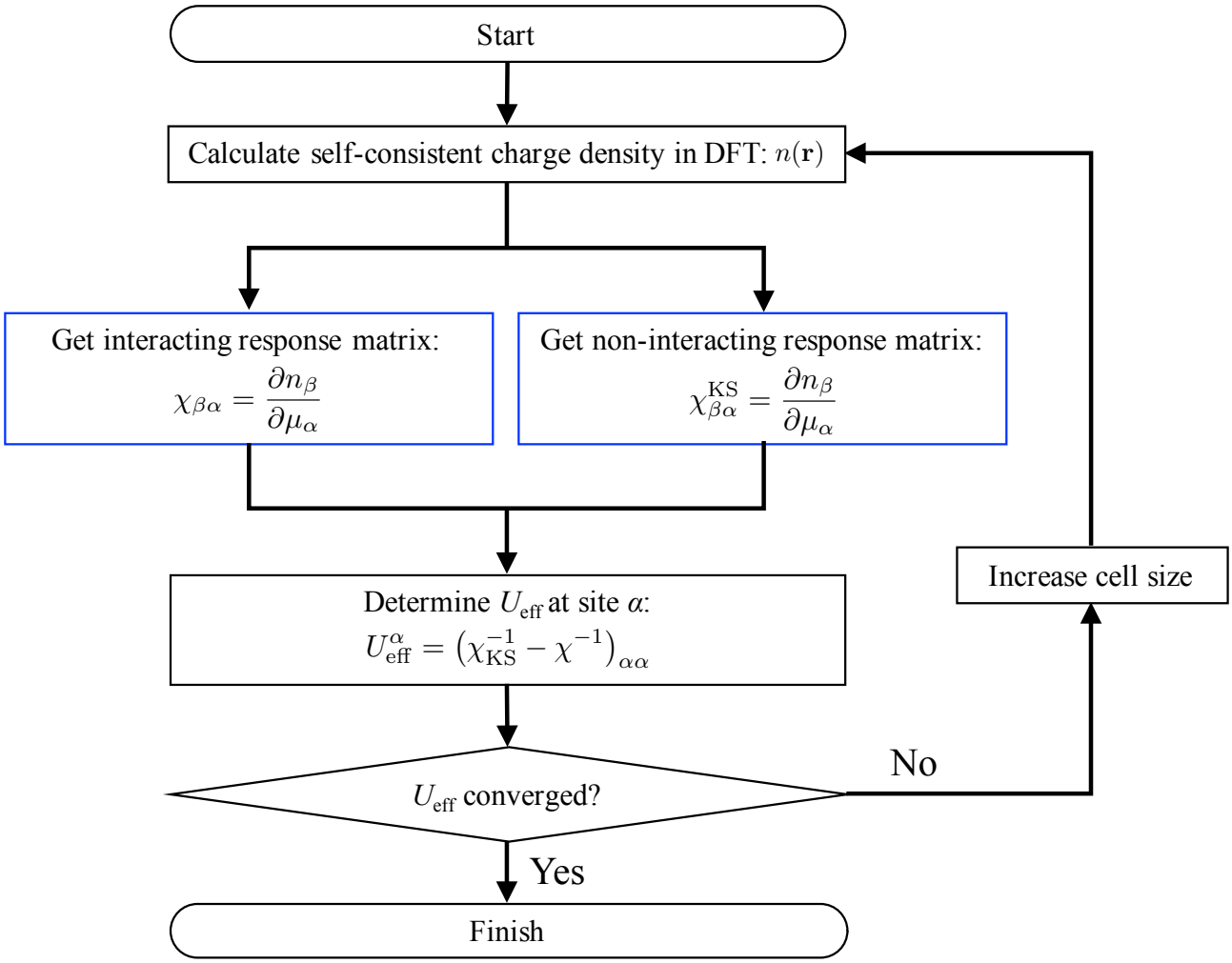

Figure 2.7: Flowchart for the linear response calculations of the U_{eff}. At blue colored step, cDFT approach is adopted to get the response functions χ by applying constraint field to the d-level occupancy.

2.5 Kohn-Sham-Dirac equation and scalar relativistic approximation

If the electrons are close to the nuclei and their motions are dominated by large kinetic contributions, the relativistic effect should not be neglected. Basically, the electrons inside MT spheres should be treated relativistically, while those in interstitial (and vacuum) regions may be non-relativistically. The Kohn-Sham equation, in which the relativistic effects are not considered, is extended to a single particle Dirac-equation, i.e., Kohn-Sham-Dirac equation, as

$$\{c\alpha \cdot \mathbf{p} + (\beta - 1)mc^2 + V_{\text{eff}}(\mathbf{r})\}\psi_i = \varepsilon\psi_i. \tag{2.120}$$

The vector operator α is 4×4 matrix whose components are written using the Pauli-spin matrices, $\sigma_{\mathbf{r}}$, as

$$\alpha = \begin{pmatrix} 0 & \sigma_{\mathbf{r}} \\ \sigma_{\mathbf{r}} & 0 \end{pmatrix}, \tag{2.121}$$

where the standard Pauli matrices' representations are

$$\sigma_x = \begin{pmatrix} 0 & 1 \\ 1 & 0 \end{pmatrix}, \quad \sigma_y = \begin{pmatrix} 0 & i \\ -i & 0 \end{pmatrix}, \quad \sigma_z = \begin{pmatrix} 1 & 0 \\ 0 & -1 \end{pmatrix}. \tag{2.122}$$

The $\mathbf{p}$ is the momentum operator, $\mathbf{p} = -i\hbar\nabla$, and the β matrix is represented with $(n \times n)$ unit matrix $\mathbf{I}_n$ as

$$\beta = \begin{pmatrix} \mathbf{I}_2 & 0 \\ 0 & -\mathbf{I}_2 \end{pmatrix}. \tag{2.123}$$

Quantities of m and c are electron mass and the speed of light, respectively. In the relativistic Dirac equations, the quantum numbers of ℓ, m, and s are no longer the "good" quantum numbers due to the effect of spin-orbit coupling (SOC), instead, these values are replaced by the quantum numbers of κ and μ. The κ and μ are respective eigenvalues of the operator of K,

$$K = \beta\,(\sigma \cdot \ell)\,, \tag{2.124}$$

and that of total angular momentum $\mathbf{j}$ (and j_z): $\mathbf{j}$ is sum of ℓ and s,

$$\mathbf{j} = \ell + \mathbf{s}. \tag{2.125}$$

In the $\kappa\mu$ space, eigenstates inside the MT spheres, ψ_i, in a central-force potential in Eq. (2.120) are four component wave functions and of the form of

$$\psi_i(\mathbf{r}) = \psi_{\kappa,\mu}(\mathbf{r}) = \begin{bmatrix} g_\kappa(\mathbf{r})\chi_{\kappa\mu} \\ -if_\kappa(\mathbf{r})\sigma_r\chi_{\kappa\mu} \end{bmatrix}, \tag{2.126}$$

where $g_\kappa(\mathbf{r})$ and $f_\kappa(\mathbf{r})$ are called as large and small components, respectively. Functions of spin angular, $\chi_{\kappa\mu}$, are eigenfunctions of $\mathbf{j}, j_z, K$, and S^2 with eigenvalues of j, μ, κ, and $s = 1/2$, respectively, and can be expanded into a sum of product of spherical harmonics and Pauli spinors with the Clebsh-Gordan coefficients as their expansion coefficients. The large and small components satisfy the following set of radial equations:

$$f'_\kappa(r) = \frac{1}{c}(V_{\text{eff}} - E)g_\kappa(r) + \left(\frac{\kappa - 1}{r}\right) f_\kappa(r), \tag{2.127}$$

$$g'_\kappa(r) = \left(\frac{\kappa + 1}{r}\right) g_\kappa(r) + 2Mcf_\kappa(r), \tag{2.128}$$

with the relativistic mass $M = m + (E - V_{\text{eff}}(\mathbf{r}))/(2c^2)$. In these equations, the prime indicates the differentiation with respect to radial r, i.e., $f'_\kappa = \partial f_\kappa/\partial r$, $g'_\kappa = \partial g_\kappa/\partial r$, and the energy E is defined as $E = mc^2$. Solving Eq. (2.128) for $f_\kappa(r)$ and substituting it into Eq. (2.127), we obtain

$$-\frac{1}{2M}\left[g''_\kappa + \frac{2}{r}g'_\kappa - \frac{\ell(\ell+1)}{r^2}g_\kappa\right] - \frac{V'g_\kappa}{4M^2c^2} - \frac{\kappa+1}{r}\frac{V'g_\kappa}{4M^2c^2} = Eg_\kappa. \tag{2.129}$$

Second term including $(dV/dr)(dg/dr)$ in left-hand side is known as the Darwin term, and third term is the SOC term, which depends on the sign of κ number: the κ is given as

$$\kappa = \begin{cases} \ell & \text{for } j = \ell + 1/2 \\ -(\ell+1) & \text{for } j = \ell - 1/2. \end{cases} \tag{2.130}$$

When these two terms can be ignored, the Eq. (2.129) seems to be a radial Schrödinger equation. One may get the g_κ from the Eq. (2.129) keeping the spin quantum number as a good

quantum number, but typically it is difficult to solve with highly precision. Moreover, the small component f_κ may be of importance in calculations for core-state charge density as well. In 1977, Kölling and Harmon overcame this difficulty so as to introduce relativistic effects into practical band structure calculations [142].

In scalar-relativistic approximation (SRA) that was established by Kölling and Harmon [142], the effect of the SOC can be treated as a perturbation after the relativistic spin-polarized based bands and wave functions are obtained. Thus, this approach can be regarded as reduction of the Dirac equation, in which the SOC is initially omitted while other relativistic effects are included, the second variation procedure. The advantage in this approach is that the spin quantum number can be still kept as a "good" quantum number.

To derive the SRA solution, a new function ϕ_κ(r) is defined

$$\phi_\kappa(r) = \frac{1}{2Mc} g'_\kappa, \tag{2.131}$$

then the $f_\kappa(r)$ is given as

$$f_\kappa(r) = \phi_\kappa + \frac{\kappa+1}{2Mcr} g_\kappa. \tag{2.132}$$

Using Eq. (2.131) and (2.132), we can rewrite Eq. (2.127) and (2.128)

$$g'_\kappa = 2Mc\phi_\kappa, \tag{2.133}$$

$$\phi'_\kappa = -\frac{2}{r}\phi_\kappa + \left[\frac{\ell(\ell+1)}{2Mcr^2} + \frac{1}{c}(V-E) + \frac{\kappa+1}{2Mc^2 r} M'\right] g_\kappa, \tag{2.134}$$

where an identity $\kappa(\kappa+1) = \ell(\ell+1)$ is used. The term $(\kappa+1)M'/2Mc^2r$ is identified as the SOC which is dropped in the RSA because it is the only one term being coupling with both spin-up and -down. Note that the M' denotes $M' = \partial M/\partial r$.

Now, the wave functions of Eq. (2.126) can be rewritten as

$$\psi_i(\mathbf{r}) = \psi_{\kappa,\mu}(\mathbf{r}) \approx \begin{bmatrix} g_\ell \chi_{\kappa\mu} \\ -if_\ell \left(\phi_\ell + \frac{\kappa+1}{2Mcr}\right) \sigma_r \chi_{\kappa\mu} \end{bmatrix}, \tag{2.135}$$

where the Eq. (2.132) is used to replace the small component radial function f_ℓ. The κ numbers are combined with appropriate Clebsh-Gordan coefficients to get a familiar non-relativistic

quantum-number-based wave function

$$\psi_{\ell ms}(\mathbf{r}) = \begin{bmatrix} g_\ell Y_{\ell m}\chi_s \\ \frac{i}{2Mc}\sigma_r \left(-g'_\ell + \frac{1}{r}g_\ell \sigma \cdot \mathbf{L}\right) Y_{\ell m}\chi_s \end{bmatrix}, \tag{2.136}$$

with the usual spin-up and down spinors, χ_s. What we can see from obtained wave function of Eq. (2.136) is that the large component is formed by pure spin function while the small component has some mixture of spins. Because the g_ℓ includes most of the relativistic corrections, neglecting the small component may give a simple solution, however, particularly in the atomic calculation, the small component contribution is necessary for well-description of the core charge density. In this context, these calculations are approached using the second variation method.

Now new functions defined by

$$P_\ell = r g_\ell, \tag{2.137}$$

$$Q_\ell = rc\phi_\ell \tag{2.138}$$

can rewrite Eq. (2.133) and (2.134) as

$$P'_\ell = 2McQ_\ell + \frac{1}{r}P_\ell \tag{2.139}$$

$$Q'_\ell = -\frac{1}{r}Q_\ell + \left[\frac{\ell(\ell+1)}{2Mr^2}\right] P_\ell. \tag{2.140}$$

By this transformation, the wave function reformulated from Eq. (2.136) to

$$\psi_{\ell ms}(\mathbf{r}) = \frac{1}{r}\begin{bmatrix} P_\ell Y_{\ell m}\chi_s \\ -i\mathbf{r}\cdot\sigma_r \left(-Q_\ell + \frac{P_\ell}{2Mcr}\sigma \cdot \mathbf{L}\right) Y_{\ell m}\chi_s \end{bmatrix} \tag{2.141}$$

is determined by following the procedures of the second variation method [142].

The Hamiltonian including the relativistic SOC contribution whose eigenfunctions are determined by the second variation technique is

$$H = H_0 + H_{\mathrm{SO}}, \tag{2.142}$$

where H_0 is standard Hamiltonian within the non-relativistic LDA or GGA and $H_{\rm SO}$ is the SOC term defined by

$$H_{\rm SO} = \sum_i \xi(r_i)\sigma \cdot \mathbf{L}, \tag{2.143}$$

$$\xi(r_i) = \frac{\hbar}{(2Mc)^2}\frac{1}{r_i}\frac{dV(r_i)}{dr_i}. \tag{2.144}$$

Figure 2.9 shows a calculation flowchart of the second variation method for treating the SOC, which may follow similar procedure to the one described in the DFT+U section (see section 2.4). Before entering the second variation-based SCF loop, spin quantization axis can be rotated by angles of θ and ϕ by Euler angle (see Fig. 2.8) using 2×2 rotation matrix U,

$$U = U(\theta, \phi) = \begin{pmatrix} \cos\frac{\theta}{2} & \sin\frac{\theta}{2} \\ -\sin\frac{\theta}{2} & \cos\frac{\theta}{2} \end{pmatrix} \begin{pmatrix} e^{i\frac{\phi}{2}} & 0 \\ 0 & e^{i\frac{\phi}{2}} \end{pmatrix}. \tag{2.145}$$

The term $\sigma \cdot \mathbf{L}$ in Eq. (2.143) can be expressed as

$$\sigma \cdot \mathbf{L} = \sigma(\theta, \phi) \cdot \mathbf{L} \tag{2.146}$$

$$= U(\theta, \phi)\sigma \cdot \mathbf{L}U^{\dagger}(\theta, \phi). \tag{2.147}$$

The relativistic Kohn-Sham-Dirac equations for single-particle electron states can be solved by following steps:

(i) Scalar-relativistic one-electron wave functions, $\varphi^{\rm RSA}$, are determined from conventional Kohn-Sham equation,

$$H_{\rm DFT}\varphi^{\rm RSA} = \varepsilon\varphi^{\rm RSA}, \tag{2.148}$$

where the SOC effect is not considered.

(ii) By assuming second variation wave function, ψ, with variation coefficients, $\{d_j\}$,

$$\psi = \sum_j d_j\varphi^{\rm RSA}, \tag{2.149}$$

the matrix elements of full-relativistic Hamiltonian including $H_{\rm SO}$ are calculated:

$$\{\mathbf{H}\}_{j'j} = \varepsilon\langle\varphi^{\rm RSA}_{j'}|\varphi^{\rm RSA}_{j}\rangle + \langle\varphi^{\rm RSA}_{j'}|H_{\rm SO}|\varphi^{\rm RSA}_{j}\rangle \tag{2.150}$$

$$= \varepsilon\delta_{j'j} + \langle\varphi^{\rm RSA}_{j'}|H_{\rm SO}|\varphi^{\rm RSA}_{j}\rangle. \tag{2.151}$$

The latter term is derived as

$$\langle\varphi^{\rm RSA}_{j'}|H_{\rm SO}|\varphi^{\rm RSA}_{j}\rangle = \sum_{\ell'\ell}\sum_{m'm} i^{\ell-\ell'}\langle Y^{\sigma'}_{\ell m'}\chi^{\sigma'}|\ell\cdot\mathbf{s}|Y^{\sigma}_{\ell m}\chi^{\sigma}\rangle D^{\sigma'\sigma}_{\ell,m'm,j'j}, \tag{2.152}$$

where

$$\begin{aligned} D^{\sigma'\sigma}_{\ell,m'm,j'j} = \delta_{\ell'\ell}\Bigg[&\left(A^{\sigma'}_{\ell'm',j'}\right)^* A^{\sigma}_{\ell m,j}\int\xi(r)u^{\sigma'}_{\ell'}u^{\sigma}_{\ell}r^2d\mathbf{r} \\ &+\left(A^{\sigma'}_{\ell'm',j'}\right)^* B^{\sigma}_{\ell m,j}\int\xi(r)u^{\sigma'}_{\ell'}\dot{u}^{\sigma}_{\ell}r^2d\mathbf{r} \\ &+\left(B^{\sigma'}_{\ell'm',j'}\right)^* A^{\sigma}_{\ell m,j}\int\xi(r)\dot{u}^{\sigma'}_{\ell'}u^{\sigma}_{\ell}r^2d\mathbf{r} \\ &+\left(B^{\sigma'}_{\ell'm',j'}\right)^* B^{\sigma}_{\ell m,j}\int\xi(r)\dot{u}^{\sigma'}_{\ell'}\dot{u}^{\sigma}_{\ell}r^2d\mathbf{r}\Bigg] \end{aligned} \tag{2.153}$$

.

(iii) Relativistic Hamiltonian is diagonalized to get the eigenvalues e from

$$\sum_j\{\mathbf{H}\}_{j'j}d_j = ed_j, \tag{2.154}$$

and the eigenfunctions ψ is again projected back to Eq. (2.149), and continue these cycles (i) $\sim$ (iii) to achieve a self-consistent solution.

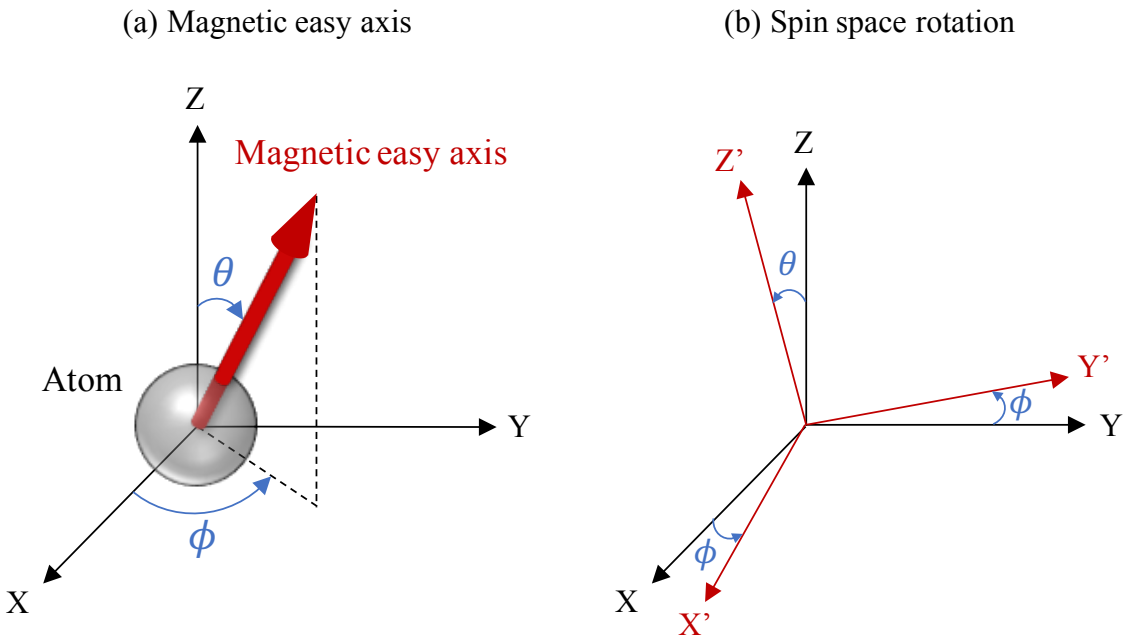

Figure 2.8: (a) Schematic of spin quantization axis where magnetic moment lies along (θ, ϕ)-direction in polar coordination. (b) Cartesian coordination can be rotated by angles of θ and ϕ using rotation matrix U in Eq. (2.145) from XYZ space to $X'Y'Z'$ space.

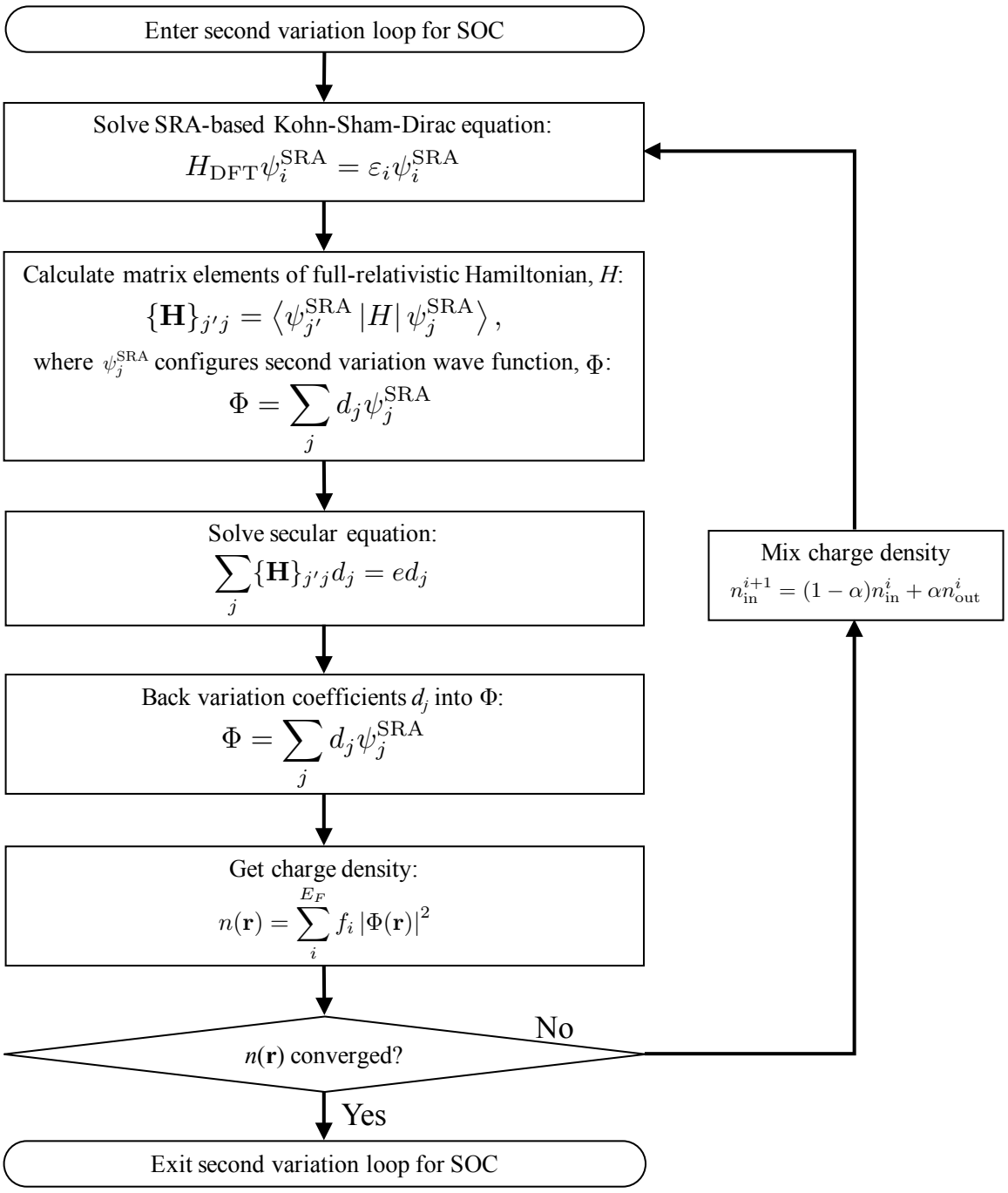

Figure 2.9: Flowchart of the second variation method for treating the SOC within the scalar relativistic approximation.

Chapter 3

Application to transition-metal monoxide, TMO

3.1 Introduction

For the transition-metal monoxides, TMOs, of Mott-type insulators, the DFT calculations within the LDA or GGA arise a problematic issue, for example, unphysical metallic feature in FeO and CoO, and underestimating band gaps even in MnO and NiO showing insulators. It is thus suggested that a proper treatment of correlation effects by the DFT+U that go beyond the LDA and GGA functionals is needed to demonstrate experimentally observed insulating properties. In the last decades, a number of researchers have attempted to derive the U_{eff} for the DFT+U theoretically, but widely scattered values were reported even for the same ionic state as summarized in Table 1.3. However, since the optimal U_{eff} values can extremely depend on the computational details such as potentials, basis sets, and projection operators, comparing the U_{eff} in absolute values may not be of significance.

In this chapter, a relationship between the U_{eff} and basis set have been focused to study. In this context, liner response based U_{eff} calculations were performed for different sizes of MT spheres of the TM ions, R_{MT}. This systematical investigation is inspired by the fact that the implemented LAPW basis set is defined by the size of the MT sphere radius: the coefficients $A_{\ell m}$ and $B_{\ell m}$ in the radial part of the LAPW basis in Eq. (2.40) are determined by boundary conditions of the wave function on the MT sphere of radius R_{MT}. Varying the

R_{MT} may translate a change in the basis set, and more strictly, that of density matrix. Our results find that the U_{eff} values depend strongly on the R_{MT} size in all systems by more than $2 \sim 3$ eV. However, despite this large variation, essentially identical valence band structures are obtained, and we find an approximate scaling of U_{eff} with regard to R_{MT}. Thus, although simple transferability of the U_{eff} value among different calculations methods is not allowed, we propose guidelines for estimating the optimal U_{eff}.

3.2 Calculation model

A model of the rock-salt structure with the rhombohedral lattice vectors, as shown in Fig. 3.1, is employed. The lattice constants are fixed to match to experimentally observed values, 4.435, 4.334, 4.261, and 4.195 Å for MnO, FeO, CoO, and NiO, respectively [143–146], and an antiferromagnetic spin alignment along the [111] direction, called as the AFM II, is assumed. All calculations were carried out by all-electron FLAPW method and the GGA is used for exchange-correlation term. The LAPW basis functions with cutoff of $|\mathbf{k} + \mathbf{G}| \leq 3.9$ a.u.$^{-1}$ are used, and angular momentum expansion inside MT sphere is truncated to $\ell = 8$ (TM) and 6 (O) for the wave functions, charge and spin densities, and potentials. For the oxygen atom, the MT radius sets 1.4 a_B, while that of TM atoms was varied from 2.0 a_B up to touching spheres of nearest neighbor atom, i.e., 2.2, 2.4, 2.5, 2.6, and 2.7 a_B. The k-point mesh of $8 \times 8 \times 8$ in the first Brillouin zone is used.

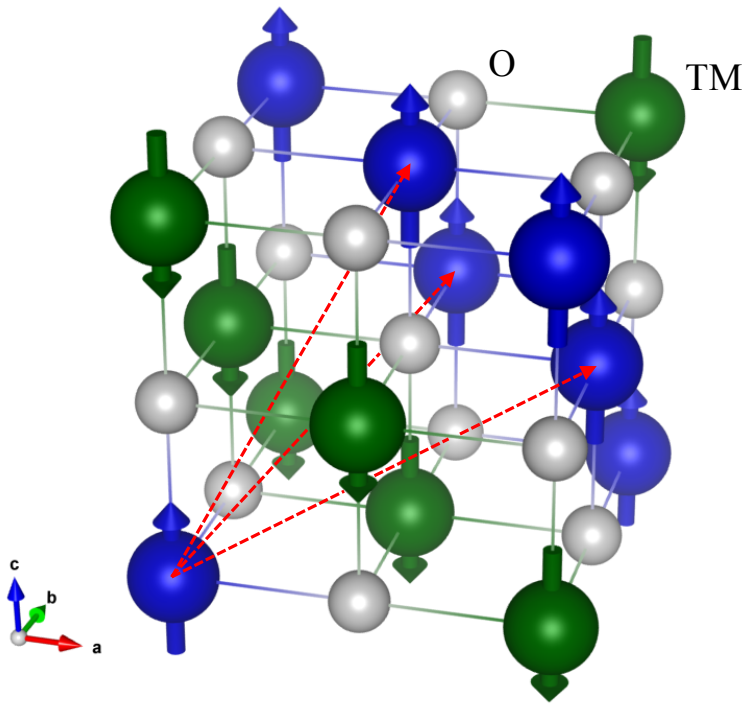

Figure 3.1: Geometric structure of a transition-metal monoxide with an anti-ferromagnetic alignment along [111] direction, AFM II type. Large (blue and green) and small (gray) circles indicate transition metal (TM=Mn, Fe, Co, and Ni), where the arrows at the TM atoms represent magnetic moment directions. Dashed (red) arrows represent the unit vector of a rhombohedral unit cell.

3.3 Calculation of effective on-site Coulomb interactions

We start by considering the effect of the U_{eff} on the band structure. Figure 3.2 shows the calculated bands and partial density of states (DOS) of the $3d$ bands for MnO for two U_{eff} values previously derived (c.f. Table 1.3), 3.6 and 6.04 eV (as well as GGA, $U_{\text{eff}} = 0$), and $R_{MT} = 2.2\ a_B$. In the GGA, there are sharp peaks due to the Mn-$3d$ states around the Fermi energy. Introducing U_{eff} opens the gap and pushes the Mn d states away from the gap. Not surprisingly, the choice of U_{eff} affects both the valence and conduction bands significantly, suggesting an issue of non-transferability of U_{eff} values.

We now proceed to calculate U_{eff}. Figure 3.3 shows the occupation numbers of $3d$ orbitals, n_d, of the TM atoms as a function of applied constraint field, μ for R_{MT} varying from 2.0 to 2.7 a_B. In all the systems, the occupation number increases as R_{MT} increases. When a negative (or positive) constraint field is applied, the occupation number at the constrained TM atoms linearly increases (decreases) relative to the $\mu = 0$ case (left panels in Fig. 3.3). Since the total occupation number in the unit cell is conserved, the occupation numbers at the unconstrained ($\mu = 0$) nearest-neighbor site exhibit the opposite tendency (right panels).

The response functions of Eqs. (2.110) and (2.111), corresponding to the gradient of occupation number n_β with respect to the applied constraint field μ_α at site α, were calculated numerically for each site β, and then U_{eff} was evaluated from Eq. (2.112). Because the KS term does not include self-consistent screening and can be thought of in terms of perturbation theory effect on the occupation numbers, n_d, due to the applied constraint fields, we find that the curves for n_d are parallel to each other for different R_{MT} (see solid line in Fig. 3.3), and thus results in constant χ_{KS}. On the other hand, the interacting χ_{scf} is calculated self-consistently, with the screened response obtained by treating of interactions of electrons, nuclei, and exchange-correlation within GGA level. Since the self-consistent cycle is beyond the framework of linear response, the variation of n_d with regard to μ is consequently affected by the size of the MT sphere differently.

As mentioned above, Eqs. (2.110) and (2.111) require the inverse of the density response matrices, which in turn will depend on the size of the supercells. Figure 3.4 summarizes the behavior of U_{eff} as a function of number of atoms per cell (size of the supercell). For MnO with $R_{MT} = 2.0\ a_B$, for example, U_{eff} has a values of 5.8 eV for a $1 \times 1 \times 1$ supercell (4 atoms per

cell), while for $2 \times 2 \times 2$ (32 atoms) and $3 \times 3 \times 3$ supercells (108 atoms) it is converged to 10.1 eV. For all the systems the converged U_{eff} values decrease when the sphere radius increases. These changes can be quite large, such as in the case of MnO (left top panel in Fig. 3.4) where there is a 3 eV difference in U_{eff} for radii of 2.0 and 2.7 a_B. Similar behavior is seen for FeO and NiO; the results of CoO will be discussed later.

Although the calculated U_{eff} varies significantly with MT radius, the band structures and local 3*d*-DOS are essentially identical as shown in Figs. 3.5, 3.6 and 3.7, but differ significantly from the GGA results. In MnO, the localized d states, whose t_{2g} and e_g orbitals are fully occupied by five electrons in parallel, locate at 4.5 and 5.5 eV below the Fermi energy in the valence states, as shown in Fig. 3.5. Even though the GGA calculations show a metallic character in FeO due to the partially occupied triplet t_{2g} in the minority spin state by one electron resulting in metallic, the calculations using derived U_{eff}s open the band gap over 4 eV. which leads to in the insulator (see Fig.3.6). For the NiO in Fig. 3.7, fully occupied minority t_{2g} state constitutes the Fermi surface in the GGA, but this energy position becomes lower when the +U calculations, then the Fermi states are composed by O-2p states (not shown in figure). For the all systems, that consistently derived values of $U_{\text{eff}}(R_{MT})$ do in fact result in the same band structures and properties argues strongly for the validity of the underlying constraint DFT approach and demonstrates that different (converged) DFT computational methods should agree even when the absolute values of U_{eff} differ greatly. (As already demonstrated in Fig. 3.2, we have confirmed that in all cases using U_{eff} values obtained for one R_{MT} in calculations with a different choice of radius leads to significant changes in the calculated bands.)

Supplementally, we also performed to band structure calculations in which the applied value of U_{eff} is not a determined one for a employed R_{MT} For example, the electronic structures for MnO which are calculated by setting the R_{MT} of 2.7 a_B and the U_{eff} of 7.1 eV, although the derived U_{eff} for 2.7 a_B of MT sphere is indeed 10.1 eV. It is confirmed that obtained ground state bands totally differ from each other: the large peak of d-states are relatively shifted in lower energy, by about 1 eV (this is very big difference), and their dispersions become rather less. This tendency is contradictory to the results shown in Fig. 3.5. Same situation is taken account in other models.

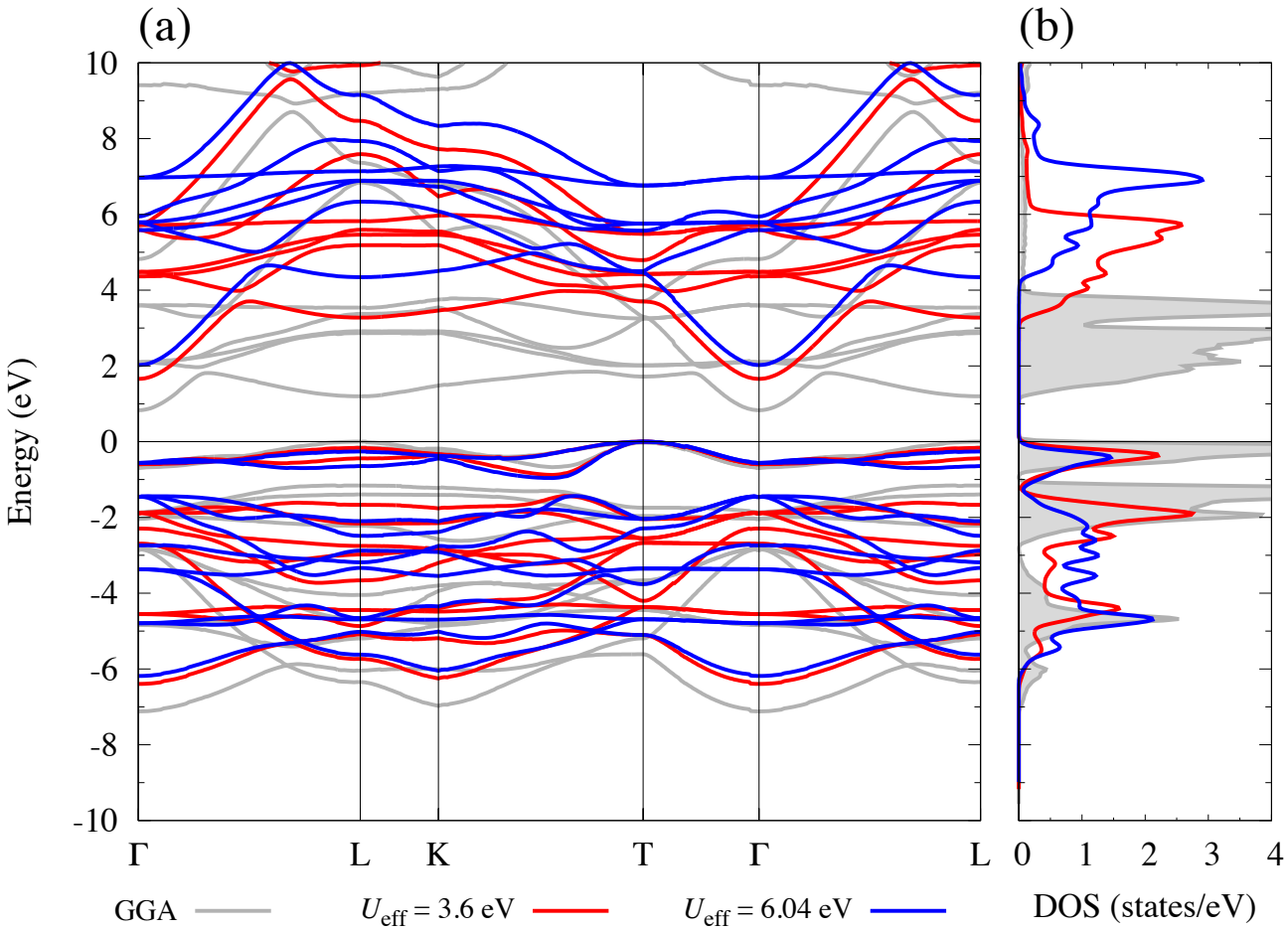

Figure 3.2: (a) Band structures and (b) partial 3d density of states for MnO, where MT sphere size of 2.2 a_B is used for Mn. Red and blue solid lines correspond to the previously reported values of U_{eff}, i.e., 3.6 and 6.0 eV, respectively (see Table 1.3). The GGA calculation (U_{eff}=0 eV) is also shown in gray line in (a) and filled area in (b). The Fermi energy is set to an eigenvalue at valence top states.

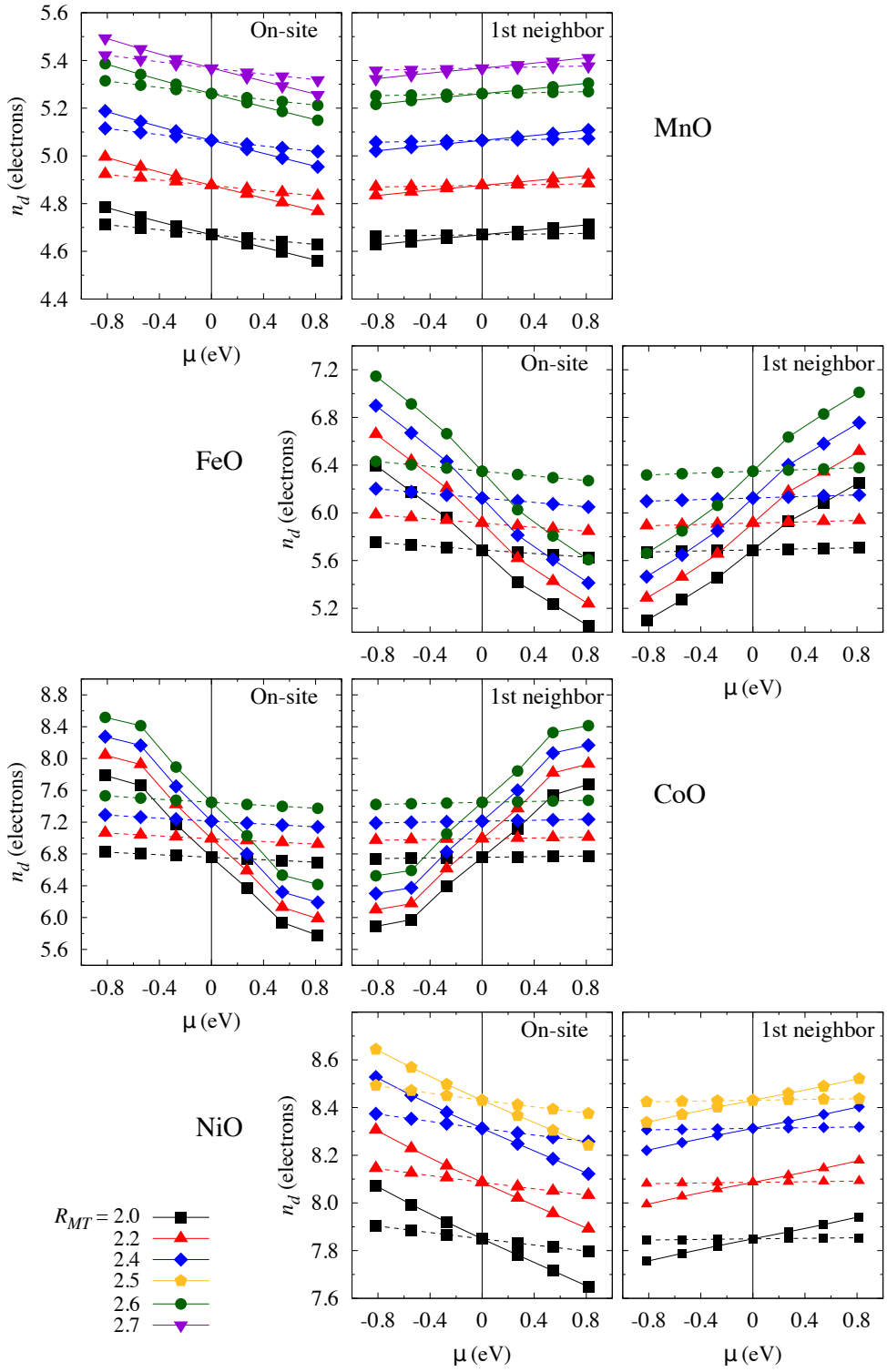

Figure 3.3: Variations of the occupation numbers of $3d$ orbitals, n_d, as a function of constraint field, μ, for (a) MnO, (b) FeO, (c) CoO, and (d) NiO. Left panels for each are at on-site where set of μ is applied to and we are interested in, and right ones are at unconstrained first-neighbor site. Solid and dashed lines indicate behavior of self-consistent (SCF) and Kohn-Sham (KS) calculations, and the symbols: i.e, square (black), triangle (red), diamond (blue), circle (green), and downward triangle (purple), represent the size of MT sphere for TM atoms, respectively.

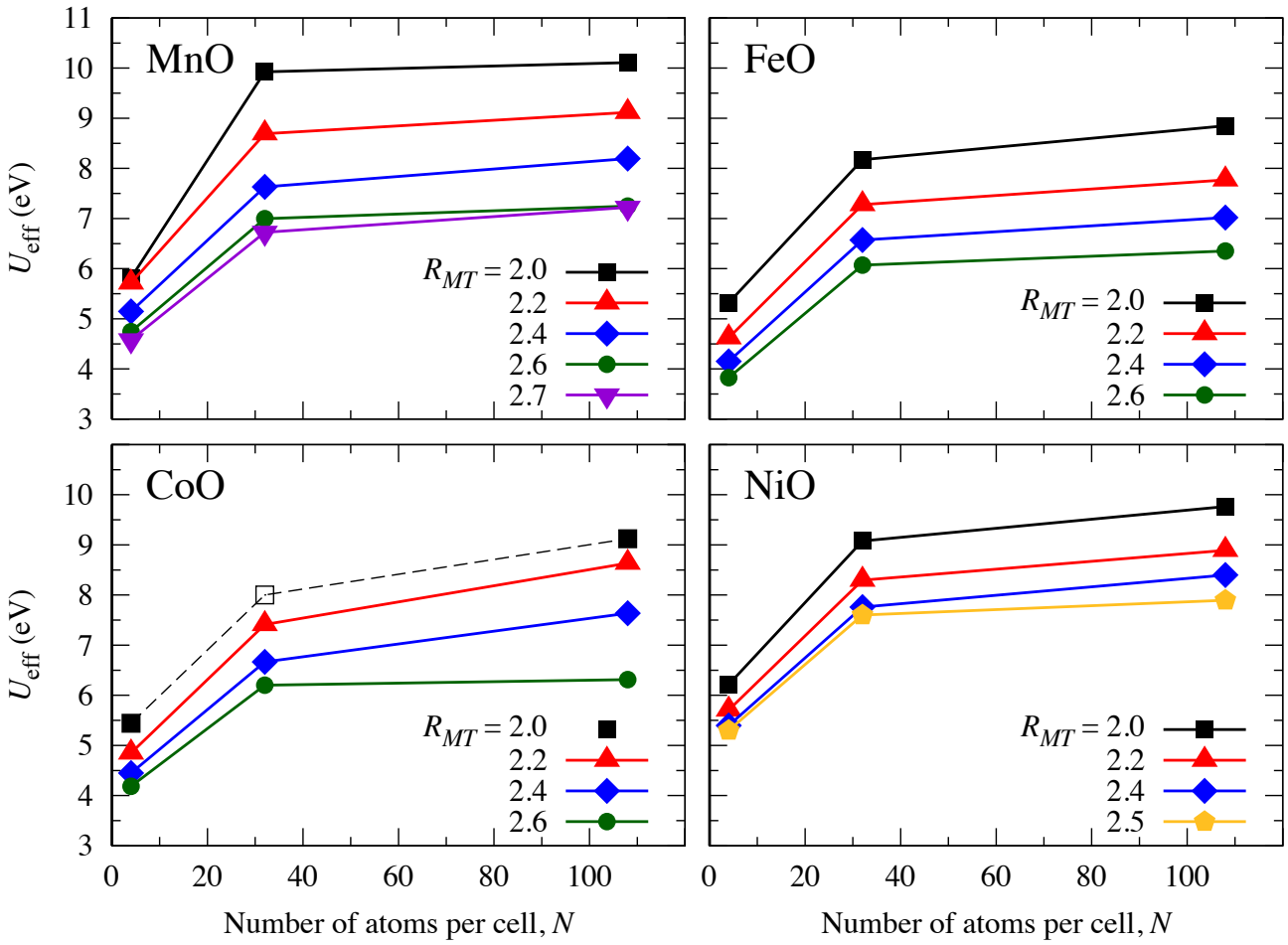

Figure 3.4: Effective on-site Coulomb interaction parameters, U_{eff}s, as a function of number of atoms per cell, N, for (a) MnO, (b) FeO, (c) CoO, and (d) NiO. For (c) CoO system, an opened plot in $R_{MT} = 2.0\ a_B$ is expected value from the tendency of what is observed in the other models (see in text for more detail). Notation is the same as in Fig. 3.3.

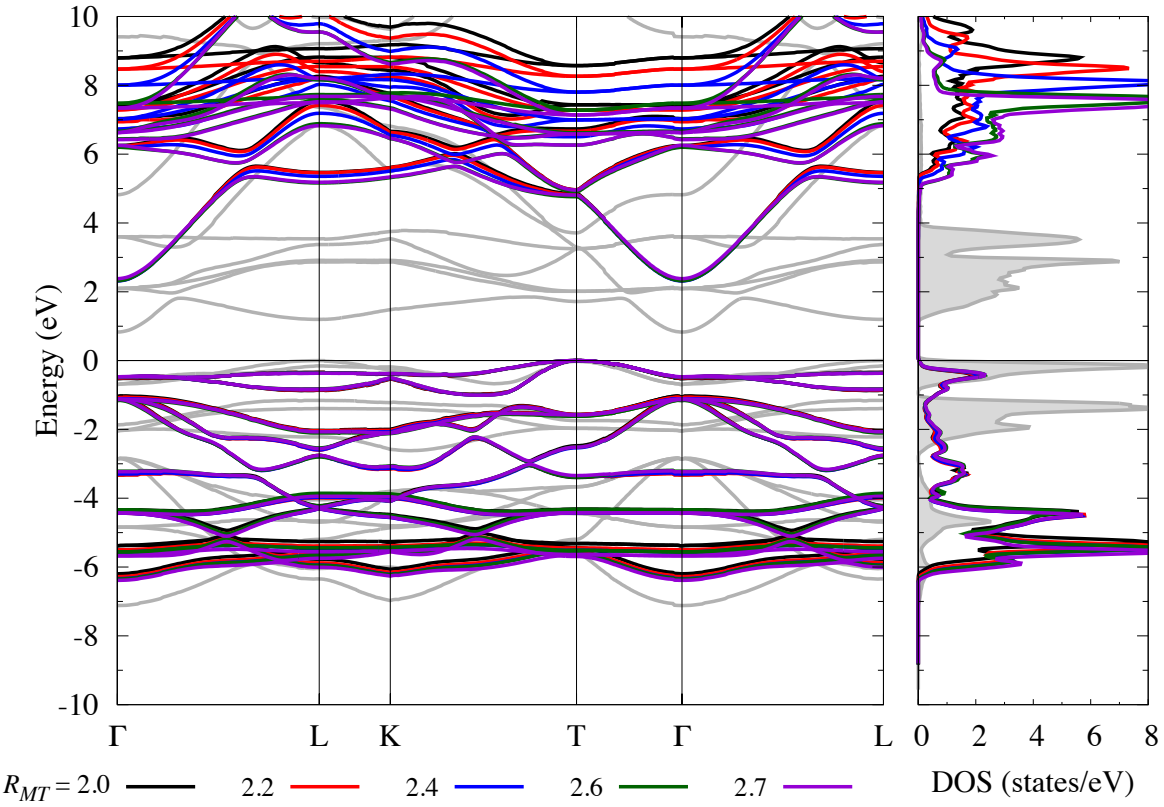

Figure 3.5: GGA+U band structures and partial 3*d* densities of states for different TM sphere radii using the scaled U_{eff} values for MnO. Black, red, blue, green, and purple solid lines are R_{MT} of 2.0, 2.2, 2.4, 2.6, and 2.7 a_B for Mn atom, respectively. The GGA ($U_{\text{eff}} = 0$ eV) calculations are also shown in gray line (left panel) and filled space (right). The energy zero is set to the top of the valence band.

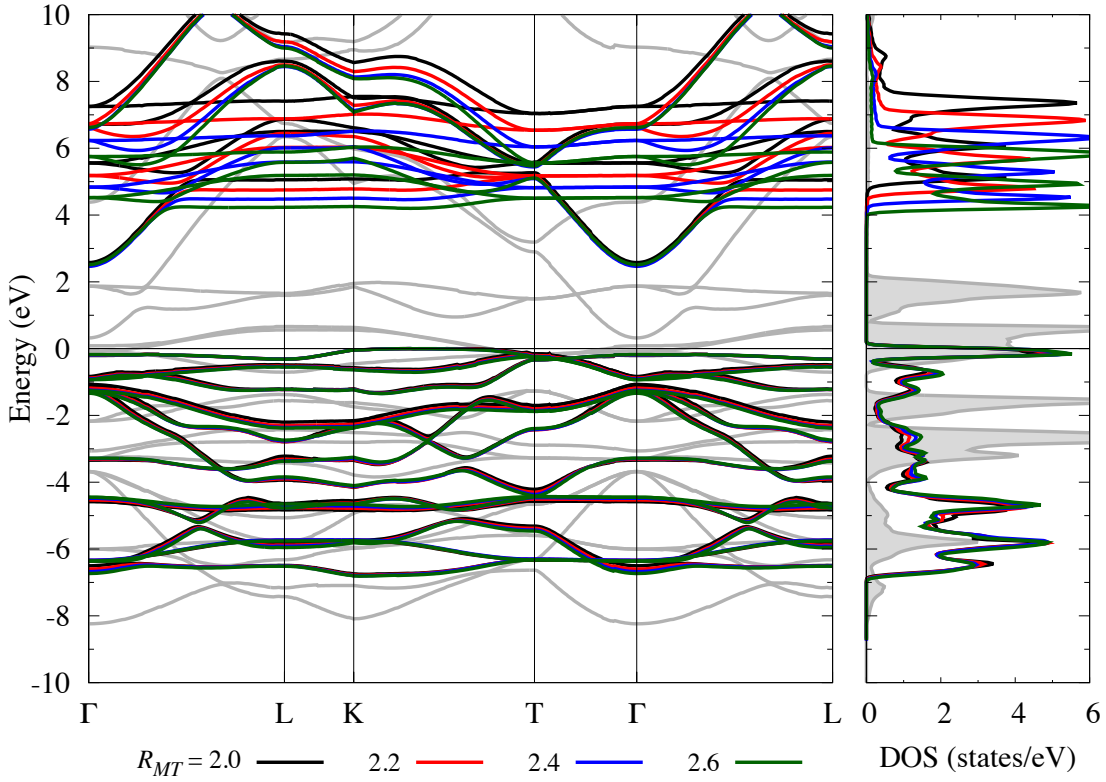

Figure 3.6: GGA+U band structures and partial 3d densities of states for different TM sphere radii using the scaled U_{eff} values for FeO. Black, red, blue, and green solid lines are R_{MT} of 2.0, 2.2, 2.4, and 2.6 a_B for Fe atom, respectively. The gray shows GGA calculations as same manner in Fig. 3.5.

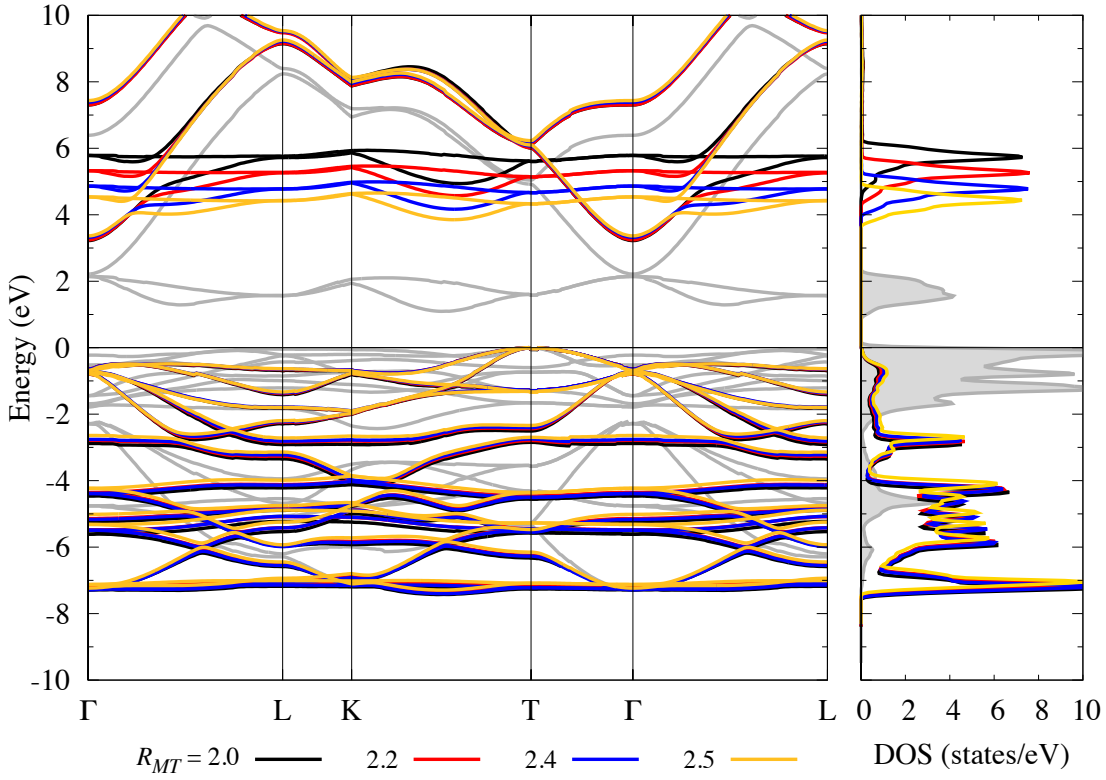

Figure 3.7: GGA+U band structures and partial 3d densities of states for different TM sphere radii using the scaled U_{eff} values for NiO. Black, red, blue, and green solid lines are R_{MT} of 2.0, 2.2, 2.4, and 2.5 a_B for Ni atom, respectively. The gray shows GGA calculations as same manner in Fig. 3.5.

3.4 Electronic structure

Based on our results, we propose guidelines to estimate suitably scaled values of U_{eff} for different MT sphere size, which will also be applicable to other computational methods. Figure 3.8 shows the determined $U_{\text{eff}}(R_{MT})$ as a function of occupation number, $n_d(R_{MT})$ determined in the standard $U = 0$ GGA calculations. We find a simple linear relationship between U_{eff} and n_d: U_{eff} is negatively proportional to increasing n_d as shown by the regression lines in the figure. We have confirmed for a number of cases that using U_{eff} values estimated from the calculated d-electron occupation number at the GGA level produces the same band structure and gives the same physics.

Of the different TMOs considered, CoO presents some particular issues which we now discuss. In Fig. 3.4, we were unable to obtain a value for the $R_{MT} = 2.0\ a_B$ $2 \times 2 \times 2$ (32 atom) supercell because our calculations did not yield a stationary solution for this antiferromagnetic alignment. However, an appropriate value could be obtained from the scaling behavior and is represented by the opened square and dashed line in Fig. 3.4. Rather unexpectedly, the behavior for $R_{MT} = 2.6\ a_B$ with regard to cell size differs from the others and has a value of $U_{\text{eff}} = 6.3$ eV. This value is smaller than expected from other trends, and in fact leads to a calculated band structure that differs from the others, the green line in left bottom panel of Fig. 3.3, which shows a shift of the $3d$ states. Similarly, in Fig. 3.8, only the $R_{MT} = 2.6\ a_B$ point is off the regression line for CoO. Analysis of the calculations suggest that this observed behavior for this case is due to numerical issues related to the fact that for this R_{MT}, the Co and O spheres are almost touching ($\sim 0.026\ a_B$); increasing various cutoffs should correct this problem. (Since as a practical matter touching spheres in FLAPW calculations is *not* good practice, this problem generally will not arise.) However, if we simply use the scaled value as indicated by the open square in Fig. 3.8 appropriate for $R_{MT} = 2.6\ a_B$ of 7.0 eV, the valence band structure (not shown) is identical to those for the other values of $U_{\text{eff}}(R_{MT})$.

Although the valence band structures for different values of $U_{\text{eff}}(R_{MT})$ are essentially the same, there are differences in the conduction bands (Figs. 3.5, 3.6, 3.7 and 3.9). Using MnO as an example, we finally provide a possible argue to this problem that is related to a nature of anti-bonding wave function. The Mn $3d$ states just below the Fermi energy hybridize with O-$2p$ orbitals in the GGA calculation (Fig. 3.10 (a)). In contrast, for GGA+U, the O-$2p$ pre-

dominates at the Fermi level (Fig. 3.10 (b)). Figure 3.11 shows a schematic energy diagram of the hybridization between Mn and O in the GGA and GGA+U calculations. For the majority valence (occupied) states, the introduction of the $+U$ correction pushes the Mn-3d orbitals down to lower energy relative to the O-2p, hybridizing to form bonding orbitals, rather than antibonding states in GGA calculation. Both with and without $+U$, antibonding states are formed by Mn-3d states in the minority conduction (unoccupied) bands. The wave functions of the antibonding state, which possesses a node, are more compact spatially (Fig. 3.12 (b)) compared to those of bonding states (Fig. 3.12 (a)). Figure 3.13 shows calculated radial probability of the wave function for the different TM atoms (TM = Mn, Fe, Co, and Ni) as a function of radial. Since the radial wave function for the latter TM atoms in the periodic table is rather more localized, the Ni (or Mn) has few (more) radial probability at the tail, resulting in small (large) change in the charge density when the MT sphere size increased. Thus, the weight of an antibonding states varies slower with respect to sphere size than that of the bonding states, as shown in Fig. 3.12 (c); this is one reason behind the decrease in magnitude of the observed slopes (coefficient a of $U_{\text{eff}} = an_d + b$) in Fig. 3.8 going from Mn to Ni. A consequence is that for the conduction bands, changing R_{MT} does not appreciably change the d wave function weight that U is acting on, so these size of the matrix elements determined by mainly by the value of U_{eff} alone. As a result, as found in all the systems considered, the conduction bands are shifted toward lower states in energy as R_{MT} increases and U_{eff} decreases as shown in Figs. 3.5, 3.6, 3.7 and 3.9.

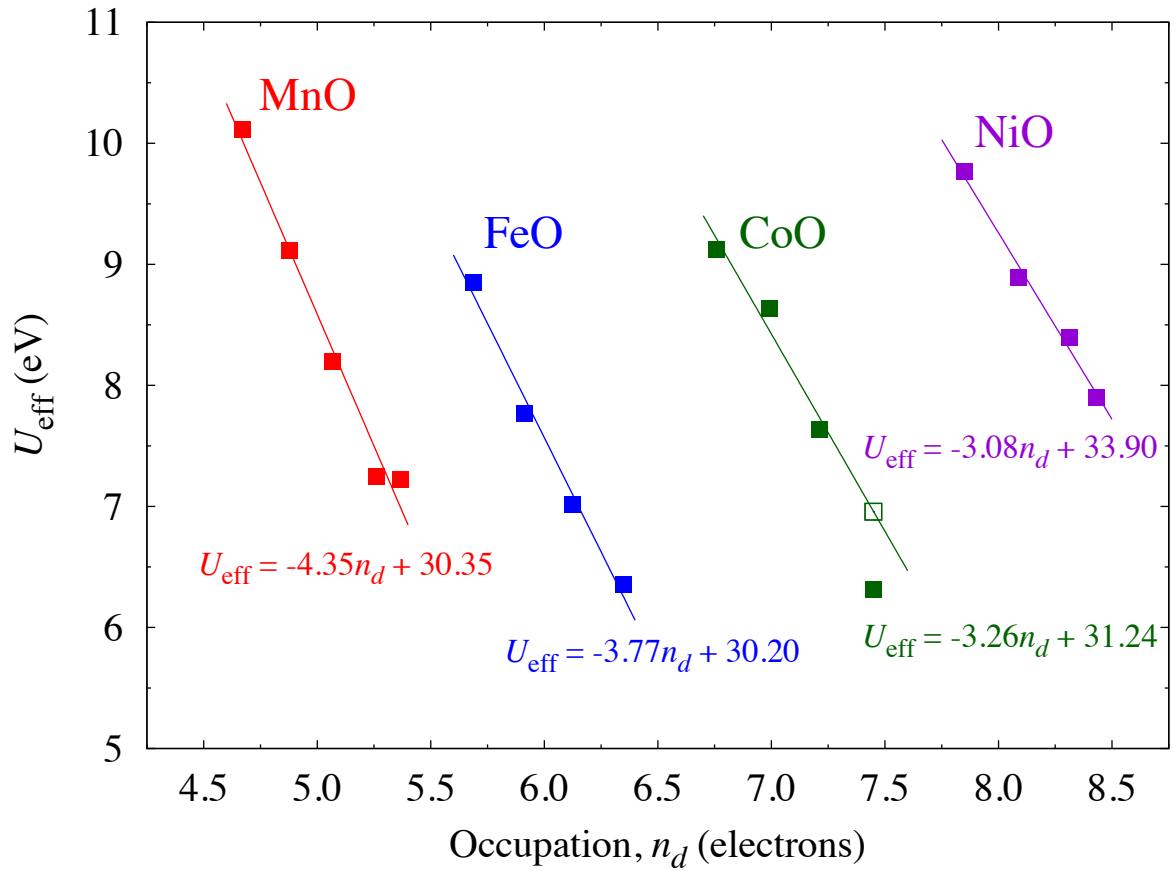

Figure 3.8: Relationship between determined U_{eff} values and occupation numbers, n_ds, that are calculated within framework of GGA. Colored plots in red, blue, green, and purple are for MnO, FeO, CoO, and NiO, respectively. Regression lines are also shown by solid lines. In the CoO system, the regression line is fitted by using from smaller n_d values up to the third one, that correspond to R_{MT} of 2.0, 2.2, and 2.4 bohr.

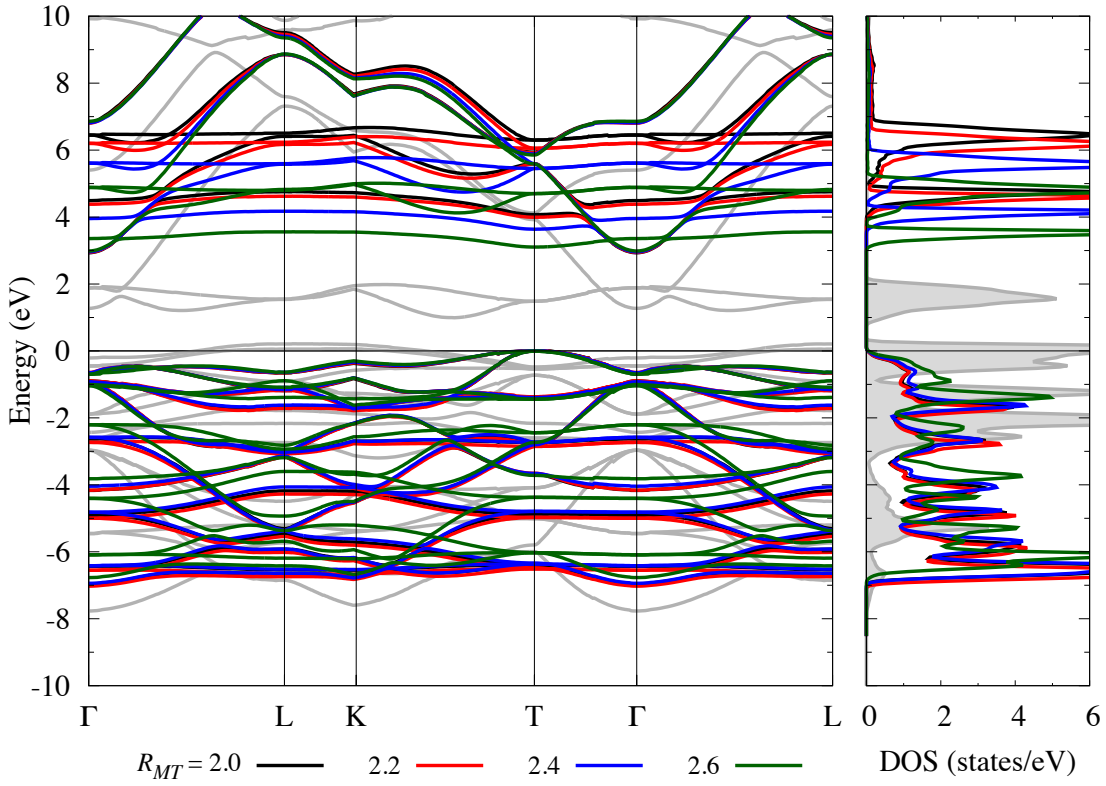

Figure 3.9: GGA+U band structures and partial 3d densities of states for different TM sphere radii using the scaled U_{eff} values for CoO. Different solid colors are same as in Fig. 3.6. The gray shows GGA calculations as same manner in Fig. 3.5.

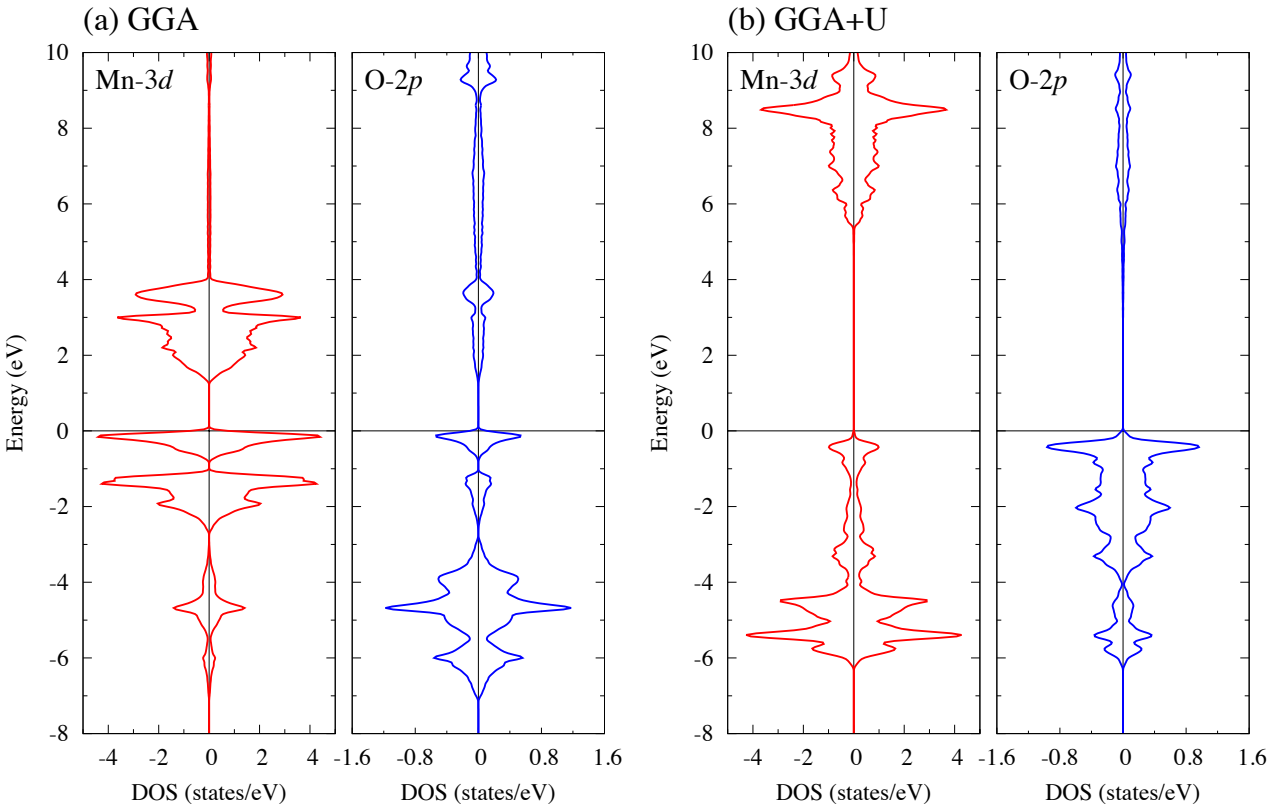

Figure 3.10: Calculated DOS for MnO by (a) GGA and (b) GGA+U when R_{MT} of Mn atom is 2.2 bohr. Left panel shows Mn–3d orbital, where splits into e_g (red) and t_{2g} (blue) states in octahedral crystal field symmetry, and right one shows O–2p states. The Fermi energy is set to valence top eigenstate.

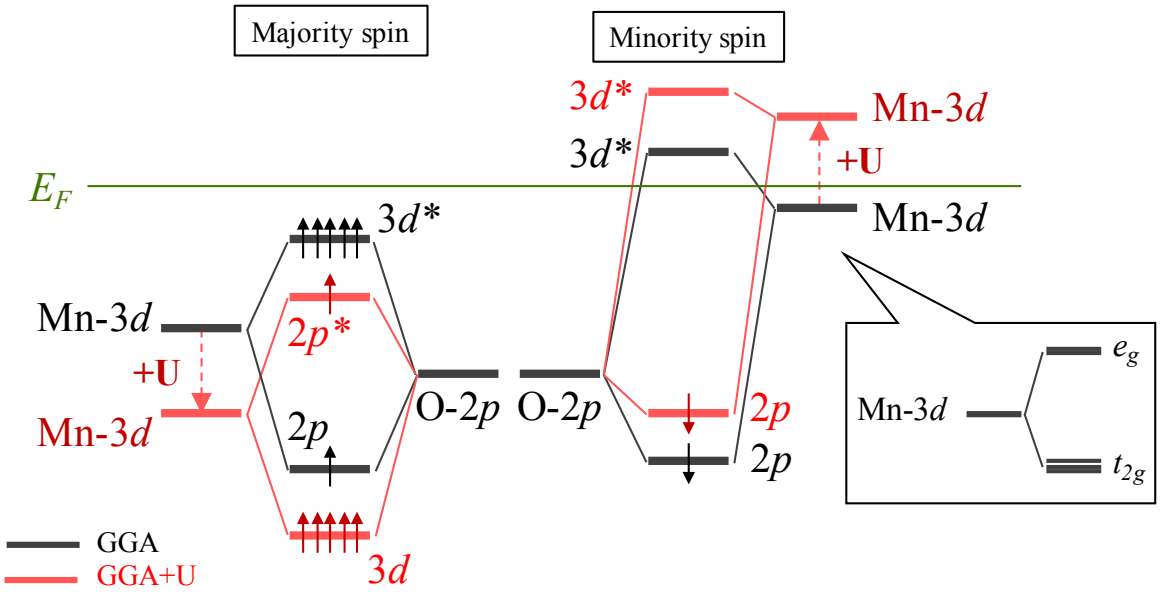

Figure 3.11: Energy diagram of hybridization between Mn–3d and O–2p in both GGA (black) and GGA+U (red) calculations, where correspond to DOS of Fig. 3.10 (a) and (b), respectively. Left (right) panel shows majority (minority) spin state and solid arrows indicate occupied electrons with either up or down spin below Fermi energy (green solid line). Note that the split e_g and t_{2g} orbitals are simplified by only one solid line as a Mn–3d orbital.

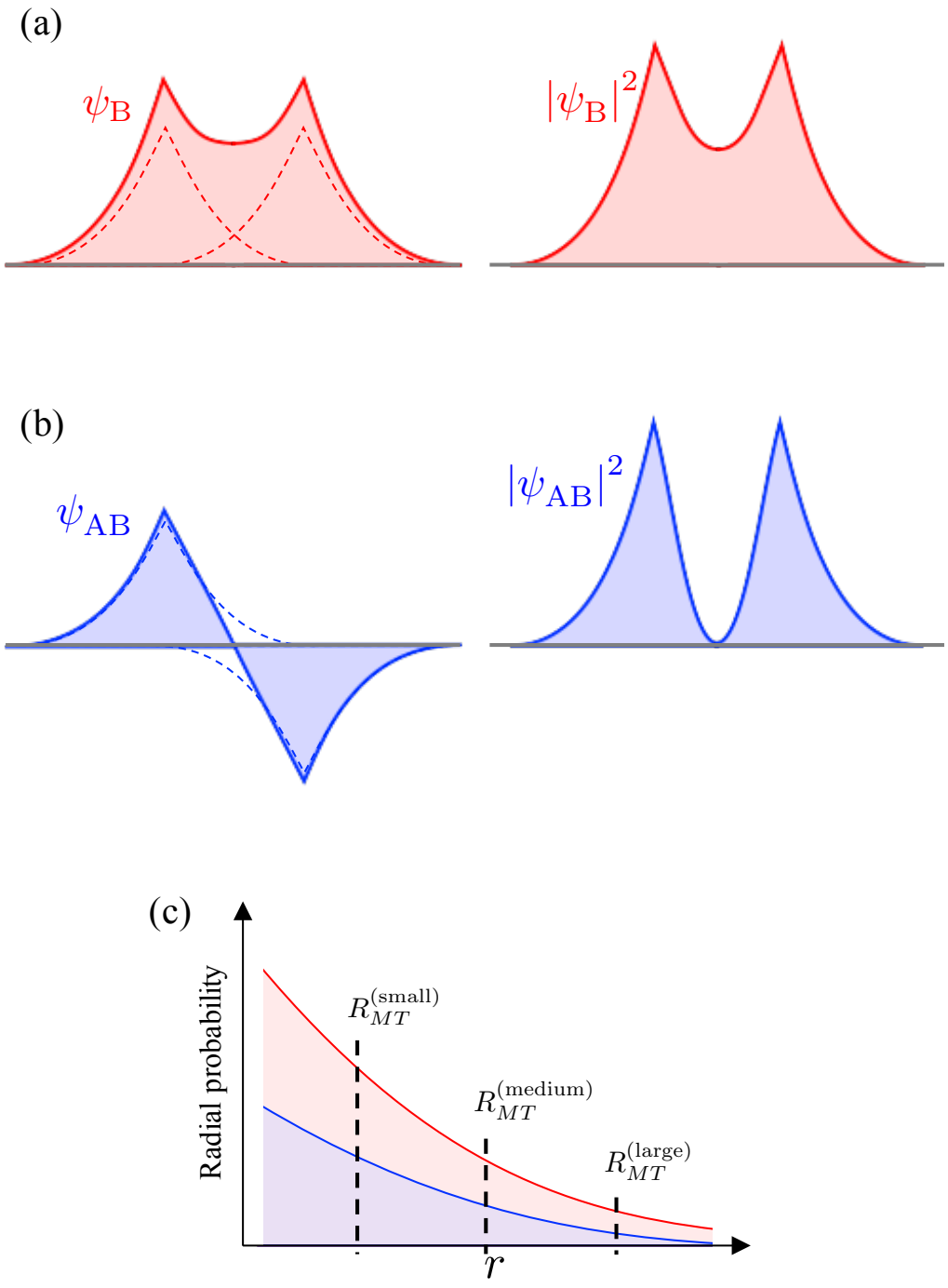

Figure 3.12: Schematics of spatially spread wave functions (left side) and their charge densities (right) for (a) bonding state, ψ_{B}, and (b) anti-bonding state, ψ_{AB}. (c) Comparison of norm of bonding- and anti-bonding wave functions as as a function of radial, r. Red and blue are bonding and anti-bonding states, respectively. $R_{MT}^{(\mathrm{small})}$, $R_{MT}^{(\mathrm{medium})}$, and $R_{MT}^{(\mathrm{large})}$ indicate examples of small, medium, and large MT sphere radii.

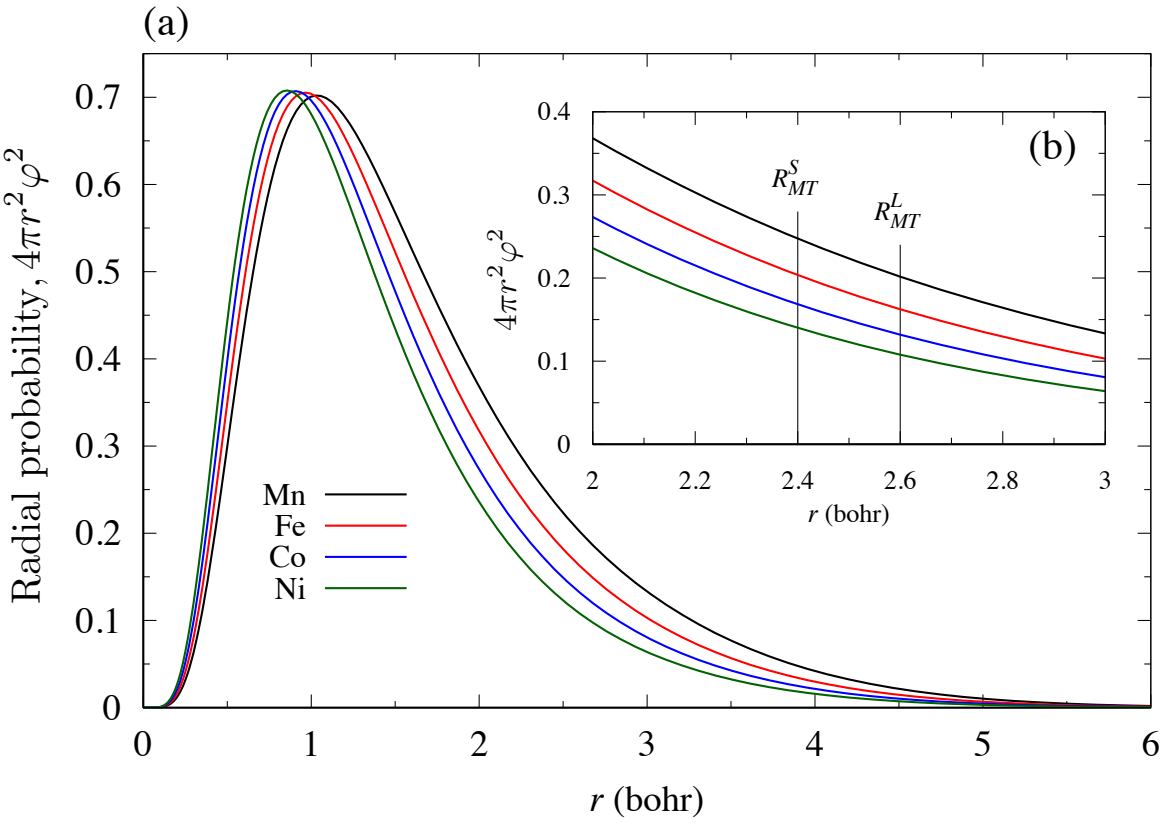

Figure 3.13: (a) Radial probability for d-orbital, $4\pi r^2\varphi^2$, as a function of radial, r. Black, red, blue, and green lines are for free-Mn, Fe, Co, and Ni atoms, respectively. (b) Inset focuses on the region where is usually employed as radius of their MT spheres. In (b), $R^{\mathrm{S(L)}}_{MT}$ is a smaller (larger) values as an example of MT sphere size (see text for more detail).

3.5 Concluding remarks

The on-site Coulomb effective U_{eff} is determined by all-electron FLAPW method based on constraint DFT approach from linear response approach for varying radius of MT sphere in prototypical correlated monoxides, TMO (TM = Mn, Fe, Co, and Ni). Although the significant dependence of U_{eff} value on the R_{MT} size were confirmed, importantly, an identical valence band structure was produced in all systems with an approximate scaling of U_{eff}. Furthermore, a simple linear relationship between the determined U_{eff} and the n_d calculated by the standard GGA is found and a straightforward estimation of the U_{eff} from the linear relationship was demonstrated where the electronic structure was identical. Our results implies that a simple transferability of the U_{eff} values among different calculation methods is not allowed, but the relationship associating scale of the U_{eff} with occupations n_d (or MT sphere size R_{MT}) gives a guideline for the most suitable parameter.

Chapter 4

Application to organometallic metallocene molecule, $TMCp_2$

4.1 Introduction

Since the rectifier elements and transistors that are composed by organic molecules had been predicted by Aviram *et al.* in 1974 [147], there has been a growing interest in studies and developments of novel applications because of their advantages compared to that in the Si-based devices, for example, size minimization, light weight, mechanical flexibility, and long-time spin relaxation/lifetime [148–153], in which an effort now extends to treat an extreme limit of a single molecule [154]. In organometallic molecules composed of metal elements such as transition metals and rare-earth metals, there is two freedoms of spins and electron charges, which can be controlled on experimental level as demonstrated by spin-polarization scanning tunneling microscopy (SP-STM) and atomic force microscopy (AFM) experimentally. [155–159] Metallocene ($TMCp_2$) discovered in 1950's [160–163] is one of the attractive molecules with a variety of electronic and magnetic properties that can be tuned by substitutions of the composed transition-metals, redox cycles and so on. [164, 165] Further examples: metallocene molecular wire [166] and magnetoresistive element [165], are shown in Fig. 4.1.

For organometallic molecules where the electronic configurations of d (f) electrons are an essential aspect, the complexity of the orbital degeneracy and the changes due to the presence of the ligand field of molecules complicate the theoretical analysis of even the ground state,

with the consequence that *ab-initio* calculations based on the DFT often fail to obtain the experimentally observed ground state electronic configuration. To get straight to the point, this difficulty is intrinsically related to the fact that the various electronic configurations belonging to different irreducible representations are all compatible with the symmetry of the charge (and spin) density (completely symmetric representation), i.e., the *symmetry* of the charge density is not sufficient to distinguish among the electronic configurations.

The d-orbital electronic configurations (or multiplet structures) are given by group theory that identifies symmetries of orbital (wave function) and are described using irreducible representation (term symbol) as

$$^{2S+1}L_J. \tag{4.1}$$

Two kinds of multiplicities are indicated: $(2S+1)$ multiplicity for spin freedom with total spin angular momentum, $S = \sum_i^N s_i$, and $(2L+1)$ multiplicity for orbital freedom with total orbital angular momentum, $L = \sum_i^N \ell_i$, in N-electron system. J is total angular momentum and its multiplicity is shown by $J = L+S, L+S-1, \cdots, |L-S|$. There are patterns of $(2L+1)$ times $(2S+1)$ multiplicities for N-electron system in free atom or ion totally. One can predict the ground state electronic configuration from $(2L+1)(2S+1)$ candidates from the Hund's rule in which the S and L of the open shell follow three rules:

1. For a given electronic configuration, the term with maximum spin multiplicity S has the lowest energy.

2. For a given multiplicity, the term with the largest orbital multiplicity L has the lower energy.

3. For a given term, in an atom, if outermost subshell is half-filled or less than half-filled, the term with the lowest value of the J lies lowest in energy, and if outermost subshell is more than half-filled, the term with the highest value of J lies lowest in energy.

According to these rules, for example, electronic configurations of d^2 system in free atom whose candidates are ${}_{10}C_2$ patterns are shown from the term in lower energy level in Fig. 4.2 (a).

In the metal complex systems, where the symmetry of environment surrounding d-orbital is reduced by ligand fields, the many-body eigenstates of electronic configurations are described

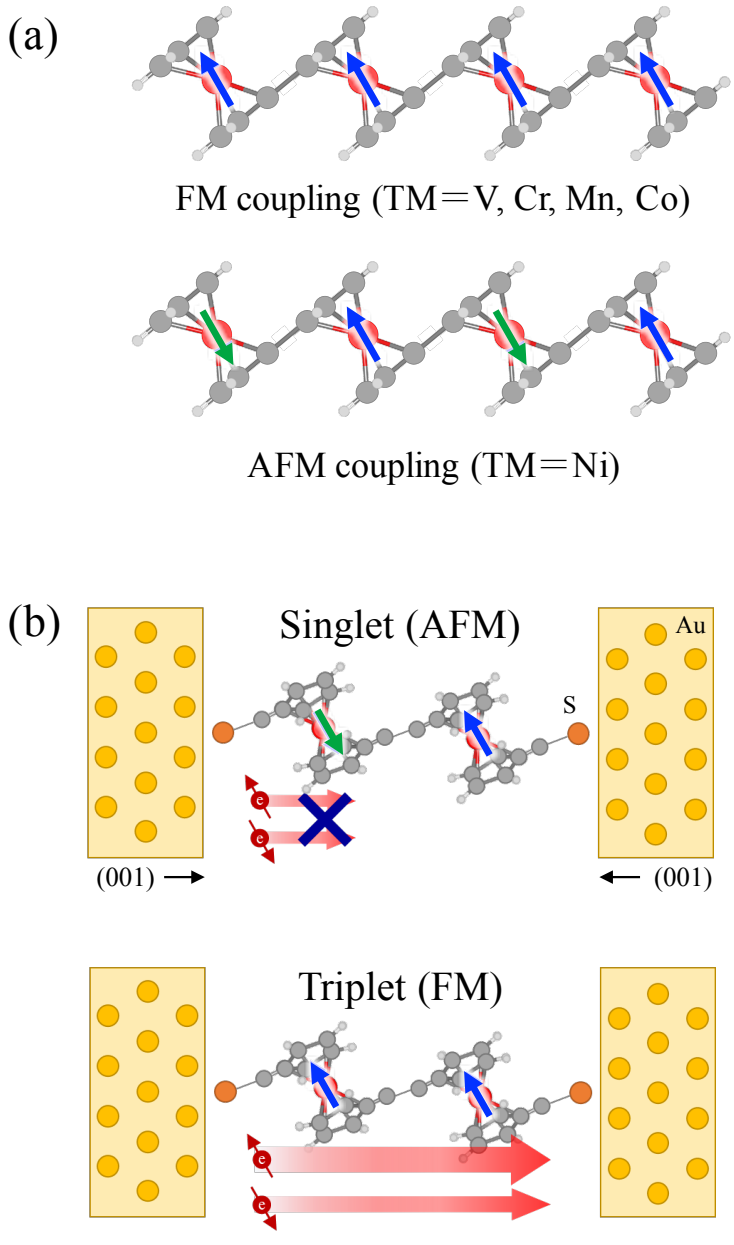

Figure 4.1: (a) One-dimensional molecular wire consisting of metallocenes. Local magnetic moments in respective molecules are interacted to neighboring ones like ferromagnetic (FM) or anti-ferromagnetic (AFM) coupling as shown in upper or lower panels, respectively. (b) Magnetoresistive element which is composed by two metallocene molecules connecting Au(001) surfaces. Resistance becomes higher when local magnetic moment coupling is AFM-like, while it becomes lower when magnetic moments coupling is FM-like. Blue and green arrows indicate local magnetic moment orienting different directions. Circles in different colors corresponding to red, gray, white, orange, and yellow indicate Transition-metal, C, H, S, and Au atoms, respectively.

using irreducible representation within corresponding space group,

$$^{2S+1}\Gamma. \tag{4.2}$$

This is similar to the one in free atom or ion system that are under spherical symmetry, but only difference is the orbtal function L in Eq. (4.1) is replaced by whole of eigenstates Γ.

Figure 4.2 (b) shows the d-orbital splitting due to the ligand field with the irreducible representation in O_h symmetry. The d-orbital of has five-folds degeneracy in free atom split out into two states that correspond to doublet degenerate e_g $(d_{x^2-y^2}, d_{z^2})$ orbital and triplet t_{2g} (d_{xy}, d_{xz}, d_{yz}) orbital. Furthermore, if a metal atom is surrounded by D_{5d} symmetry, complexity of splitting arises and d-orbital is separated into three states: a singlet of a_{1g} (d_{z^2}) and doublets of e_{2g} $(d_{x^2-y^2}, d_{xy})$ and e_{1g} (d_{xz}, d_{yz}).

For Kohn-Sham-based DFT calculations, in principle, the variational principle finds a global minimum of the total energy from arbitrary set of initial charge density in the effective potential by self-consistent-field procedures (see Fig. 4.3 (a)). However, in numerical strategy, an critical issue may be appeared. Organometallic molecules have various meta-stable structure of different electronic configurations at nearly degenerate with ground state energetically. This fact means that the total energies of ground state is competitive with that of meta-stable ones, thus the final SCF-calculated solution must depend on how initial charge density is set numerically. Figure 4.3 (b) shows schematics of competitive total energies as a function of electronic configuration. If noe put initial charge distribution on the parabola function whose minimum is configuration B so that variational principle procedure satisfies that total energy becomes lower and lower by every SCF-iteration. As a result, calculations may be trapped in one of the multiple local minima corresponding to the various electronic configurations. Thus, searching from the ground state electronic configuration of correlated system using DFT remains a significant challenge as well as the importance of correlation effects.

In order to overcome such difficulties, constraint DFT provides a powerful tool for exploring the low energy electronic configurations compatible with a given ligand symmetry. In this chapter, the constraint DFT was applied to the prototypical organometallic molecules, $TMCp_2$, [160–163, 167] for the $3d$ transition metals (TM) from V to Ni. Here it was demonstrated that this approach – combined with non-empirical values of U – is capable of obtaining agreement

with experiments for the correlated organometallic molecules with their high degree of electronic complexity.

Before going to sections of calculated results, previous studies are overviewed. In the past decades, numerous studies have been done for analyzing ground state electronic configurations experimentally. [168–171] Photoelectron spectroscopy measurements of $FeCp_2$ in the gas phase reveal a S=1 spin multiplet corresponding to orbital occupations of the $^1A_{1g}$ state ($d^2_{z^2}, d^4_{x^2-y^2,xy}$). [168, 169] For VCp_2, $CrCp_2$, $MnCp_2$, $CoCp_2$, and $NiCp_2$ in gas phases, $^4A_{2g}$ ($d^1_{z^2}, d^2_{x^2-y^2,xy}$), $^3E_{2g}$ ($d^1_{z^2}, d^3_{x^2-y^2,xy}$), $^6A_{1g}$ ($d^1_{z^2}, d^2_{x^2-y^2,xy}, d^2_{xz,yz}$), $^2E_{1g}$ ($d^2_{z^2}, d^4_{x^2-y^2,xy}, d^1_{xz,yz}$) and $^3A_{2g}$ ($d^2_{z^2}, d^4_{x^2-y^2,xy}, d^2_{xz,yz}$) were systematically observed, [168, 169] where the spin multiplicity S decreases from VCp_2 ($S = 4$) to $FeCp_2$ (1), except for $MnCp_2$ (6), and then it increases in $CoCp_2$ (2) and $NiCp_2$ (3). A high spin state $^6A_{1g}$ of $MnCp_2$ was further identified by electron spectroscopy and nuclear magnetic resonance measurements. [170, 171] However, the DFT ground states are still a matter of debate due to the complexity and difficulty of incorporating correlation effects. For example, for $MnCp_2$, +U calculations predict the low-spin $2E_{2g}$ state [172] while hybrid functional B3LYP calculations predict the high-spin $^6A_{1g}$ state. [173] Further, both calculations for $CrCp_2$ ($^3A_{1g}$) disagree with the ($^3E_{2g}$) state found by experiment.

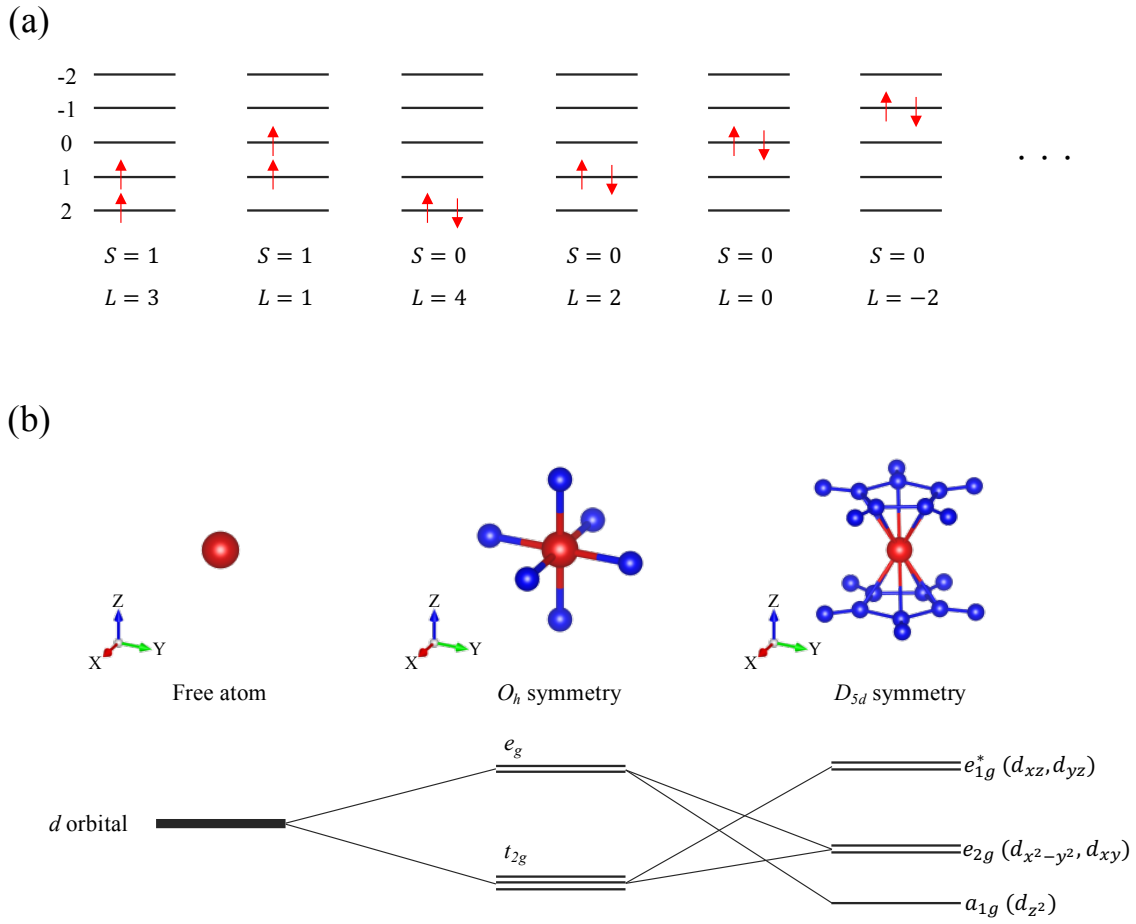

Figure 4.2: (a) Examples of the electronic configurations for free atom with d^2 electron system in which there are ${}_{10}\mathrm{C}_2$ patterns. Candidates are listed in order of lower energy by satisfying Hund's rule. Red arrows indicate the electrons with spin channel and the S and L are total spin and orbital angular momenta. (b) d-orbital splitting due to the ligand field of O_h symmetry, where five-fold degenerate d orbital split out into doublet e_g and triplet t_{2g} orbitals. Further orbital splitting into $e^*_{1g}(d_{xz,yz})$, $e_{2g}(d_{x^2-y^2,xy})$, and $a_{1g}(d_{z^2})$ is occurred due to a ligand field of D_{5d} symmetry. Red and blue circles indicate transition-metal atom and atoms of ligand field, respectively.

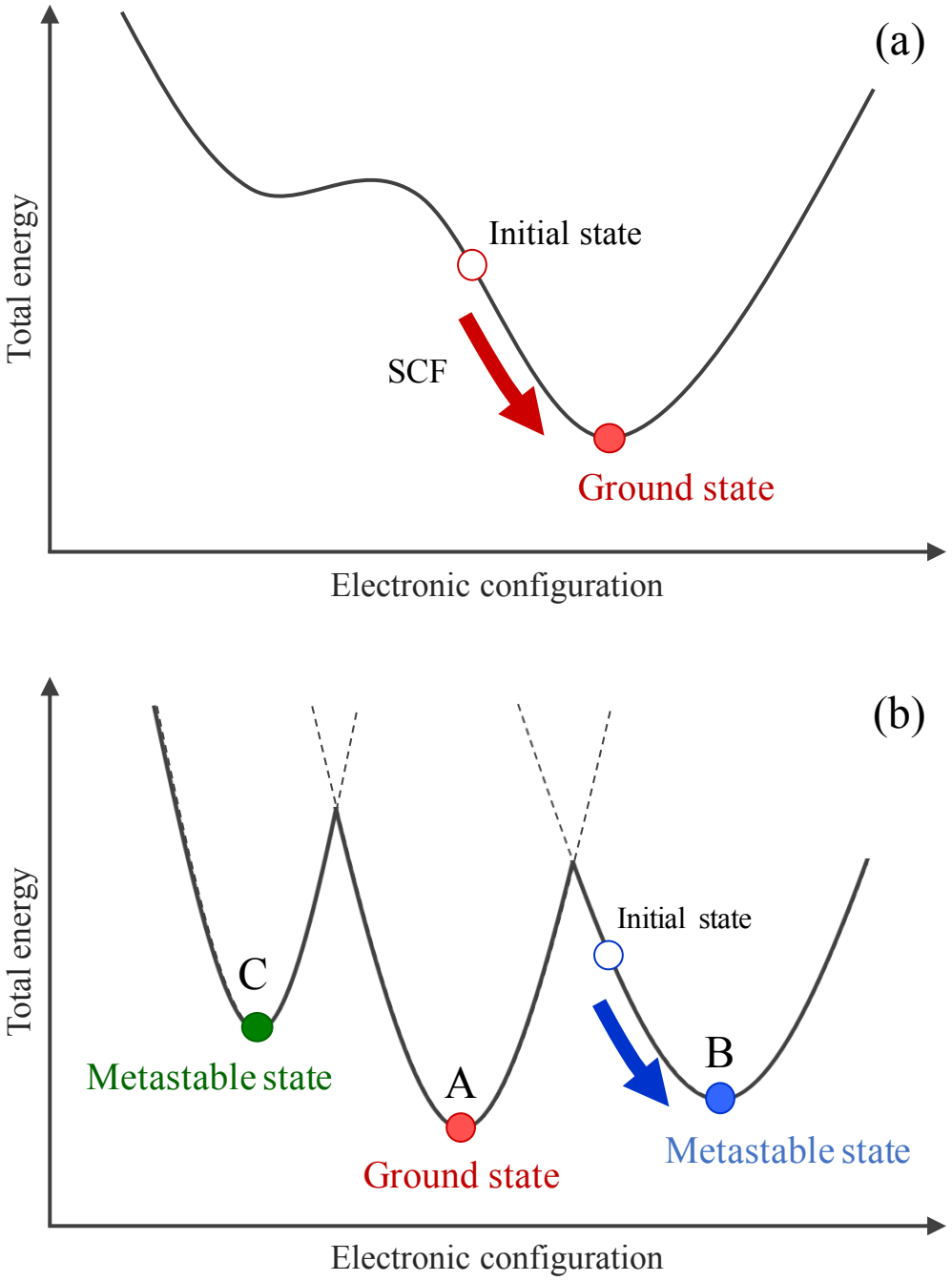

Figure 4.3: (a) Profile of total energy as a function of electronic configuration in Kohn-Sham-based DFT. A given initial state of charge density represented by opened circles, in principle, will lead to ground state (global minimum) represented by closed circle by self-consistent-field (SCF) procedure. (b) Profile of total energy for organometallic molecule systems, in which plural local minima are energetically degenerate.

4.2 Calculation model and molecular orbital

The atomic structure of the $TMCp_2$ molecules, with the two 5-fold cyclopentadienyl rings, Cp_2, is shown in Fig. 4.4. Both eclipsed and staggered conformations exist; here we focus on the latter, which has been the reported structure in a number of experiments. [168–171] The metal atom, at the center of the molecule between the two Cp rings, sits at a site of D_{5d} symmetry such that the d orbitals are split into three states. Figure 4.5 (a) gives a schematic energy level diagram allowed by group theory in the D_{5d} point group: a singlet d_{z^2} and two doublets $d_{xz,yz}$, $d_{x^2-y^2,xy}$. The $d_{xz,yz}$ state may be further pushed up in energy due to the hybridization with the Cp_2 e_{1g} orbital, while the $d_{x^2-y^2,xy}$ state goes down due to the hybridization with the e_{2g} orbital, as illustrated in Figs. 4.5 (b) and (c), respectively. The d_{z^2} state shown in Fig. 4.5 (d), with no direct overlap to the molecular orbitals, may have the lowest energy of the d states.

To model the isolated $TMCp_2$, a slab with infinite vacuum on both side of the slab (along the Cp ring plane normal) far from 2.7 bohr was adopted, with a large in-plane lattice constant of 18 bohr, as shown in Fig. 4.6. For molecular structure, the geometric positions given in Fig. 4.7 and parameters in Table 4.1 are initially used so that the C and H atoms form their own equilateral pentagons with the TM atom sitting at origin, then atomic positions were fully optimized. Final atomic positions are summarized in Table 4.2. Calculations were carried out by using the film-FLAPW [117,118] method based on the GGA [103] with +U [126]. A cut-off of $|\mathbf{k}+\mathbf{G}| \leq 3.6$ a.u.$^{-1}$ was used to expand the wave functions. The muffin-tin radii and lattice harmonic expansions for the charge and spin densities were 2.2 a.u., $\ell = 8$; 1.1 a.u., $\ell = 6$; and 0.8 a.u., $\ell = 4$ for the TM, C, and H atoms, respectively.

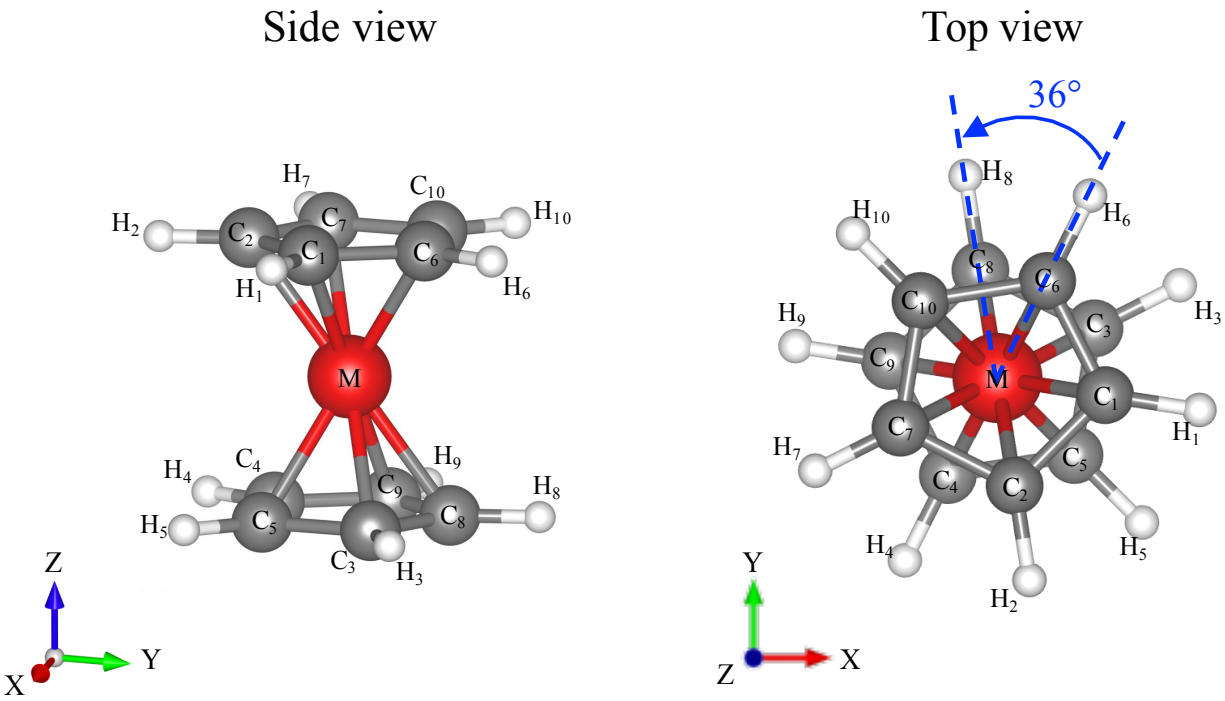

Figure 4.4: Side and top views of structure of a metallocene where large (red), middle (gray), and small (white) circles indicate transition-metal, carbon, and hydrogen atoms, respectively. Labeled atomic numbers correspond to the ones in Table 4.2. In D_{5d} symmetry, the top and bottom ligand Cp rings are rotated relatively by 36 degree (°).

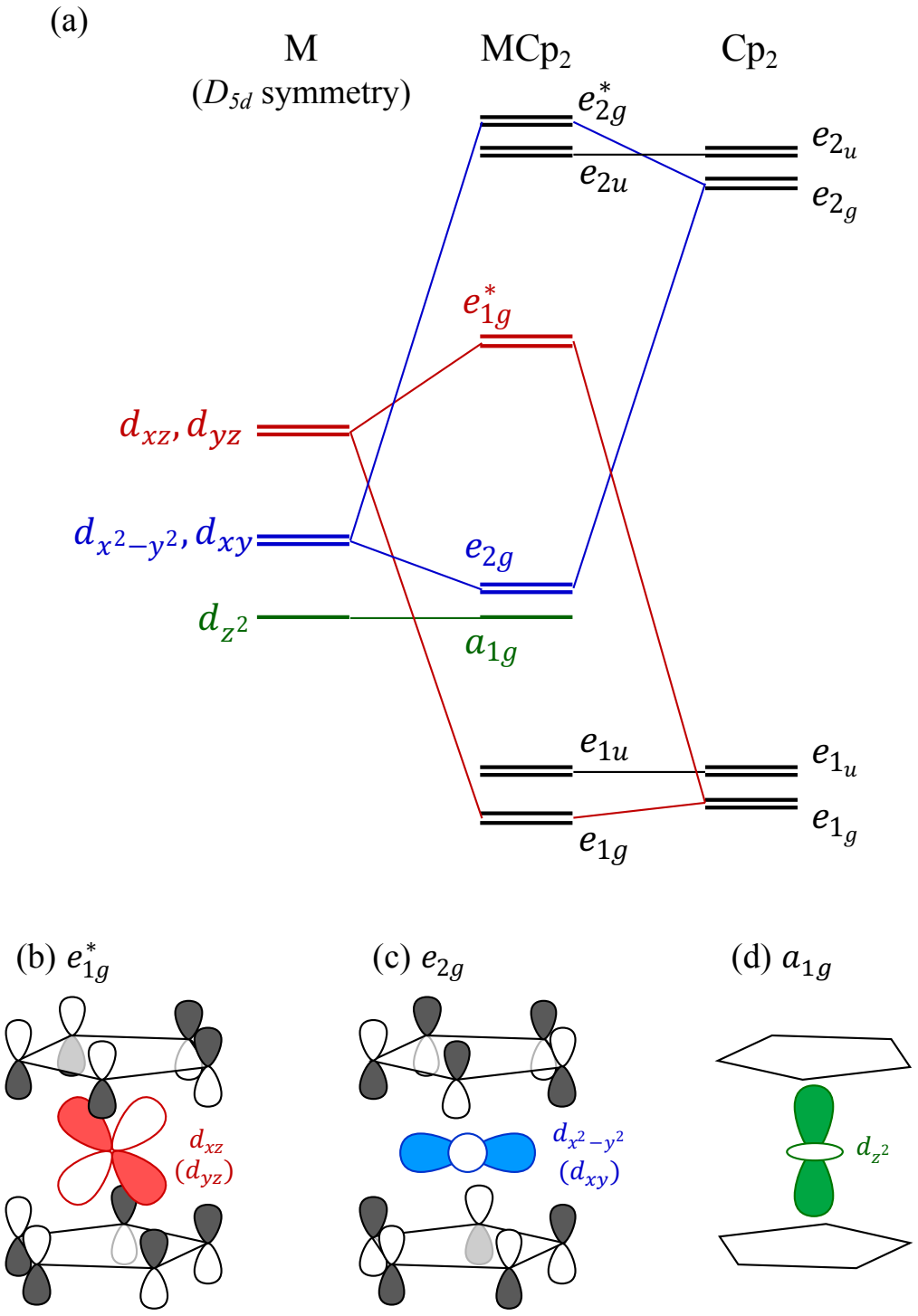

Figure 4.5: (a) Schematic of the energy diagrams of the crystal-field splitting of trantision-metal (TM) d orbitals for D_{5d} symmetry, the molecular orbitals in the two cycropentadienyl rings Cp$_2$, and the hybridized orbitals in the TNCp$_2$. (b), (c), and (d) Schematics of the molecular e^*_{1g} (antibonding TM $d_{xz,yz}$–Cp$_2$ e_{1g}), e_{2g} (bonding TM $d_{x^2-y^2,xy}$–Cp$_2$ e_{2g}), and a_{1g} (TM d_{z^2}) states in TMCp$_2$.

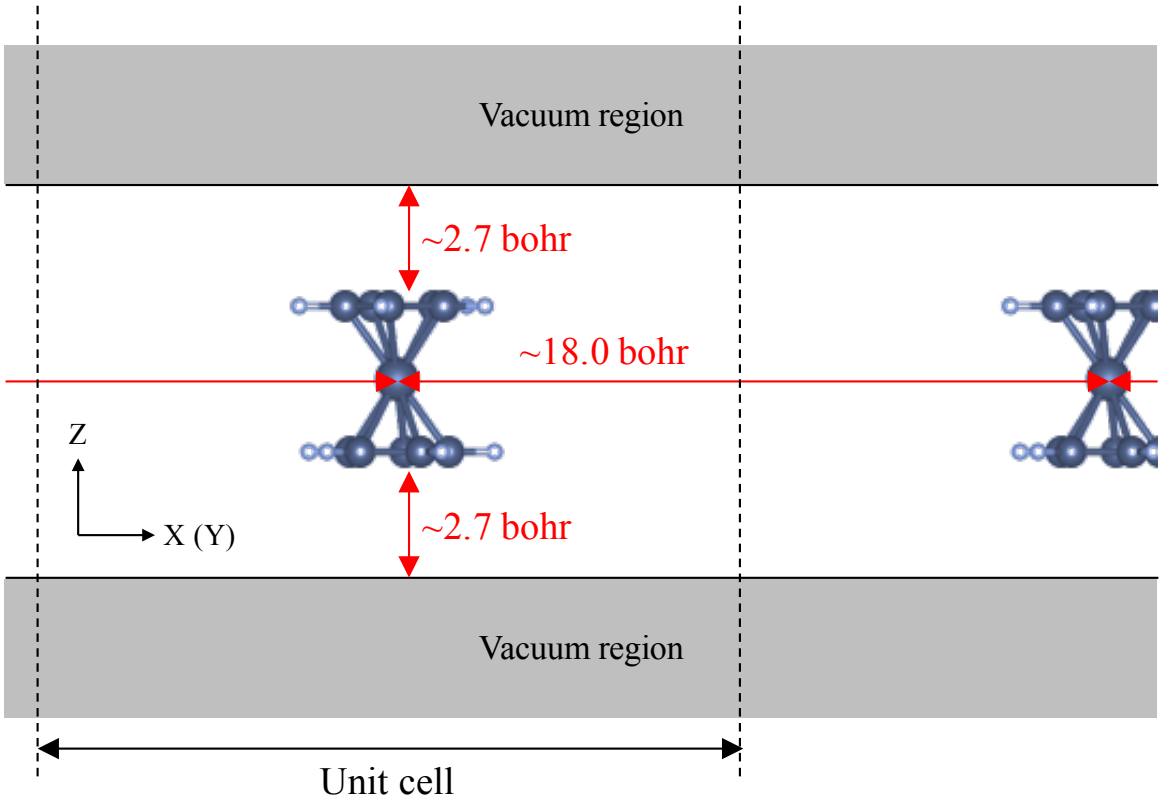

Figure 4.6: Isolated single $TMCp_2$ molecule in the slab model with vacuum regions of both sides separated by 2.7 bohr and large lattice constant of 18 bohr in xy plane.

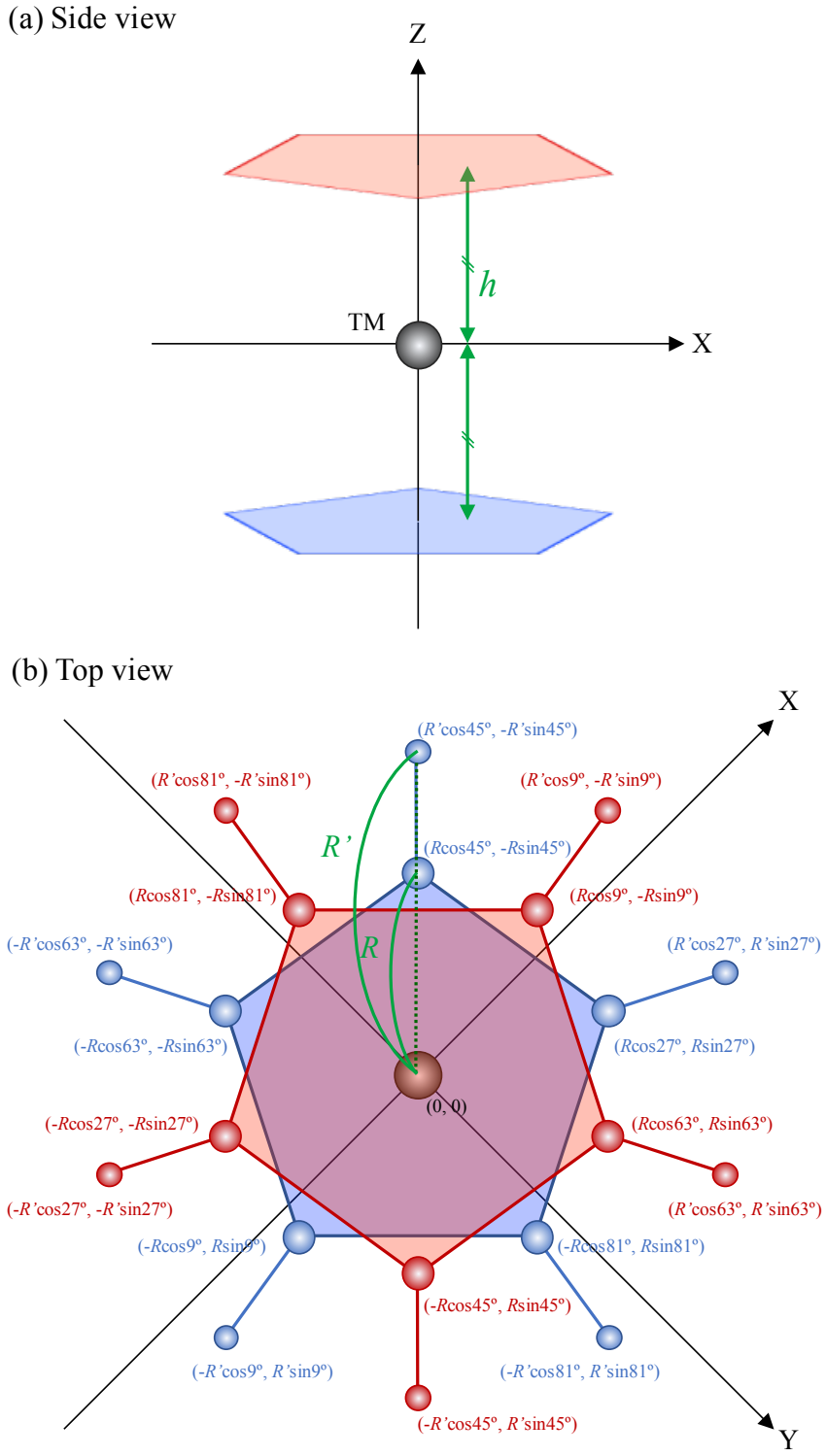

Figure 4.7: Geometric structure for $TMCp_2$ from (a) side and (b) top views where black, red, and blue circles indicate TM, top and bottom ligand Cp rings (C_5H_5), respectively. Parameters, h, R, and R' are given from Table 4.1 for $TMCp_2$ with TM of V, Cr, Mn, Fe, Co, and Ni.

Table 4.1: Geometric parameters, h, R, and R', for $TMCp_2$ in the unit of angstrom (Å). Definitions of variables are shown in Fig. 4.7.

	VCp_2	$CrCp_2$	$MnCp_2$	$FeCp_2$	$CoCp_2$	$NiCp_2$
h	1.967	1.897	2.083	1.685	1.776	1.868
R	1.215	1.214	1.216	1.219	1.216	1.216
R'	2.301	2.300	2.302	2.304	2.301	2.301

Table 4.2: Cartesian atomic position after fully optimization in the unit of Å. The labeled atoms, C_i and H_i ($i = 1 \sim 10$), correspond to the ones shown in Fig. 4.5.

	VCp_2			$CrCp_2$			$MnCp_2$		
	X	Y	Z	X	Y	Z	X	Y	Z
TM	0.000	0.000	0.000	0.000	0.000	0.000	0.000	0.000	0.000
C_1	1.212	-0.194	1.959	1.120	-0.108	1.972	1.213	-0.180	1.777
C_2	0.194	-1.212	1.959	0.108	-1.120	1.972	0.180	-1.213	1.777
C_3	1.093	0.557	-1.960	1.179	0.486	-1.799	1.102	0.545	-1.840
C_4	-0.557	-1.093	-1.960	0.486	-1.179	-1.799	-0.545	-1.102	-1.840
C_5	0.865	-0.865	-1.962	0.953	-0.953	-1.681	0.867	-0.867	-1.881
C_6	0.557	1.093	1.960	0.486	1.179	1.799	0.545	1.102	1.840
C_7	-1.093	-0.557	1.960	-1.179	-0.005	1.799	-1.102	-0.545	1.840
C_8	-0.194	1.212	-1.959	-0.108	1.120	-1.972	-0.180	1.213	-1.777
C_9	-1.212	0.194	-1.959	-1.120	0.108	-1.972	-1.213	0.180	-1.777
C_{10}	-0.865	0.865	1.962	-0.953	0.953	1.681	-0.867	0.867	1.881
H_1	2.276	-0.361	1.964	2.178	-0.285	2.067	2.279	-0.343	1.799
H_2	0.361	-2.276	1.964	0.285	-2.178	2.067	0.343	-2.279	1.799
H_3	2.054	1.044	-1.964	2.129	0.991	-1.761	2.069	1.022	-1.863
H_4	-1.044	-2.054	-1.964	-0.991	-2.129	-1.761	-1.022	-2.069	-1.863
H_5	1.627	-1.627	-1.963	1.710	-1.710	-1.571	1.630	-1.630	-1.908
H_6	1.044	2.054	1.964	0.991	2.129	1.761	1.022	2.069	1.863
H_7	-2.054	-1.044	1.964	-2.129	-0.991	1.761	-2.069	-1.022	1.863
H_8	-0.361	2.276	-1.964	-0.285	2.178	-2.067	-0.343	2.279	-1.799
H_9	-2.276	0.361	-1.964	-2.178	-0.285	-2.067	-2.279	0.343	-1.799
H_{10}	-1.627	1.627	1.963	-1.710	1.710	1.571	-1.630	1.630	1.908

	$FeCp_2$			$CoCp_2$			$NiCp_2$		
	X	Y	Z	X	Y	Z	X	Y	Z
TM	0.000	0.000	0.000	0.000	0.000	0.000	0.000	0.000	0.000
C_1	1.214	-0.193	1.684	1.228	-0.177	1.697	1.211	-0.193	1.873
C_2	0.193	-1.214	1.684	0.177	-1.228	1.697	0.193	-1.211	1.873
C_3	1.094	0.560	-1.685	1.087	0.588	-1.736	1.092	0.559	-1.874
C_4	-0.560	-1.094	-1.685	-0.588	-1.087	-1.736	-0.559	-1.092	-1.874
C_5	0.868	-0.868	-1.685	0.850	-0.850	-1.691	0.866	-0.866	-1.875
C_6	0.560	1.094	1.685	0.588	1.087	1.736	0.559	1.092	1.874
C_7	-1.094	-0.560	1.685	-1.087	-0.588	1.736	-1.092	-0.559	1.874
C_8	-0.193	1.214	-1.684	-0.177	1.228	-1.697	-0.193	1.211	-1.873
C_9	-1.214	0.193	-1.684	-1.228	0.177	-1.697	-1.211	-0.193	-1.873
C_{10}	-0.868	0.868	1.685	-0.850	0.850	1.691	-0.866	0.866	1.875
H_1	2.278	-0.360	1.681	2.291	0.358	1.682	2.275	-0.360	1.862
H_2	0.360	-2.278	1.681	0.358	-2.291	1.682	0.360	-2.275	1.862
H_3	2.055	1.045	-1.682	2.058	1.058	-1.736	2.053	1.043	-1.862
H_4	-1.045	-2.055	-1.682	-1.058	-2.058	-1.736	-1.043	-2.053	-1.862
H_5	1.629	-1.629	-1.681	1.611	-1.611	-1.674	1.626	-1.626	-1.862
H_6	1.045	2.055	1.682	1.058	2.058	1.736	1.043	2.053	1.862
H_7	-2.055	-1.045	1.682	-2.058	-1.058	1.736	-2.053	-1.043	1.862
H_8	-0.360	2.278	-1.681	-0.358	1.762	-1.682	-0.360	2.275	-1.862
H_9	-2.278	0.360	-1.681	-2.291	0.358	-1.682	-2.275	0.360	-1.862
H_{10}	-1.629	1.629	1.681	-1.611	1.611	1.674	-1.626	1.626	1.862

4.3 Electronic configurations in GGA

In the constraint DFT approach, the total energies of all electronic configurations that are allowed by a symmetric group were calculated self-consistently with the Lagrange multipliers so as to energetically determine the ground state electronic configuration. A part of the candidates of electronic configurations are;

- VCp_2
  - ${}^4A_{2g}\ ((d_{z^2})^1, (d_{x^2-y^2(xy)})^2, (d_{xz(yz)})^0)$
  - ${}^2E_{2g}\ ((d_{z^2})^2, (d_{x^2-y^2(xy)})^1, (d_{xz(yz)})^0)$
- $CrCp_2$
  - ${}^1E_{1g}\ ((d_{z^2})^2, (d_{x^2-y^2(xy)})^2, (d_{xz(yz)})^0)$
  - ${}^1A_{1g}\ ((d_{z^2})^0, (d_{x^2-y^2(xy)})^4, (d_{xz(yz)})^0)$
  - ${}^3A_{1g}\ ((d_{z^2})^2, (d_{x^2-y^2(xy)})^2, (d_{xz(yz)})^0)$
  - ${}^3E_{2g}\ ((d_{z^2})^1, (d_{x^2-y^2(xy)})^3, (d_{xz(yz)})^0)$
  - ${}^5E_{2g}\ ((d_{z^2})^1, (d_{x^2-y^2(xy)})^2, (d_{xz(yz)})^1)$
- $MnCp_2$
  - ${}^2A_{2g}\ ((d_{z^2})^1, (d_{x^2-y^2(xy)})^4, (d_{xz(yz)})^0)$
  - ${}^3E_{2g}\ ((d_{z^2})^2, (d_{x^2-y^2(xy)})^3, (d_{xz(yz)})^0)$
  - ${}^6A_{1g}\ ((d_{z^2})^1, (d_{x^2-y^2(xy)})^2, (d_{xz(yz)})^2)$
- $FeCp_2$
  - ${}^1A_{1g}\ ((d_{z^2})^2, (d_{x^2-y^2(xy)})^4, (d_{xz(yz)})^1)$
  - ${}^5A_{1g}\ ((d_{z^2})^2, (d_{x^2-y^2(xy)})^2, (d_{xz(yz)})^2)$
- $CoCp_2$
  - ${}^2E_{1g}\ ((d_{z^2})^2, (d_{x^2-y^2(xy)})^4, (d_{xz(yz)})^1)$
  - ${}^4A_{2g}\ ((d_{z^2})^1, (d_{x^2-y^2(xy)})^4, (d_{xz(yz)})^2)$

- $NiCp_2$
  - $^1E_{2g}$ $((d_{z^2})^2, (d_{x^2-y^2(xy)})^4, (d_{xz(yz)})^2)$
  - $^3A_{2g}$ $((d_{z^2})^2, (d_{x^2-y^2(xy)})^4, (d_{xz(yz)})^2)$

At first, the $FeCp_2$ is focused. The calculated results show that the $d_{x^2-y^2,xy}$ and d_{z^2} states are fully occupied with respective electron occupations over 0.7 (electrons) in Table 4.3, and a large energy gap of 2.8 eV appears between the highest occupied molecular orbital (HOMO) and lowest unoccupied molecular orbital (LUMO), forming a closed shell with $^1A_{1g}$ symmetry. Figure 4.8 shows calculated electron charge density distributions of HOMO and LUMO states, where hybridizations of the Fe $d_{x^2-y^2,xy}$ – Cp_2 e_{2g} and Fe $d_{xz,yz}$ – Cp_2 e_{1g} can be confirmed. This is consistent with the molecular-orbital energy diagram presented in Fig. 4.5 (a). No stationary solutions of the other electronic configurations were observed in the constraint DFT calculations, even for large constraint field μ_n up to 10 eV. Thus, it is expected that the electronic configuration of the $^1A_{1g}$ state is energetically the most stable as expected from the "18-electron rule" describing stable metal complexes.

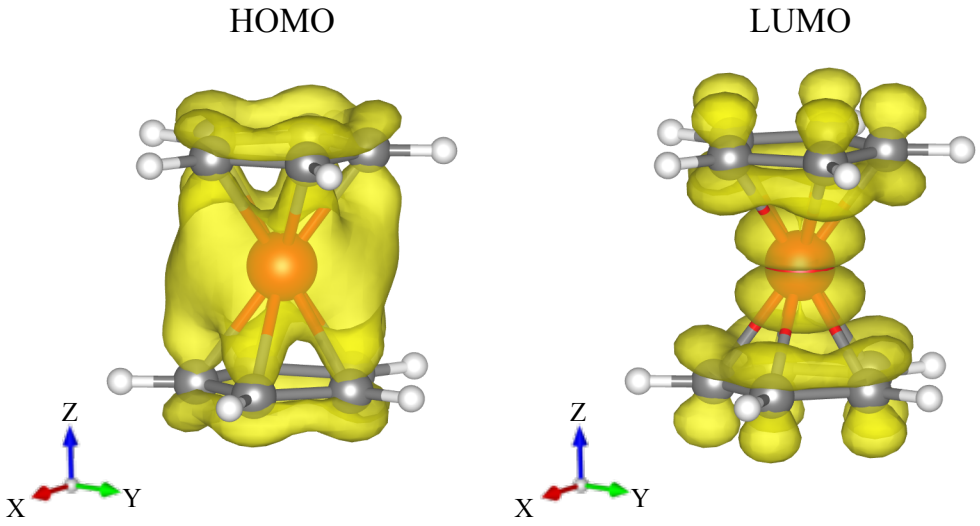

Figure 4.8: Calculated charge density distributions for (left) HOMO and (right) LUMO for the $FeCp_2$ of $^1A_{1g}$.

Table 4.3: d-electron occupation numbers for obtained electronic configuration (E.C.) for $TMCp_2$ calculated within GGA. Strength of applied constraint field μ in the unit of eV and the d-orbitals applied μ with spin-channel are also listed.

	E.C.	μ (eV)	Constrained d-orbital	Majority					Minority				
				z^2	x^2-y^2	xy	xz	yz	z^2	x^2-y^2	xy	xz	yz
VCp_2	$^2A_{2g}$	0.00	-	0.7585	0.7204	0.7219	0.2170	0.2170	0.0238	0.0032	0.0032	0.1493	0.1493
$CrCp_2$	$^3E_{2g}$	0.00	-	0.8117	0.7566	0.6884	0.3216	0.3216	0.0369	0.0095	0.5981	0.2406	0.2406
	$^3A_{1g}$	-1.36	$d^{\downarrow}_{x^2-y^2,xy}$	0.7693	0.7374	0.2806	0.2800	0.7524	0.7629	0.0107	0.0079	0.2161	0.2161
	$^1E_{1g}$	1.36	$d^{\uparrow}_{z^2}, d^{\downarrow}_{xy}$	0.7460	0.0108	0.7044	0.2677	0.2677	0.7460	0.0108	0.7044	0.2677	0.2677
$MnCp_2$	$^2E_{2g}$	0.00	-	0.8171	0.7423	0.8074	0.3316	0.3316	0.7983	0.7097	0.0095	0.2769	0.2769
	$^6A_{1g}$	-2.72	$d^{\downarrow}_{xz,yz}$	0.9021	0.9047	0.9045	0.9436	0.9436	0.0169	0.0022	0.0021	0.1053	0.1053
	$^2A_{2g}$	1.36	$d^{\uparrow}_{z^2}$	0.8456	0.7235	0.7529	0.3734	0.3734	0.0323	0.6610	0.6960	0.3172	0.3172
$FeCp_2$	$^1A_{1g}$	0.00	-	0.8568	0.7484	0.7473	0.3942	0.3942	0.8568	0.7484	0.7473	0.3942	0.3942
$CoCp_2$	$^2E_{1g}$	0.00	-	0.8883	0.8253	0.8236	0.7490	0.7390	0.8771	0.7980	0.7975	0.3993	0.3993
$NiCp_2$	$^3A_{2g}$	0.00	-	0.9150	0.8962	0.8958	0.9763	0.9763	0.9909	0.8751	0.8747	0.4421	0.4421

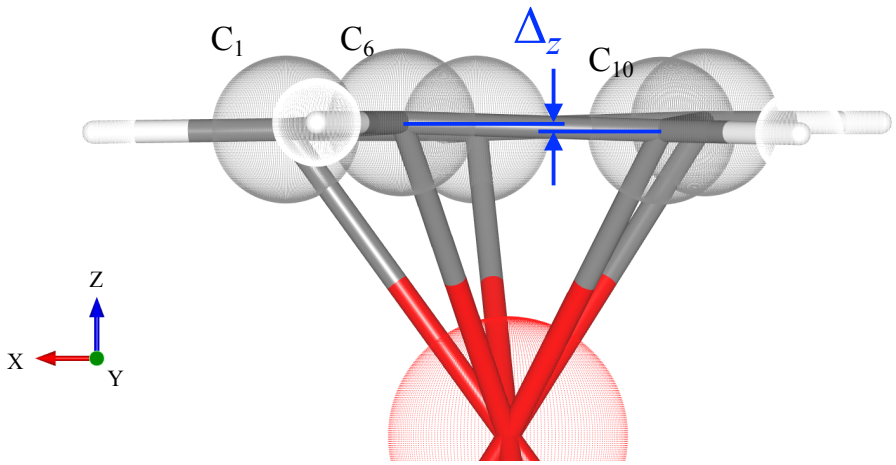

Figure 4.9: The Jahn-Teller distorted molecular structure for the $CoCp_2$ of $^2E_{1g}$. Difference of z position, Δ_z is defined by $\Delta_z = z(C_{6(7)}) - z(C_{10}) = 0.045$ Å.

For the $CoCp_2$ and $NiCp_2$, since the number of electrons is larger than that of the $FeCp_2$, the doublet $d_{xz,yz}$ is occupied by a single electron for $CoCp_2$ and by two electrons for $NiCp_2$ (see Table 4.3), leading to $^2E_{1g}$ and $^3A_{2g}$ ground states, respectively. In both molecules, no stationary solutions of the other electronic configurations exist in the GGA. Calculations confirmed that for the $^2E_{1g}$ state of the $CoCp_2$, the degeneracy in the doublet $d_{xz,yz}$ occupied by a single electron is removed. In terms of atomic position in Table 4.1, one can see that the D_{5d} symmetric molecular structure is distorted: for example, z-position of $C_{6(7)}$ differs from that of C_{10} by $\Delta_{CoCp_2} = z(C_{6(7)}) - z(C_{10}) = 0.045$ Å (see Fig. 4.9) which is forty-five times greater than $\Delta_{FeCp_2} = z(C_{6(7)}) - z(C_{1(2)}) = 0.001$ Å in $FeCp_2$. This distortion is induced by Jahn-Teller effect and then the symmetry of D_{5d} is degraded to C_{2h}. The predicted ground states of $CoCp_2$ and $NiCp_2$ agree with experiments [171, 174, 175].

For $MnCp_2$, where the number of electrons is smaller than in $FeCp_2$, a low-spin $^2E_{2g}$ state is found as a solution of standard DFT scheme. Interestingly, addtional two different electronic configurations are obtained by extended constraint DFT approach. By an introduction of constraint field of -2.72 eV to minority $d_{xz,yz}$ orbital ($\mu^{\downarrow}_{xz,yz} = -2.72$ eV), $^6A_{1g}$ state, in which all of d^5 electrons occupied in parallel resulting in high-spin state, is obtained. Contrary, when positive constraint field is applied to d_{z^2}-orbital in majority-spin states, $\mu^{\uparrow}_{z^2} = 1.36$ eV, a low-spin $^2A_{1g}$ structure is confirmed. The d-electron occupancies in each electronic configuration are listed in Table 4.3. The constraint DFT calculations, secondary, reduced applied constraint field so as to get a solution that corresponds to the standard unconstraint DFT equation.

Figure 4.10 (a) shows relative total energy difference as a function of applied constraint field, μ. If a strength of $\mu^{\downarrow}_{xz,yz}$ is reduced to zero, finally unconstrained solution of $^6A_{1g}$ is produced: this result is regarded as a significance because the constraint DFT calculations achieve additional stationary electronic configuration to the conventional DFT method. In the same manner, the $d^{\uparrow}_{z^2}$ is dwindled to get $^2A_{1g}$ at $\mu = 0$, but if μ of less than 0.82 eV, $^2A_{1g}$ moves into $^2E_{2g}$ state: in other words, solution of the $^2A_{1g}$ without constraining d electrons can not be achieved. Finally, the calculated total energy indicates the ground state is $^2E_{2g}$, and the metastable of the $^6A_{1g}$ state with higher energy by 0.77 eV. This result is in contrast to the previous +U calculations where the $^2E_{2g}$ state was predicted. [172]

For $CrCp_2$, standard GGA-based DFT calculations give stationary solution for $^3E_{2g}$ without any constraint fields to d-orbital electrons. By performing the constraint DFT calculations based on the procedures presented in previous paragraph for $MnCp_2$, another $^3A_{1g}$ state is provided using $\mu^{\downarrow}_{x^2-y^2} = 2.72$ eV, and then this configuration is preserved if the $\mu^{\downarrow}_{x^2-y^2}$ decreased to 0.0 eV finally. Note that total energy at zero point of μ is evaluated after full relaxation in molecular structure. Low-spin $^1E_{1g}$ never be stabilized by a set of μ at zero-point (see Fig. 4.10 (b)). Fully optimized molecular structure is visualized in Fig. 4.11. The ligand two Cp_2 rings are tilted a few degrees while remaining parallel to each other. This distortion which is induced by Jahn-Teller effect makes a degeneracy of doublet d_{2g} orbital be solved, thus the $^3E_{2g}$ state result in a ground state with the total energy of $^3E_{2g}$ state lower than the $^3A_{1g}$ one by 0.32 eV.

In VCp_2, the ground state is predicted to be $^4A_{2g}$ in GGA. No other stationary solutions were found, even for large constraint fields. This results is not surprising since the singlet d_{z^2} and the doublet $d_{x^2-y^2,xy}$ in the majority spin states are fully occupied, which stabilizes the high spin state.

Finally, Fig. 4.12 summarizes the energy positions of d orbital in the ground-state electronic configurations for studied $TMCp_2$ (TM=V, Cr, Mn, Fe, Co, and Ni) in GGA. Table 4.4 compares the ground states obtained in our calculations with previous studies: theoretical results by GGA+U [172] and hybrid functional (B3LYP) [173] calculations, and experiments [171, 174, 175]. With the electronic configuration of $FeCp_2$ which satisfies the 18-electron rule [176] as a reference, spin multiplicity $(2S + 1)$ of Eq. (4.2) simply increases due to one and two more electrons for later TM atoms, i.e., Co and Ni, while it decreases due to one,

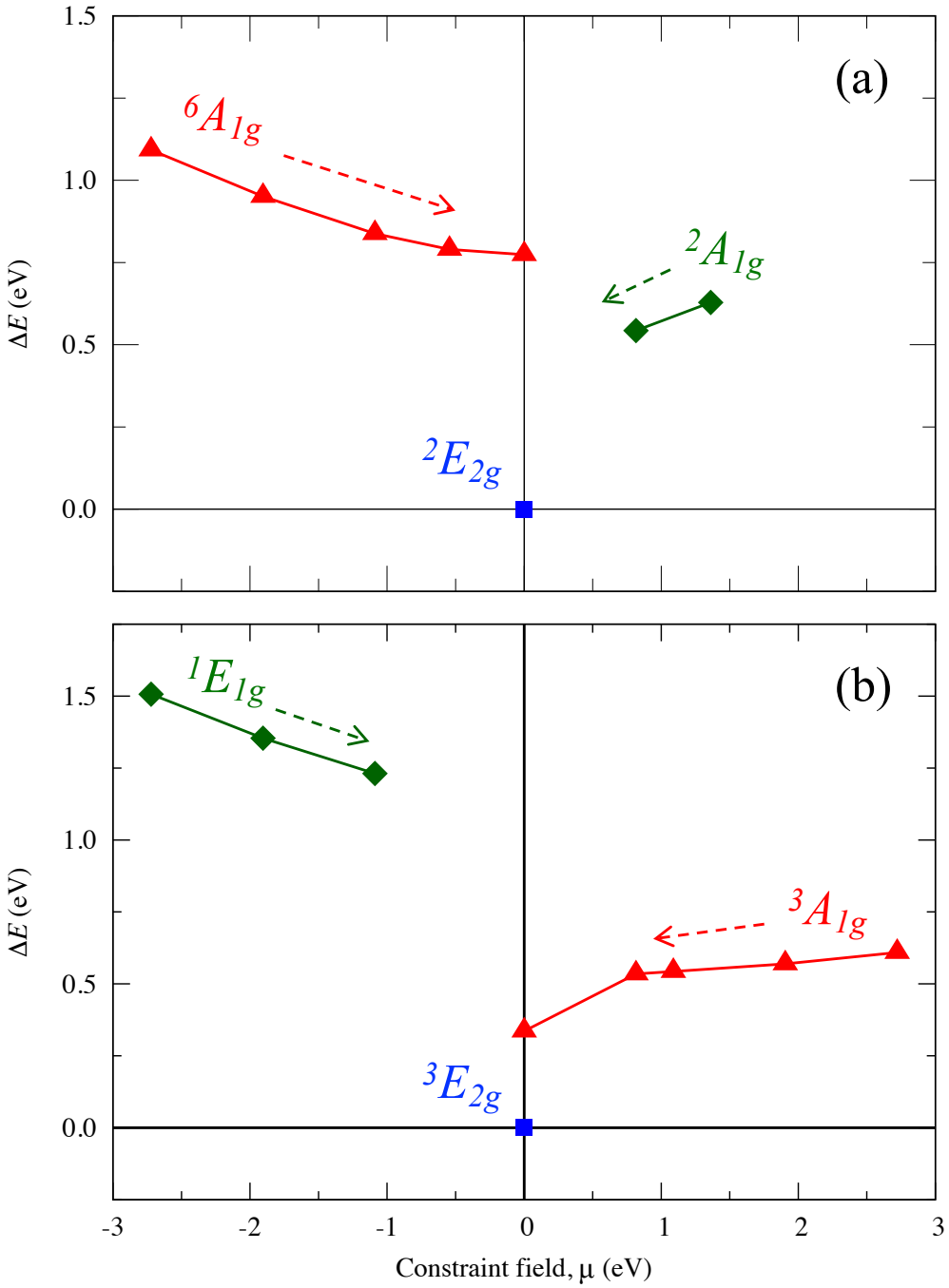

Figure 4.10: The total-energy difference, ΔE, with respect to the applied constraint field, μ, for (a) $MnCp_2$ and (b) $CrCp_2$. For (a) $MnCp_2$, closed squares, triangles, and diamonds indicate the solution for $^2E_{2g}$, $^6A_{1g}$, and $^2A_{1g}$, and for (b) $CrCp_2$, $^3E_{2g}$, $^3A_{1g}$, and $^1E_{1g}$, respectively. The plots at $\mu = 0$ correspond to a solution without any constraint fields.

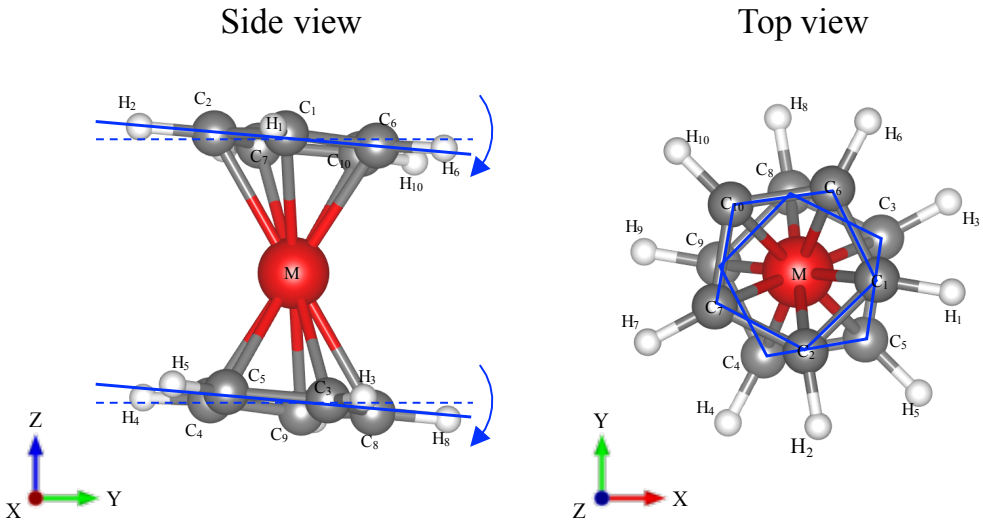

Figure 4.11: The Jahn-Teller distorted molecular structure for the $CrCp_2$ of $^3E_{2g}$.

tow, and three less electrons for earlier TMs, i.e., Mn, Cr, and V, respectively. This tendency mostly agrees with the experiments, but only $MnCp_2$ seems to be still questionable, unfortunately. The hybrid B3LYP calculations which is well-known as a powerful technique for treating organometallic molecules predicted the high-spin $^6A_{1g}$, in agreement with experiments, whereas DFT-based results including present and GGA+U [172] calculations obtained low-spin ground state $^2E_{2g}$. Furthermore, in $CrCp_2$, even though the spin multiplicity $2S+1 = 3$ is identical, the configuration of occupied electrons ($^3E_{2g}$) disagrees with previous calculations ($^3A_{1g}$) [172,173].

Table 4.4: Ground state electronic configurations in the present constraint DFT calculations for both GGA and GGA+U, compared to previous GGA+U (U_{eff} of 3.0 eV) and hybrid functional (B3LYP), and experiments for $TMCp_2$ (TM=V, Cr, Mn, Fe, Co, Ni). The U_{eff} (in eV) in the parentheses of the third column are determined from constraint DFT calculations based on the linear response theory.

	Present calculations		Previous calculations		Experiments [168–171]
	GGA	GGA+U (U_{eff})	GGA+U [172]	B3LYP [173]	
V	$^4A_{2g}$	$^4A_{2g}$ (2.3)	$^4A_{1g}$ [a]	$^4A_{1g}$ [a]	$^4A_{2g}$
Cr	$^3E_{2g}$	$^3E_{2g}$ (2.3)	$^3A_{1g}$	$^3A_{1g}$	$^3E_{2g}$
Mn	$^2E_{2g}$	$^6A_{1g}$ (2.4)	$^2E_{2g}$	$^6A_{1g}$	$^6A_{1g}$
Fe	$^1A_{1g}$	$^1A_{1g}$ (2.5)	$^1A_{1g}$	$^1A_{1g}$	$^1A_{1g}$
Co	$^2E_{1g}$	$^2E_{1g}$ (2.6)	$^2E_{1g}$	$^2E_{1g}$	$^2E_{1g}$
Ni	$^3A_{2g}$	$^3A_{2g}$ (2.4)	$^3A_{2g}$	$^3A_{2g}$	$^3A_{2g}$

[a] Electronic configuration in Refs. [172,173] is identical to that of $^4A_{2g}$.

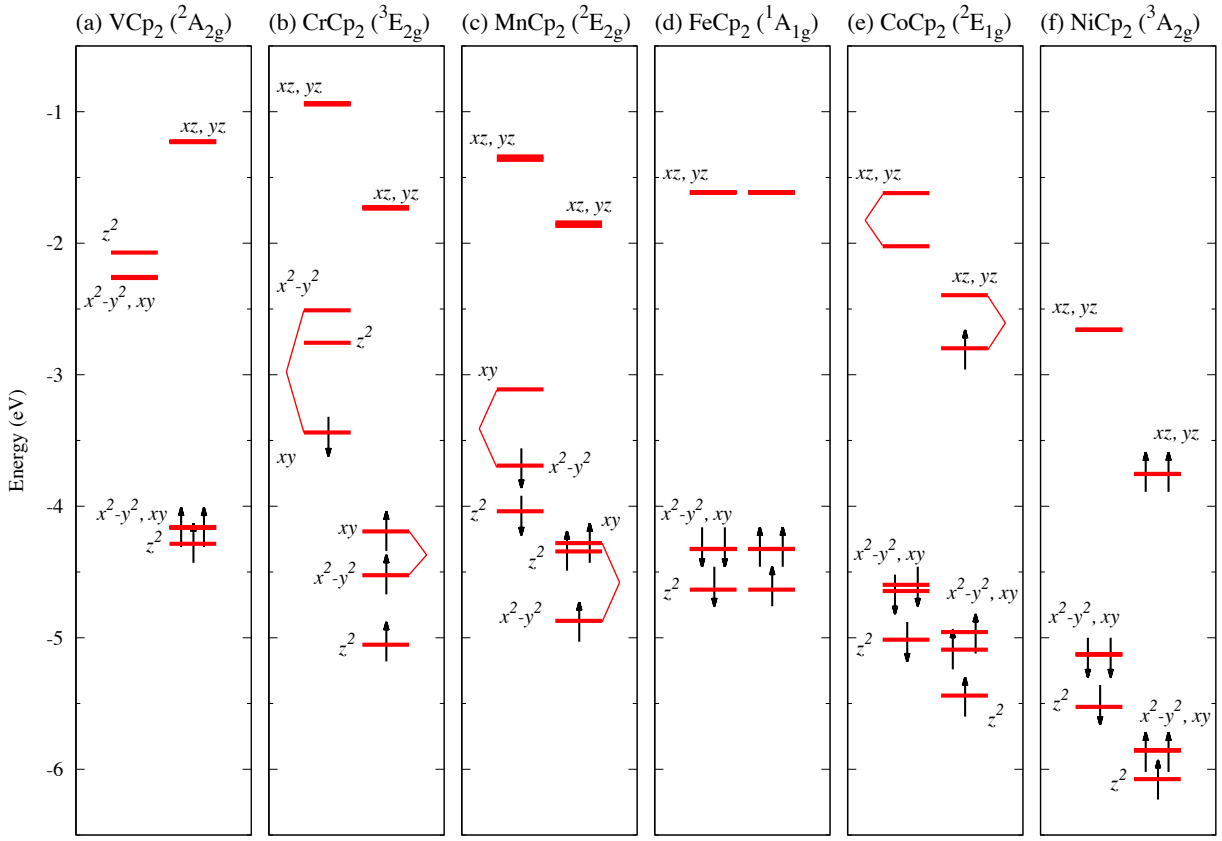

Figure 4.12: Energy diagram of the d orbitals in (a) VCp_2 ($^4A_{2g}$), (b) $CrCp_2$ ($^3E_{2g}$), (c) $MnCp_2$ ($^2E_{2g}$), (d) $FeCp_2$ ($^1A_{1g}$), (e) $CoCp_2$ ($^2E_{1g}$), and (f) $NiCp_2$ ($^3A_{2g}$), calculated using GGA. Up and down arrows indicate the electron occupations of the majority and minority spin states, respectively. The reference energy (0 eV) is set to the vacuum level.

4.4 Electronic configurations in extended GGA+U

As mentioned in the introduction, the correlation effects are of importance when considering the electronic configurations of organometallic molecules. For all models, GGA+U calculations are performed to investigate the stability of different electronic configurations, in which the value of effective on-site Coulomb U_{eff} varies from zero (GGA) to 8 eV. The U_{eff} values are obtained based on the procedures discussed in the previous chapter.

Interestingly, for $MnCp_2$ the electron correlations (+U) affects the stability of electronic configurations of the ${}^2E_{2g}$ and ${}^6A_{1g}$. Fig. 4.13 (a) shows the relative total energy, ΔE, between them with respect to the varying U_{eff}, where the molecular structures were fully optimized at each U_{eff}. It can be easily seen that the stability between them is found to be very sensitive depending on the U_{eff}. When U_{eff} increases, ΔE for the ${}^6A_{1g}$ configuration monotonically decreases, and this state becomes stable for U_{eff} greater than ~ 2 eV, where the total energies of the ${}^6A_{1g}$ and ${}^2E_{2g}$ states are nearly degenerate. In order to get the non-empirical U_{eff}, linear response calculations based on the constraint DFT was performed: a change of the Mn d-electron occupations with respect to the constraint field μ is shown in Fig. 4.14 (c). Then calculations using response functions of KS and SCF terms give the $U_{\text{eff}}^{\text{LRT}}$ of 2.4 eV. In that case, present constraint DFT+U calculations provides a ground state of the ${}^6A_{1g}$ (Fig. 4.13 (a)), reproducing experiments [168–171]. Importantly, starting the self-consistent calculations with no constraints naturally yields the ${}^2E_{2g}$ solution: thus, in this case constraint DFT must be essential in the search for the true ground state.

Note that the ${}^2E_{2g}$ state could in principle be stabilized by the Jahn-Teller effect, i.e., a lifting of the degeneracy of the doublet $d_{x^2-y^2,xy}$ in the minority spin states. However, the ${}^6A_{1g}$ state — with fully occupied majority-spin states and empty minority — is still favorable due to the large exchange splitting arising from the electron correlation (+U) effects. Thus, the high spin electronic configuration with $S = 5/2$ μ_{B} is preferable, as expected by the Hund's first rule. As shown in Fig. 4.15 (a), the charge density difference, $\Delta\rho = \rho_{\text{MnCp}_2} - (\rho_{\text{Cp}_2} + \rho_{\text{Mn}})$, of the ${}^6\text{A}_{1\text{g}}$ state shows small changes of the d orbitals around Mn site but almost no changes in the molecular orbitals in the ligand Cp_2.

In $CrCp_2$, as shown in Fig. 4.13 (b), the energy difference ΔE for the ${}^3A_{1g}$ state decreases as U_{eff} increases and becomes stable when the U_{eff} is over 4 eV. For $U_{\text{eff}}^{\text{LRT}}$ (=2.3 eV), the ground

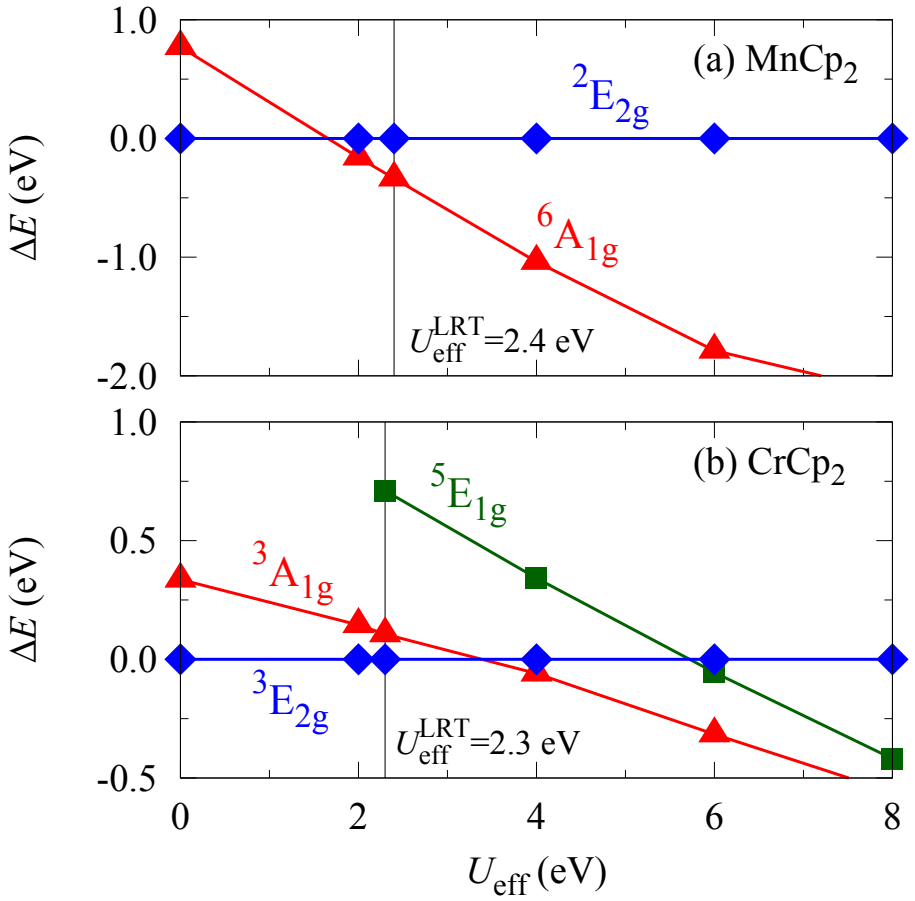

Figure 4.13: Total energy differences among the electronic configurations, ΔE, as a function of U_{eff} for (a) $MnCp_2$ and (b) $CrCp_2$. Diamond (blue) and triangle (red) in (a) represent the $^2E_{2g}$ and $^6A_{1g}$ states, respectively, and diamond (blue), triangle (red), and square (green) in (b), the $^3E_{2g}$, $^3A_{1g}$, and $^5E_{1g}$ states, respectively. $U_{\text{eff}} = 0$ eV correspond to the GGA results.

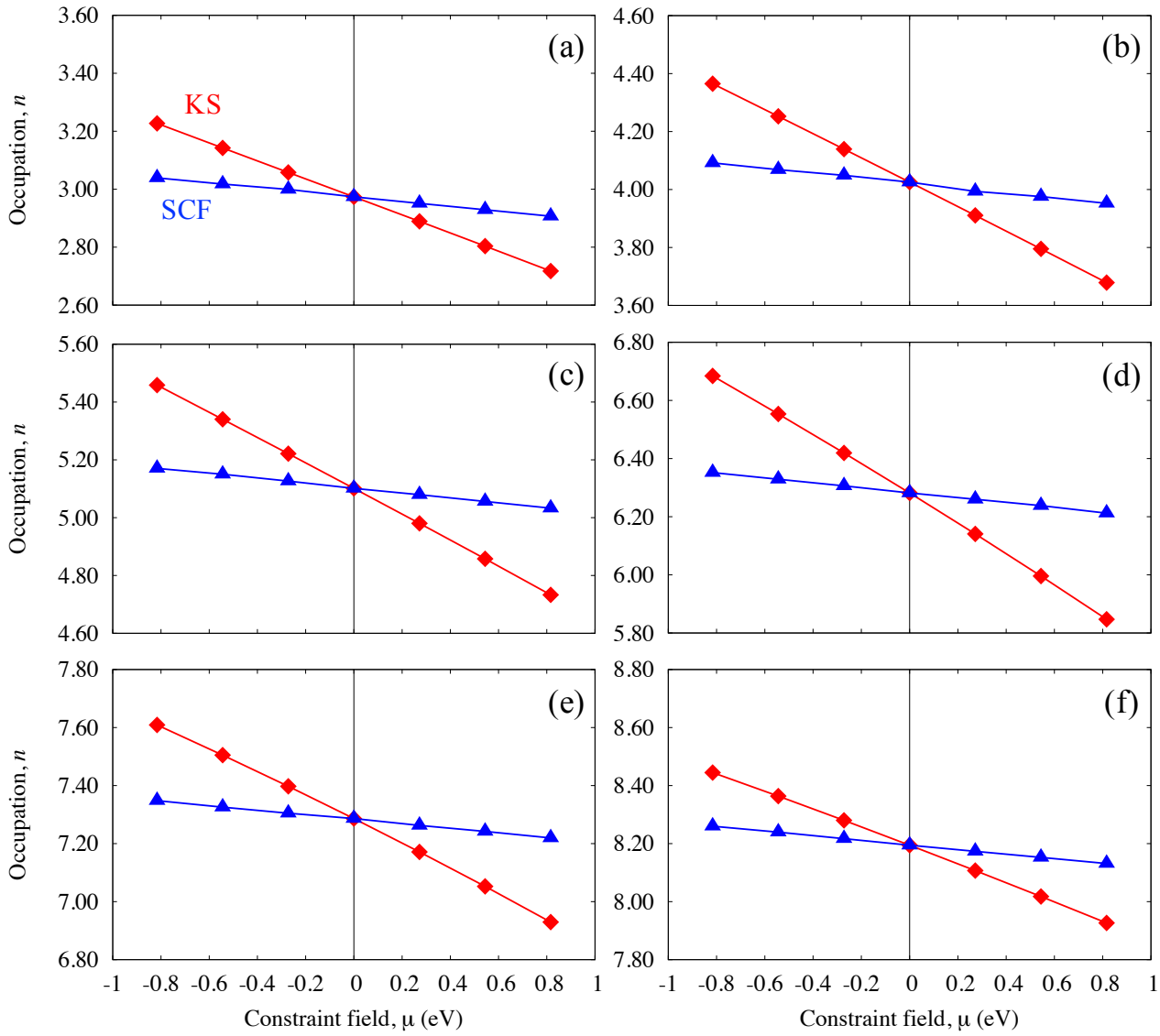

Figure 4.14: d-orbital occupation numbers with respect to the applied constraint field μ for (a) VCp_2, (b) $CrCp_2$, (c) $MnCp_2$, (d) $FeCp_2$, (e) $CoCp_2$, and (f) $NiCp_2$. Red and blue solid lines are Kohn-Sham (KS) and self-consistent-field (SCF) calculations.

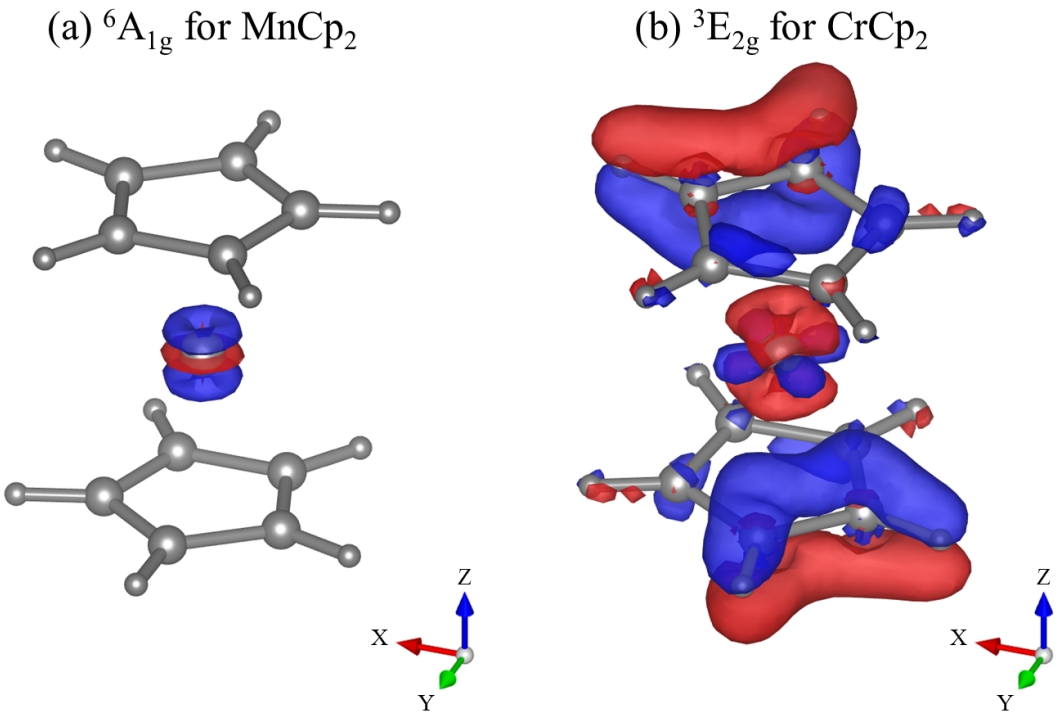

Figure 4.15: Charge density difference, $\Delta\rho = \rho_{\mathrm{MCp_2}} - (\rho_{\mathrm{Cp_2}} + \rho_{\mathrm{M}})$, for (a) $^6\mathrm{A_{1g}}$ $\mathrm{MnCp_2}$ and (b) $^3\mathrm{E_{2g}}$ $\mathrm{CrCp_2}$ for GGA+U with $U_{\mathrm{eff}}^{\mathrm{LRT}}$. The blue and red regions indicate positive (accumulation) and negative (depletion) differences, respectively.

state is the $^3E_{2g}$ state and the electronic configuration does not change due to electron correlation effects. As seen in Fig. 4.15 (b), the charge density difference has significant hybridization between the Cr $d_{x^2-y^2,xy}$ and $\mathrm{Cp_2}$ e_{2g} orbitals. In this system, the single occupation of the doublet $d_{x^2-y^2,xy}$ causes a Jahn-Teller distortion that leads to the $^3E_{2g}$ ground state. In contrast, the $^3A_{1g}$ state predicted by previous GGA+U [172] and B3LYP [173] calculations corresponds to the metastable state in the present constraint DFT calculations.

It is also demonstrated that the $U_{\mathrm{eff}}^{\mathrm{LRT}}$ values for $\mathrm{VCp_2}$, $\mathrm{FeCp_2}$, $\mathrm{CoCp_2}$, and $\mathrm{NiCp_2}$ are also obtained from linear response calculations: the values are almost the same for all molecules, varying between 2.3 and 2.6 eV. For $\mathrm{FeCp_2}$, there is no change in the ground state in the GGA+U compared to the GGA, still ground state corresponds to $^1A_{1g}$ state. The same situation can be seen even in $\mathrm{VCp_2}$, $\mathrm{CoCp_2}$, and $\mathrm{NiCp_2}$.

To conclude, the ground-state electronic configurations finally obtained by the GGA+U are listed in Table 4.4, in which the values of non-empirical U_{eff} are adopted, and the energy diagram of the d orbital is shown in Fig. 4.16. From the dependence of stability on the U_{eff}, it is clarified that the calculated ground states are very sensitive to the U_{eff} and to Jahn-Teller splittings.

The spin multiplicity of $S(= 2s + 1)$ has a maximum of $S = 6$ at $MnCp_2$ due to high-spin A_{1g} configuration induced by large exchange-splitting, while the S continuously decreases from VCp_2 ($S = 4$) to $FeCp_2$ (1), and then increases to $NiCp_2$ (3) in GGA calculations. As a result, predicted ground states are found to be in agreement with experiments in all of models. Thus, an utility of constraint DFT including electron correlations via non-empirical U_{eff} determined from linear response for predicting the properties of correlated systems was demonstrated.

Table 4.5: Calculated energy gap between HOMO and LUMO for the $TMCp_2$ by both of GGA and GGA+U methods in the unit of eV for obtained electronic configuration (E.C.) in $TMCp_2$. ΔE is given by difference between gap of GGA+U and that of GGA, $\Delta E = E_{\text{gap}}(\text{GGA} + \text{U}) - E_{\text{gap}}(\text{GGA})$.

	E.C.	E_{gap}		ΔE
		GGA	GGA+U	
VCp_2	$^4A_{2g}$	1.90	3.20	1.30
$CrCp_2$	$^3E_{2g}$	0.68	1.49	0.81
$MnCp_2$	$^2E_{2g}$	0.58	1.98	1.40
	$^6A_{1g}$	0.71	1.82	1.11
$FeCp_2$	$^1A_{1g}$	2.71	2.82	0.11
$CoCp_2$	$^2E_{1g}$	0.40	0.94	0.54
$NiCp_2$	$^3A_{2g}$	1.10	1.61	0.51

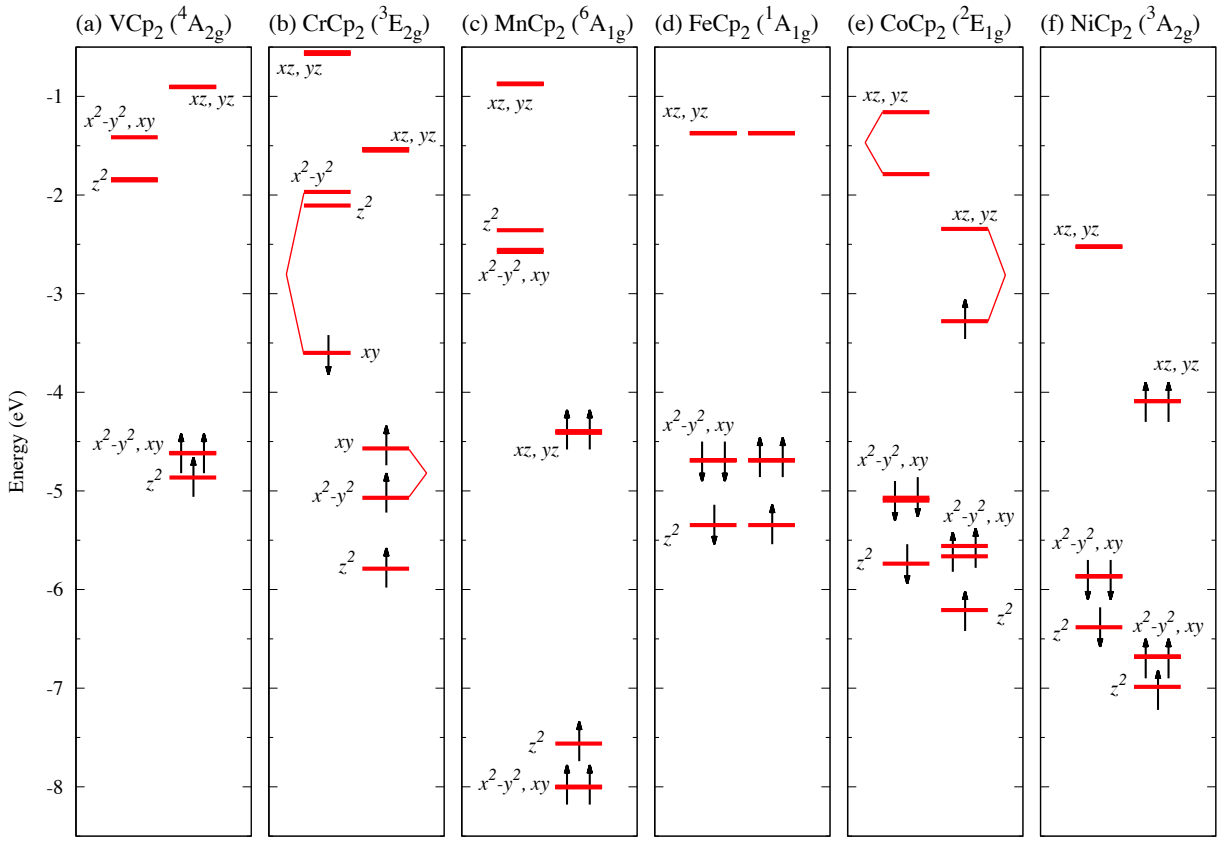

Figure 4.16: Energy diagram of the d orbitals in (a) VCp_2 ($^4A_{2g}$), (b) $CrCp_2$ ($^3E_{2g}$), (c) $MnCp_2$ ($^6A_{1g}$), (d) $FeCp_2$ ($^1A_{1g}$), (e) $CoCp_2$ ($^2E_{1g}$), and (f) $NiCp_2$ ($^3A_{2g}$), calculated using GGA+U with the $U_{\text{eff}}^{\text{LRT}}$ values in Table 4.4. Notation is the same as in Fig. 4.12.

4.5 Magnetic anisotropy

The present constraint DFT calculations have been performed for systematical investigation of magnetic anisotropy in $TMCp_2$. Magnetic anisotropy energy, $E_{\rm MA}$, is defined by the total energy difference between magnetizations orienting along the parallel (x-axis) and perpendicular (z-axis) directions to the Cp plane,

$$E_{\rm MA} = E^{\rm Total}(x) - E^{\rm Total}(z), \tag{4.3}$$

where the total energies $E^{\rm Total}$ are calculated with self-consistently incorporated the SOC following second variation procedures.

Firstly, the GGA-based $E_{\rm MA}$ for the ground state of ${}^4A_{2g}$ (for VCp_2), ${}^3E_{2g}$ ($CrCp_2$), ${}^2E_{2g}$ ($MnCp_2$), ${}^1A_{2g}$ ($FeCp_2$), ${}^2E_{1g}$ ($CoCp_2$), and ${}^3A_{2g}$ ($NiCp_2$), are presented by red color bars in Fig. 4.17. The magnetization of the $CoCp_2$ energetically favors to lie along the perpendicular direction to the Cp plane with $E_{\rm MA} = 0.46$ meV/molecule and for the $NiCp_2$, the parallel direction with -1.35 meV/molecule. Almost no preference in the magnetic easy direction for the VCp_2, $CrCp_2$, $MnCp_2$, and $FeCp_2$ is observed, where the $E_{\rm MA}$ is less than ~ 0.03 meV/molecule.

In order to clarify the role of the HOMO and LUMO states on the magnetic anisotropy for the $CoCp_2$ and $NiCp_2$, the energy contributions from the SOC interaction to the $E_{\rm MA}$ are evaluated based on the second-order perturbation theory [177]. The $E^{\rm 2nd}_{\rm MA}$ may be given as

$$E^{\rm 2nd}_{\rm MA} \approx \Delta E^{\uparrow\uparrow} + \Delta E^{\uparrow\downarrow}, \tag{4.4}$$

where

$$\Delta E^{\uparrow\uparrow} = E^{\uparrow\uparrow}(x) - E^{\uparrow\uparrow}(z) \tag{4.5}$$

$$= \xi(r)^2 \sum_{o^\uparrow, u^\uparrow} \frac{\left|\langle o^\uparrow|\hat{L_z}|u^\uparrow\rangle\right|^2 - \left|\langle o^\uparrow|\hat{L_x}|u^\uparrow\rangle\right|^2}{\varepsilon^\uparrow_u - \varepsilon^\uparrow_o} \tag{4.6}$$

$$\Delta E^{\uparrow\downarrow} = E^{\uparrow\downarrow}(x) - E^{\uparrow\downarrow}(z) \tag{4.7}$$

$$= \xi(r)^2 \sum_{o^\uparrow, u^\uparrow} \frac{\left|\langle o^\uparrow|\hat{L_x}|u^\downarrow\rangle\right|^2 - \left|\langle o^\uparrow|\hat{L_z}|u^\downarrow\rangle\right|^2}{\varepsilon^\downarrow_u - \varepsilon^\uparrow_o} \tag{4.8}$$

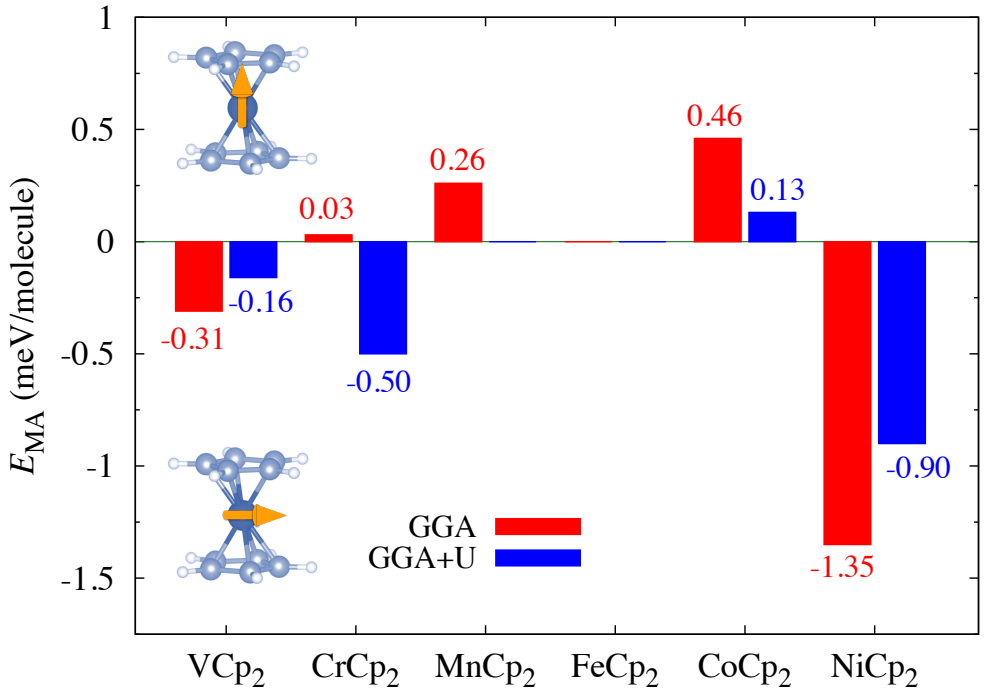

Figure 4.17: Calculated magnetic anisotropy energy, E_{MA}, of the $TMCp_2$ (TM=V, Cr, Mn, Fe, Co, and Ni), where positive and negative energies indicate that the magnetic easy axis lies along the perpendicular and parallel directions to the Cp ring plane, respectively. Red and blue bars correspond to the GGA and GGA+U calculations.

and $\xi(r)$ is the SOC constant, assumed to the calculated values of 38.3 and 47.9 meV for Co and Ni, respectively. The $\Delta E^{\uparrow\uparrow}$, which corresponds to the SOC between the occupied ($o^{\uparrow}$) and unoccupied ($u^{\uparrow}$) states in the majority-spin states, indicates that the same (different) magnetic quantum number, m, gives a positive (negative) contribution to the $E^{\mathrm{2nd}}_{\mathrm{MA}}$ through the $\hat{L}_z$ ($\hat{L}_x$) operator. For the $\Delta E^{\uparrow\downarrow}$, i.e., the SOC between the occupied majority-spin ($o^{\uparrow}$) and unoccupied minority-spin ($u^{\downarrow}$) states, the same (different) m gives a negative (positive) contribution to the $E^{\mathrm{2nd}}_{\mathrm{MA}}$.

In the $CoCp_2$, as pointed in Fig. 4.12 (e), the Jahn-Teller distortion breaks the degeneracy of the doublet $d_{xz,yz}$ in the majority-spin states and introduces small energy gap between the occupied (HOMO) and unoccupied (LUMO) states by $\Delta = 0.404$ eV (see Fig.4.18 (a) for a given Δ). This gives a large positive contribution to the $E^{\mathrm{2nd}}_{\mathrm{MA}}$, 0.91 meV, in which the small energy splitting between the occupied and unoccupied states increases the $E^{\mathrm{2nd}}_{\mathrm{MA}}$ significantly through the denominator of the first term in Eq. (4.6). On the other hand, the SOC between the occupied majority-spin and two unoccupied minority-spin $d_{xz,yz}$ states (the spin-flip SOC term) gives negative contributions through the second term in Eq. (4.8), by -0.473 and -0.311 meV

for the lowest (LUMO+1) and second lowest (LUMO+2) unoccupied minority-spin states, respectively. Here, note that the energy of HOMO state is separated from LUMO+1 and LUMO+2 by $\Delta_1 = 0.776$ and $\Delta_2 = 1.180$ eV, respectively. Further, the SOC with the other occupied d_{z^2}, $d_{x^2-y^2,xy}$ states gives very small contributions to the $E_{\rm MA}^{\rm 2nd}$ compared to that in the $d_{xz,yz}$ states mentioned above, since the energy separation with respect to the unoccupied states is more than 2 eV. Thus, the perpendicular magnetic anisotropy arises mainly from the SOC between the HOMO and LUMO states in the majority-spin $d_{xz,yz}$ states.

In contrast, for the $NiCp_2$ in Fig. 4.18 (b), the HOMO and LUMO states consist of the majority and minority-spin states with the $d_{xz,yz}$ orbital character, and both states separate energetically by 1.097 eV each other. The second-order perturbation theory results in the $E_{\rm MA}^{\rm 2nd}$ of -1.05 meV, which comes from the second term in Eq. (4.8) and thus gives always a negative contribution to the $E_{\rm MA}^{\rm 2nd}$.

The calculations were also performed using the DFT+U framework, in which the $U_{\rm eff}$ determined by the linear response theory were employed. The magnetic anisotropy energies are shown by blue bars in Fig. 4.17. In the $CoCp_2$ and $NiCp_2$, since the energy gaps between the HOMO and LUMO were increased by the correlation effects (+U), as shown in Fig. 4.16 (e) and (f), the denominators in Eqs. (4.6) and (4.8) become greater than that in the GGA, resulting in the small contributions of the SOC interactions from the corresponding orbitals. Thus, the magnitudes of the $E_{\rm MA}$ also become small values. Similar situation is expected in the VCp_2 system. The sign of the $E_{\rm MA}$ in the $CrCp_2$ was flipped from positive (perpendicular magnetization with respect to the Cp rings) to negative (in-plane magnetization) values, and $MnCp_2$ has the $E_{\rm MA}$ of zero due to the spherical symmetric ground state of the ${}^6A_{1g}$ state as well as the $FeCp_2$ case.

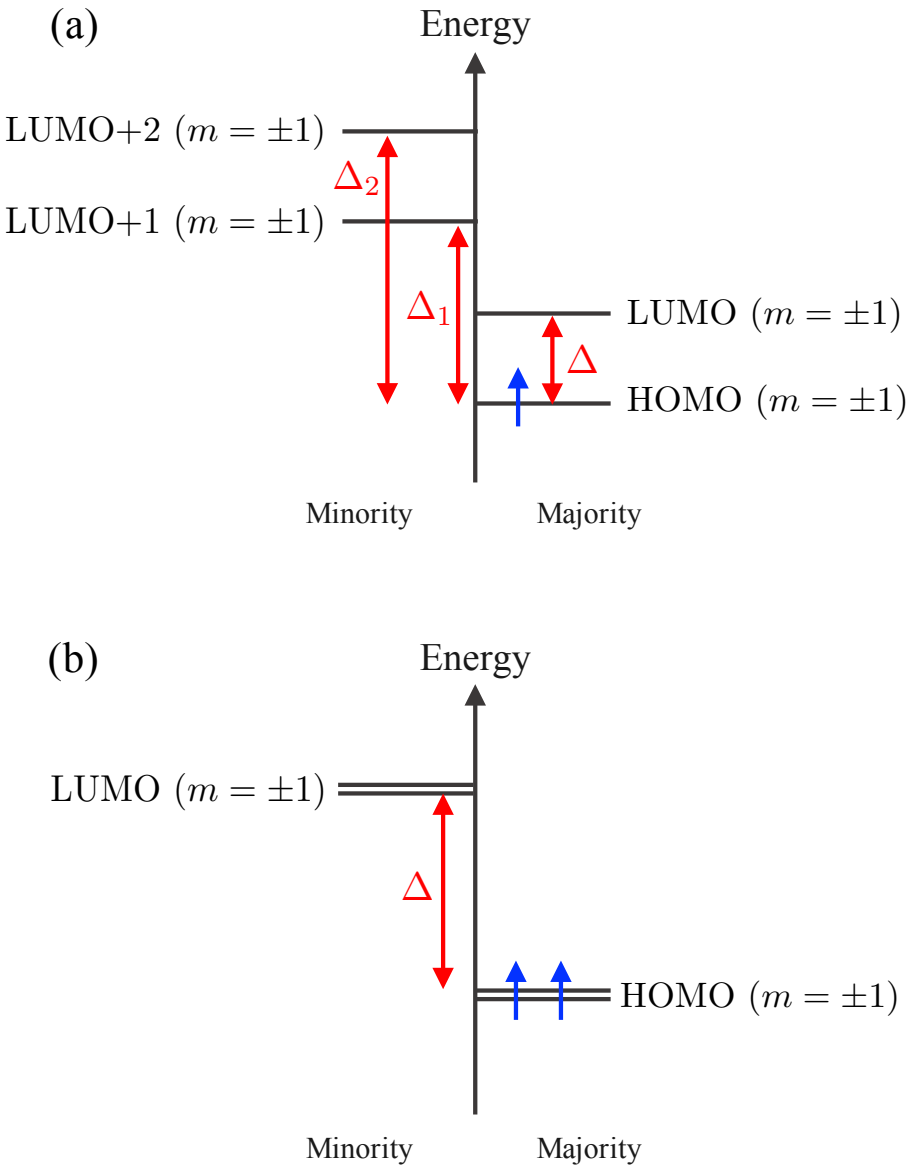

Figure 4.18: Energy diagram around the HOMO and LUMO states for (a) $CoCp_2$ and (b) $NiCp_2$. The m is magnetic quantum number. Blue arrows indicate occupied electrons and Δ shows HOMO-LUMO gap and Δ_i $(i = 1, 2)$ energy gap from HOMO to LUMO+1, LUMO+2, respectively.

4.6 Concluding remarks

In this chapter, an application of developed linear response calculations for estimating the U_{eff} values to organometallic molecule, metallocenes, are presented. Because an additional difficulty intrinsically related to various electron configurations of d electrons that nearly degenerate is raised, calculations using non-empirical +U method combined with the constraint DFT approach were performed to search for the ground-state electronic configuraitons.

As a result, this calculations clarified that ground states are very sensitive to the U_{eff} values and Jahn-Teller splitting. However, predicted ground states are found to be agree with experimental observations: the ground states for $TMCp_2$, in which TM is V, Cr, Mn, Fe, Co, and Ni, are ${}^4A_{2g}$, ${}^3E_{2g}$, ${}^6A_{1g}$, ${}^1A_{1g}$, ${}^2E_{1g}$, and ${}^3A_{2g}$, respectively. These results imply that the utility of combined linear response U_{eff} calculations and the constraint DFT was demonstrated to determine the properties of correlated systems.

Further, the FLAPW calculations were performed to systematical investigation of the magnetism, i.e., magnetic anisotropy. The magnetization of the $CoCp_2$ energetically favors highly orienting along the perpendicular direction to the Cp plane due to the Jahn-Teller splitting in the $d_{xz,yz}$ orbitals, and for the $NiCp_2$ it lies along the parallel direction, where the HOMO and LUMO states are found to play a key role to determine the magnetic anisotropy. The others shows almost no preference for the magnetic easy axis.

Chapter 5

Conclusion

In this thesis, a methodology to obtain the effective on-site Coulomb interaction, $U_{\text{eff}} = U - J$, from the linear response approach has been developed and applied to prototypical correlated materials such as transition-metal monoxides and organometallic metallocene molecules by means of FLAPW calculation method.

In Chapter three, the U_{eff} values for TM atoms in TMO (TMs are Mn, Fe, Co, and Ni) were evaluated from the change in the occupation numbers at the d electrons with respect to an applied constraint field and the variation of the U_{eff} by changing the MT sphere radius was examined. The calculated results show that the obtained U_{eff} decreases as the MT sphere radius increases, in which there is a large variation in the 2$\sim$3 eV. However, an identical band structure in valence state can be reproduced in all systems with approximately scaling of calculated U_{eff}, which are proportional to the occupation numbers of the localized d electrons. These results emphasize that the simple transferability of the U_{eff} among different calculation methods is not accepted to describe the ground state electronic structure that is internally consistent.

In Chapter four, this method was applied to the analysis of ground state electronic structure in organometallic metallocenes, $TMCp_2$, where TM is V, Cr, Mn, Fe, Co, and Ni. In this system, an additional difficulty is raised; various electronic configurations of d electrons are nearly degenerate. In order to search the ground state, a set of the constraint fields were introduced to the d-electron density matrix to calculate the total energies of all electronic configurations allowed by a symmetric group. Since the $FeCp_2$ satisfies the "18-electron rule" describing stable metal complexes, no other stationary solutions of other electronic configurations were

observed in the constraint DFT calculations, resulting in the ground state of $^1A_{1g}$. Even in the VCp_2, $CoCp_2$, and $NiCp_2$, no stationary solutions were found even for large constraint fields; the electronic configurations of $^4A_{2g}$, $^2E_{1g}$, and $^3A_{2g}$ states were predicted as the ground states, respectively. Interestingly, for $MnCp_2$, the low-spin ^2E_2g and high-spin $^6A_{1g}$ states are energetically degenerate at determined U_{eff} of 2.4 eV, while the latter configuration was more stable due to the large exchange-splitting arising from electron correlation (+U). In the $CrCp_2$ the constraint DFT calculations suggested Jahn-Teller effect stabilizes the $^3E_{2g}$ as the ground state, while the other two solutions, corresponding to $^3A_{1g}$ and $^5E_{1g}$ states, were obtained. The predicted ground state electronic configurations were consistent with experimental studies while the stability between different electronic configurations is found to be very sensitive to U_{eff} values.

In this dissertation, non-empirical methodology for obtaining the U_{eff} and the systematical investigations of U_{eff}, MT sphere radius, and electronic configurations have been studied by means of first-principles FLAPW method. In conclusion, it is important to emphasize that by using the methodology that is proposed in this dissertation opens a new avenue toward reliable prediction of structures and physical properties in strongly correlated systems and gives suggestions for future calculations.

Bibliography

[1] P. Hohenberg and W. Kohn. *Phys. Rev.*, **136**, B864 (1964).

[2] W. Kohn and L. J. Sham. *Phys. Rev.*, **140**, A1133 (1965).

[3] W. Kohn. *Rev. Mod. Phys.*, **71**, 1253 (1999).

[4] A. E. Mattsson. *Science*, **298**, 759 (2002).

[5] M. Imada, A. Fujimori, and Y. Tokura. *Rev. Mod. Phys.*, **70**, 1039 (1998).

[6] H. Wich. *"N. F. Mott. Metal-insulator transitions"*. Taylor & Francis Ltd., London (1974).

[7] W. L. Roth. *Phys. Rev.*, **110**, 1333 (1958).

[8] P. W. Anderson. *Phys. Rev.*, **79**, 350 (1950).

[9] W. A. Philip. *Solid State Physics*, **14**, 99 (1963).

[10] A. S. Glen. *J. Appl. Phys.*, **31**, 1571 (1960).

[11] A. K. Cheetham and D. A. O. Hope. *Phys. Rev. B*, **27**, 6964 (1983).

[12] H. Shaked, J. Faber, and R. L. Hitterman. *Phys. Rev. B*, **38**, 11901 (1988).

[13] D. Herrmann-Ronzaud, P. Burlet, and J. Rossat-Mignod. *J. Physics C: Solid State Physics*, **11**, 2123 (1978).

[14] W. Jauch, M. Reehuis, H. J. Bleif, F. Kubanek, and P. Pattison. *Phys. Rev. B*, **64**, 052102 (2001).

[15] H. Fjellvåg, B. C. Hauback, T. Vogt, and S. Stølen. **87**, 347 (2002).

[16] F. Helmer, G. Fredrik, S. Svein, and H. Bjørn. *J. Solid State Chem.*, **124**, 52 (1996).

[17] W. L. Roth. *Phys. Rev.*, **111**, 772 (1958).

[18] J. Baruchel, M. Schlenker, K. Kurosawa, and S. Saito. *Philosophical Magazine Part B*, **43**, 853 (1981).

[19] R. Eric, K. Nolwenn, P. R. Louis, and Y. H. Jean. *Physica B: Condensed Matter*, **385**, 394 (2006).

[20] A. L. Goodwin, M. G. Tucker, M. T. Dove, and D. A. Keen. *Phys. Rev. Lett.*, **96**, 047209 (2006).

[21] F. Tran, P. Blaha, K. Schwarz, and P. Novák. *Phys. Rev. B*, **74**, 155108 (2006).

[22] S. Fabris, S. de Gironcoli, S. Baroni, G. Vicario, and G. Balducci. *Phys. Rev. B*, **71**, 041102 (2005).

[23] S. Fabris, G. Vicario, G. Balducci, S. de Gironcoli, and S. Baroni. *J. Phys. Chem. B*, **109**, 22860 (2005).

[24] C. Di Valentin, G. Pacchioni, and A. Selloni. *J. Phys. Chem. C*, **113**, 20543 (2009).

[25] F. Emanuele, D. V. Cristiana, P. Gianfranco, and S. Annabella. *J. Chem. Phys.*, **129**, 154133 (2008).

[26] G. Mattioli, P. Alippi, F. Filippone, R. Caminiti, and B. A. Amor. *J. Phys. Chem. C*, **114**, 21694 (2010).

[27] M. C. Gutzwiller. *Phys. Rev. Lett.*, **10**, 159 (1963).

[28] J. Kanamori. *Prog. Theor. Phys.*, **30**, 275 (1963).

[29] J. Hubbard. *Proc. Roy. Soc. A*, **276**, 238 (1963).

[30] J. Hubbard. *Proc. Roy. Soc. A*, **277**, 237 (1964).

[31] J. Hubbard. *Proc. Roy. Soc. A*, **281**, 401 (1964).

[32] J. Hubbard. *Proc. Roy. Soc. A*, **285**, 542 (1965).

[33] J. Hubbard. *Proc. Roy. Soc. A*, **296**, 82 (1967).

[34] J. Hubbard. *Proc. Roy. Soc. A*, **296**, 100 (1967).

[35] V. I. Anisimov and O. Gunnarsson. *Phys. Rev. B*, **43**, 7570 (1991).

[36] V. I. Anisimov, J. Zaanen, and O. K. Andersen. *Phys. Rev. B*, **44**, 943 (1991).

[37] V. I. Anisimov, I. V. Solovyev, M. A. Korotin, M. T. Czyżyk, and G. A. Sawatzky. *Phys. Rev. B*, **48**, 16929 (1993).

[38] I. V. Solovyev, P. H. Dederichs, and V. I. Anisimov. *Phys. Rev. B*, **50**, 16861 (1994).

[39] V. I. Anisimov, F. Aryasetiawan, and A. I. Lichtenstein. *J. Phys.: Condens. Matter*, **9**, 767 (1997).

[40] J. P. Perdew, R. G. Parr, M. Levy, and J. L. Balduz. *Phys. Rev. Lett.*, **49**, 1691 (1982).

[41] J. P. Perdew and M. Levy. *Phys. Rev. Lett.*, **51**, 1884 (1983).

[42] L. J. Sham and M. Schlüter. *Phys. Rev. Lett.*, **51**, 1888 (1983).

[43] O. Gunnarsson and K. Schönhammer. *Phys. Rev. Lett.*, **56**, 1968 (1986).

[44] R. W. Godby, M. Schlüter, and L. J. Sham. *Phys. Rev. Lett.*, **56**, 2415 (1986).

[45] L. J. Sham and M. Schlüter. *Phys. Rev. Lett.*, **60**, 1582 (1988).

[46] A. J. Cohen, P. Mori-Sánchez, and W. Yang. *Science*, **321**, 792 (2008).

[47] M. Grüning, A. Marini, and A. Rubio. *J. Chem. Phys.*, **124**, 154108 (2006).

[48] P. Mori-Sánchez, A. J. Cohen, and W. Yang. *Phys. Rev. Lett.*, **100**, 146401 (2008).

[49] S. Lany and A. Zunger. *Phys. Rev. B*, **78**, 235104 (2008).

[50] K. Capelle, G. Vignale, and C. A. Ullrich. *Phys. Rev. B*, **81**, 125114 (2010).

[51] F. E. Zahariev and Y. A. Wang. *Phys. Rev. A*, **70**, 042503 (2004).

[52] A. Savin, F. Colonna, and R. Pollet. *Int. J. Quantum Chem.*, **93**, 166 (2003).

[53] E. Sagvolden and J. P. Perdew. *Phys. Rev. A*, **77**, 012517 (2008).

[54] E. Sagvolden, J. P. Perdew, and M. Levy. *Phys. Rev. A*, **79**, 026501 (2009).

[55] Y. Weitao, J. C. Aron, and M. Paula. *J. Chem. Phys.*, **136**, 204111 (2012).

[56] M. D. Reiner and K. U. G. Eberhard. *"Density functional theory: An approach to the Quantum Many-Body problem"*. Springer-Verlag, New York, Berlin Heidelberg (1990).

[57] S. Kümmel and L. Kronik. *Rev. Mod. Phys.*, **80**, 3 (2008).

[58] L. Kronik, T. Stein, S. Refaely-Abramson, and R. Baer. *J. Chem. Theor, Comp.*, **8**, 1515 (2012).

[59] G. K.-L. Chan. *J. Chem. Phys.*, **110**, 4710 (1999).

[60] M. J. Allen and D. J. Tozer. *Mol. Phys.*, **100**, 433 (2002).

[61] J. F. Janak. *Phys. Rev. B*, **18**, 7165 (1978).

[62] M. Levy, J. P. Perdew, and V. Sahni. *Phys. Rev. A*, **30**, 2745 (1984).

[63] C.-O. Almbladh and U. von Barth. *Phys. Rev. B*, **31**, 3231 (1985).

[64] J. P. Perdew and M. Levy. *Phys. Rev. B*, **56**, 16021 (1997).

[65] V. I. Anisimov, F. Aryasetiawan, and A. I. Lichtenstein. *J. Phys. Condens. Matter*, **9**, 767 (1997).

[66] P. W. Anderson. *Phys. Rev.*, **124**, 41 (1961).

[67] A. I. Liechtenstein, V. I. Anisimov, and J. Zaanen. *Phys. Rev. B*, **52**, R5467 (1995).

[68] I. Yang, S. Y. Savrasov, and G. Kotliar. *Phys. Rev. Lett.*, **87**, 216405 (2001).

[69] C. S. Wang and J. Callaway. *Phys. Rev. B*, **9**, 4897 (1974).

[70] F. Weling and J. Callaway. *Phys. Rev. B*, **26**, 710 (1982).

[71] G. Radaelli, D. Petti, E. Plekhanov, I. Fina, P. Torelli, B. R. Salles, M. Cantoni, C. Rinaldi, D. Gutiérrez, G. Panaccione, M. Varela, S. Picozzi, J. Fontcuberta, and R. Bertacco. *Nat. Commun.*, **5**, 3404 (2014).

[72] M. E. Arroyo-de Dompablo, A. Morales-García, and M. Taravillo. *J. Chem. Phys.*, **135**, 054503 (2011).

[73] A. Abbad, H. A. Bentounes, W. Benstaalib, S. Bentata, and B. Bouadjemi. *Chalcog. Lett.*, **12**, 301 (2015).

[74] K. Nawa, Y. Kitaoka, K. Nakamura, H. Imamura, T. Akiyama, T. Ito, and M. Weinert. *Phys. Rev. B*, **94**, 035136 (2016).

[75] F. Filippone, G. Mattioli, P. Alippi, and A. A. Bonapasta. *Phys. Rev. Lett.*, **107**, 196401 (2011).

[76] M. Annapaola, M. N. Konstantin, I. Francesc, and T. B. Stefan. *J. Chem. Phys.*, **131**, 064701 (2009).

[77] D. W. Boukhvalov, V. V. Dobrovitski, M. I. Katsnelson, A. I. Lichtenstein, B. N. Harmon, and P. Kögerler. *Phys. Rev. B*, **70**, 054417 (2004).

[78] U. del Pennino, V. Corradini, R. Biagi, V. De Renzi, F. Moro, D. W. Boukhvalov, G. Panaccione, M. Hochstrasser, C. Carbone, C. J. Milios, and E. K. Brechin. *Phys. Rev. B*, **77**, 085419 (2008).

[79] C. D. Pemmaraju, I. Rungger, and S. Sanvito. *Phys. Rev. B*, **80**, 104422 (2009).

[80] A. K. Pathak, D. Paudyal, Y. Mudryk, K. A. Gschneidner, and V. K. Pecharsky. *Phys. Rev. Lett.*, **110**, 186405 (2013).

[81] A. B. Shick and O. N. Mryasov. *Phys. Rev. B*, **67**, 172407 (2003).

[82] T. O. Wehling, A. I. Lichtenstein, and M. I. Katsnelson. *Phys. Rev. B*, **84**, 235110 (2011).

[83] J. Zaanen and G. A. Sawatzky. *J. Solid State Chem.*, **88**, 8 (1990).

[84] E. Şaşıoğlu, C. Friedrich, and S. Blügel. *Phys. Rev. Lett.*, **109**, 146401 (2012).

[85] C. Loschen, J. Carrasco, K. M. Neyman, and F. Illas. *Phys. Rev. B*, **75**, 035115 (2007).

[86] W. E. Pickett, S. C. Erwin, and E. C. Ethridge. *Phys. Rev. B*, **58**, 1201 (1998).

[87] L. Wang, T. Maxisch, and G. Ceder. *Phys. Rev. B*, **73**, 195107 (2006).

[88] A. Jain, G. Hautier, S. P. Ong, C. J. Moore, C. C. Fischer, K. A. Persson, and G. Ceder. *Phys. Rev. B*, **84**, 045115 (2011).

[89] B.-C. Shih, T. A. Abtew, X. Yuan, W. Zhang, and P. Zhang. *Phys. Rev. B*, **86**, 165124 (2012).

[90] M. Cococcioni and S. de Gironcoli. *Phys. Rev. B*, **71**, 035105 (2005).

[91] A. Floris, S. de Gironcoli, E. K. U. Gross, and M. Cococcioni. *Phys. Rev. B*, **84**, 161102 (2011).

[92] E. R. Ylvisaker, W. E. Pickett, and K. Koepernik. *Phys. Rev. B*, **79**, 035103 (2009).

[93] N. J. Mosey, P. Liao, and E. A. Carter. *J. Chem. Phys.*, **129**, 014103 (2008).

[94] E. Schrödinger. *Ann. Phys.*, **79**, 361 (1926).

[95] M. Born and R. Oppenheimer. *Ann. Phys.*, **84**, 457 (1927).

[96] L. H. Thomas. *Mat. Proc. Camb. Philos. Soc.*, **23**, 542 (1927).

[97] E. Fermi. *Rend. Accad. Naz. Lincei*, **6**, 602 (1927).

[98] L. Hedin and B. I. Lundqvist. *J. Phys. C: Solid State Phys.*, **4**, 2064 (1971).

[99] U. von Barth and L. Hedin. *J. Phys. C: Solod State Phys.*, **5**, 1629 (1972).

[100] O. Gunnarsson and B. I. Lundqvist. *Phys. Rev. B*, **13**, 4274 (1976).

[101] A. D. Becke. *Phys. Rev. A*, **38**, 3098 (1988).

[102] J. P. Perdew, J. A. Chevary, S. H. Vosko, K. A. Jackson, M. R. Pederson, D. J. Singh, and C. Fiolhais. *Phys. Rev. B*, **46**, 6671 (1992).

[103] J. P. Perdew, K. Burke, and M. Ernzerhof. *Phys. Rev. Lett.*, **77**, 3865 (1996).

[104] P. W. Atkins. *"Molecular Quantum Mechanics"*. Oxford University Press, United Kingdom (1983).

[105] J. C. Slater. *Phys. Rev.*, **51**, 846 (1937).

[106] P. D. DeCicco. *Phys. Rev.*, **153**, 931 (1967).

[107] N. Elyashar and D. D. Koelling. *Phys. Rev. B*, **13**, 5362 (1976).

[108] H. Bross. *Phys. Kondens. Matter.*, **3**, 119 (1964).

[109] H. Bross, G. Bohn, G. Meister, W. Schubö, and H. Stöhr. *Phys. Rev. B*, **2**, 3098 (1970).

[110] D. D. Koelling. *Phys. Rev. B*, **2**, 290 (1970).

[111] P. M. Marcus. *Int. J. Quantum Chem.*, **1**, 567 (1967).

[112] O. K. Andersen. *Phys. Rev. B*, **12**, 3060 (1975).

[113] D. D. Koelling and G. O. Arbram. *J. Phys. F: Met. Phys.*, **5**, 2041 (1975).

[114] J. D. Jackson. *"Classical electrodynamics"*. Wiley, New York, 3rd edition (1999).

[115] M. Weinert. *J. Math. Phys.*, **22**, 2433 (1981).

[116] H. Krakauer, M. Posternak, and A. J. Freeman. *Phys. Rev. B*, **19**, 1706 (1979).

[117] E. Wimmer, H. Krakauer, M. Weinert, and A. J. Freeman. *Phys. Rev. B*, **24**, 864 (1981).

[118] M. Weinert, E. Wimmer, and A. J. Freeman. *Phys. Rev. B*, **26**, 4571 (1982).

[119] D. M. Brink and G. R. Satchler. *"Angular Momentum"*. Clarendon, Oxford, 3rd edition (1968).

[120] D. J. Singh and L. Nordstrom. *"Planewaves, Pseudopotentials and the LAPW Method"*. Springer, USA, 3rd edition (2006).

[121] M. Posternak, H. Krakauer, A. J. Freeman, and D. D. Koelling. *Phys. Rev. B*, **21**, 5601 (1980).

[122] O. Bengone, M. Alouani, P. Blöchl, and J. Hugel. *Phys. Rev. B*, **62**, 16392 (2000).

[123] F. Zhou, M. Cococcioni, C. A. Marianetti, D. Morgan, and G. Ceder. *Phys. Rev. B*, **70**, 235121 (2004).

[124] H. Eschrig, K. Koepernik, and I. Chaplygin. *J. Solid State Chem.*, **176**, 482 (2003).

[125] M. J. Han, T. Ozaki, and J. Yu. *Phys. Rev. B*, **73**, 045110 (2006).

[126] A. B. Shick, A. I. Liechtenstein, and W. E. Pickett. *Phys. Rev. B*, **60**, 10763 (1999).

[127] S. Chandra and H. C. Verma. *Phys. Rev. B*, **34**, 1293 (1986).

[128] C. Herring. *Phys. Rev.*, **57**, 1169 (1940).

[129] C. Herring and A. G. Hill. *Phys. Rev.*, **58**, 132 (1940).

[130] S. L. Dudarev, G. A. Botton, S. Y. Savrasov, C. J. Humphreys, and A. P. Sutton. *Phys. Rev. B*, **57**, 1505 (1998).

[131] J. P. Perdew and A. Zunger. *Phys. Rev. B*, **23**, 5048 (1981).

[132] R. Peters and N. Kawakami. *Phys. Rev. B*, **86**, 165107 (2012).

[133] T. Miyake, F. Aryasetiawan, and M. Imada. *Phys. Rev. B*, **80**, 155134 (2009).

[134] E. Şaşıoğlu, C. Friedrich, and S. Blügel. *Phys. Rev. B*, **83**, 121101 (2011).

[135] B. Himmetoglu, A. Floris, S. de Gironcoli, and M. Cococcioni. *Int. J. Quantum Chem.*, **114**, 14 (2014).

[136] M. Cococcioni. "*A LDA+U study of selected iron compounds*". Ph.D Thesis, Insititutional Research Information System, Scuola Internazionale Superiore di Studi Avanzati, Italy (2002).

[137] K. Nakamura, Y. Kitaoka, T. Akiyama, T. Ito, M. Weinert, and A. J. Freeman. *Phys. Rev. B*, **85**, 235129 (2012).

[138] Y. Kitaoka, K. Nakamura, T. Akiyama, T. Ito, M. Weinert, and A. J. Freeman. *Phys. Rev. B*, **87**, 205113 (2013).

[139] K. Nawa, Y. Kitaoka, K. Nakamura, T. Akiyama, and T. Ito. *J. Appl. Phys.*, **117**, 17E171 (2015).

[140] P. Güttinger. *Z. Phys.*, **73**, 169 (1932).

[141] R. P. Feynman. *Phys. Rev.*, **56**, 340 (1939).

[142] D. D. Koelling and B. N. Harmon. *J. Phys. C: Solid State Phys.*, **10**, 3107 (1977).

[143] C. A. McCammon and L.-G. Liu. *Phys. Chem. Miner.*, **10**, 106 (1984).

[144] L. F. Mattheiss. *Phys. Rev. B*, **5**, 290 (1972).

[145] R. Kannan and M. S. Seehra. *Phys. Rev. B*, **35**, 6947 (1987).

[146] S. L. Dudarev, A. I. Liechtenstein, M. R. Castell, G. A. D. Briggs, and A. P. Sutton. *Phys. Rev. B*, **56**, 4900 (1997).

[147] A. Aviram and M. A. Ratner. *Chem. Phys. Lett.*, **29**, 277 (1974).

[148] G. A. Prinz. *Science*, **282**, 1660 (1998).

[149] S. A. Wolf, D. D. Awschalom, R. A. Buhrman, J. M. Daughton, S. von Molnár, M. L. Roukes, A. Y. Chtchelkanova, and D. M. Treger. *Science*, **294**, 1488 (2001).

[150] C. Felser, G. H. Fecher, and B. Balke. *Angew. Chem. Int. Ed.*, **46**, 668 (2007).

[151] J. Jortner and J. M. Ratner. *"Molecular Electronics"*. Blackwell Science, Makden, MA (1997).

[152] J. M. Tour. *Acc. Chem. Res.*, **33**, 791 (2000).

[153] C. P. Collier, E. W. Wong, M. Belohradský, F. M. Raymo, J. F. Stoddart, P. J. Kuekes, R. S. Williams, and J. R. Heath. *Science*, **285**, 391 (1999).

[154] J. Camarero and E. Coronado. *J. Mater. Chem.*, **19**, 1678 (2009).

[155] V. V. Maslyuk, A. Bagrets, V. Meded, A. Arnold, F. Evers, M. Brandbyge, T. Bredow, and I. Mertig. *Phys. Rev. Lett.*, **97**, 097201 (2006).

[156] C. Morari, H. Allmaier, F. Beiuşeanu, T. Jurcuţ, and L. Chioncel. *Phys. Rev. B*, **85**, 085413 (2012).

[157] M. Wu and X. C. Zeng. *Appl. Phys. Lett.*, **99**, 053121 (2011).

[158] Y. Li, Z. Zhou, and Z. Chen. *J. Phys. Chem. A*, **116**, 1648 (2012).

[159] N. Hoshino, F. Iijima, G. N. Newton, N. Yoshida, T. Shiga, H. Nojiri, A. Nakao, R. Kumai, Y. Murakami, and H. Oshio. *Nat. Chem.*, **4**, 921 (2012).

[160] T. J. Kealy and P. L. Pauson. *Nature*, **168**, 1039 (1951).

[161] S. A. Miller, J. A. Tebboth, and J. F. Tremaine. *J. Chem. Soc.*, , 632 (1952).

[162] G. Wilkinson, M. Rosenblum, M. C. Whiting, and R. B. Woodward. *J. Am. Chem. Soc.*, **74**, 2125 (1952).

[163] E. O. Fischer and W. Pfab. *Z. Natur.*, **7b**, 377 (1952).

[164] C. Engtrakul and L. R. Sita. *Nano Letters*, **1**, 541 (2001).

[165] R. Liu, S.-H. Ke, H. U. Baranger, and W. Yang. *Nano Letters*, **5**, 1959 (2005).

[166] Y. Ma, Y. Dai, W. Wei, and B. Huang. *J. Mater. Chem. C*, **1**, 941 (2013).

[167] N. L. Long. *"Metallocenes: An Introduction to Sandwich Complexes"*. Blackwell Scinence, London (1988).

[168] S. Evans, M. L. H. Green, B. Jewitt, A. F. Orchard, and C. F. Pygall. *J. Chem. Soc., Faraday Trans. II*, **68**, 1847 (1972).

[169] S. Evans, M. L. H. Green, B. Jewitt, G. H. King, and A. F. Orchard. *J. Chem. Soc., Faraday Trans. II*, **70**, 356 (1974).

[170] M. F. Rettig and R. S. Drago. *J. Am. Chem. Soc.*, **91**, 1361 (1969).

[171] K. R. Gordon and K. D. Warren. *Inorg. Chem.*, **17**, 987 (1978).

[172] Y. Ma, Y. Dai, W. Wei, and B. Huang. *J. Mater. Chem. C*, **1**, 941 (2013).

[173] Z.-F. Xu, Y. Xie, W.-L. Feng, and H. F. Schaefer. *J. Phys. Chem. A*, **107**, 2716 (2003).

[174] J. C. Giordan, J. H. Moore, J. A. Tossell, and J. Weber. *J. Am. Chem. Soc.*, **105**, 3431 (1983).

[175] A. Stebler, A. Furrer, and J. H. Ammeter. *Inorg. Chem.*, **23**, 3439 (1984).

[176] I. Langmuir. *Science*, **54**, 59 (1921).

[177] D.-S. Wang, R. Wu, and A. J. Freeman. *Phys. Rev. B*, **47**, 14932 (1993).

List of Publications

1. Kenji Nawa, Yukie Kitaoka, Kohji Nakamura, Toru Akiyama, and Tomonori Ito
   'Electronic Configurations and Magnetic Anisotropy in Organometallic Metallocenes'
   Journal of Applied Physics, **117**, 17E131 (2015).

2. Kenji Nawa, Yukie Kitaoka, Kohji Nakamura, Hiroshi Imamura, Toru Akiyama, Tomonori Ito, and Michael Weinert
   'Search for the ground state electronic configurations of correlated organometallic metallocenes from constraint density functional theory'
   Physical Review B, **94**, 035136 (2016).

3. Kento Yamamoto, Abdul-Muizz Pradipto, Kenji Nawa, Toru Akiyama, Tomonori Ito, Teruo Ono, and Kohji Nakamura
   'Interfacial Dzyaloshinskii-Moriya interaction and orbital magnetic moments of metallic multilayer films'
   AIP Advances, **7**, 056302 (2017).

4. Kohji Nakamura, Takahiro Nomura, Abdul-Muizz Pradipto, Kenji Nawa, Toru Akiyama, and Tomonori Ito
   'Effect of heavy-metal insertions at Fe/MgO interfaces on electric-field-induced modification of magnetocrystalline anisotropy'
   Journal of Magnetism and Magnetic Materials, **429**, 214 (2017).

5. Kenji Nawa, Toru Akiyama, Tomonori Ito, Kohji Nakamura, Tamio Oguchi, and Michael Weinert
   'Scaled effective on-site Coulomb interaction in density functional theory +U method for correlated materials'
   Physical Review B (submitted).

List of Presentations

International Conferences and Seminars

1. ◯Kenji Nawa, Yukie Kitaoka, Kohji Nakamura, Toru Akiyama, Tomonori Ito:
"Electronic configuration of d-electrons in metallocenes from constraint density functional theory"
The 3rd international Symposium for Sustainability by Engineering at MIU, 11, Tsu, Japan, November 2013.

2. ◯Kenji Nawa, Yukie Kitaoka, Kohji Nakamura, Toru Akiyama, Tomonori Ito:
"Electronic configurations and magnetic anisotropy in organometallic metallocenes"
59th Annual Magnetism and Magnetic Materials Conference, CQ-09, Honolulu, United States of America, November 2014.

3. ◯Yushi Ikeura, Kenji Nawa, Kohji Nakamura, Toru Akiyama, Tomonori Ito:
"Magnetocrystalline anisotropy of rare-earth ultra-thin films"
Symposium on Nanoscience and Nanotechnology: DIVISION E, 21, Tsu, Japan, November 2014.

4. ◯Shohei Takeda, Kenji Nawa, Kohji Nakamura, Kazuhiro Sano, Toru Akiyama, Tomonori Ito:
"Valley band structures of WSe_2 thin films in external electric field"
Symposium on Nanoscience and Nanotechnology: DIVISION E, 24, Tsu, Japan, November 2014.

5. ◯Kenji Nawa, Kohji Nakamura, Toru Akiyama, Tomonori Ito, Tamio Oguchi:
"Magnetic anisotropy in organometallic molecules"
The 18th SANKEN International and The 13th SANKEN Nanotechnology Symposium, AP60, Umeda, Japan, December 2014.

6. ◯Kenji Nawa, Kohji Nakamura, Toru Akiyama, Tomonori Ito, Michael Weinert:
"Electron configuration and correlation effects in organometallic molecules from constraint density functional theory"
APS March Meeting 2015, H01-119, San Antonio, United States of America, March 2015.

7. ◯Yushi Ikeura, Kenji Nawa, Kohji Nakamura, Toru Akiyama, Tomonori Ito:
"Electronic structures and magnetocrystalline anisotropy of rare-earth ultra-thin films"
Joint International Conference on Electronic Properties of Two-Dimensional Systems and Modulated Semiconductor Structures (EP2DS-21/MSS-17), Tu-PM-20, Sendai, Japan, July 2015.

8. ◯Shohei Takeda, Kenji Nawa, Kohji Nakamura, Kazuhiro Sano, Toru Akiyama, Tomonori Ito:
"Tuning of Spin-Valley Band Structures in WSe_2 Thin Films by External Fields"
Joint International Conference on Electronic Properties of Two-Dimensional Systems and Modulated Semiconductor Structures (EP2DS-21/MSS-17), Mo-PE-78, Sendai, Japan, July 2015.

9. ◯Kenji Nawa:
"Effective on-site Coulomb interaction and electron configurations in transition-metal complexes: A revisit from constraint DFT"
Condensed Matter Theory Group Seminar, University of York, York, United Kingdom, November 2015.

10. ◯Yushi Ikeura, Kenji Nawa, Kohji Nakamura, Toru Akiyama, Tomonori Ito:
"Magnetocrystalline anisotropy in rare-earth metal monolayers"
The 18th Asian Workshop on First-Principles Electronic Structure Calculations, 54, Kashiwa, Japan, November 2015.

11. ◯Shohei Takeda, Kenji Nawa, Kohji Nakamura, Kazuhiro Sano, Toru Akiyama, Tomonori Ito:
"Spin-polarized carrier tuning in transition metal dichalogenides by electric and magnetic fields"
The 18th Asian Workshop on First-Principles Electronic Structure Calculations, 44, Kashiwa, Japan, November 2015.

12. ◯Takahiro Ito, Kenji Nawa, Kohji Nakamura, Toru Akiyama, Tomonori Ito, Teruo Ono:
"Spin Hall conductivity in Pt-based superlattice structures"
The 18th Asian Workshop on First-Principles Electronic Structure Calculations, 58, Kashiwa, Japan, November 2015.

13. ◯Kento Yamamoto, Kenji Nawa, Kohji Nakamura, Toru Akiyama, Tomonori Ito Teruo Ono:
"Role of interface structures in magnetocrystalline anisotropy of Co/Pt(111) thin films"
The 18th Asian Workshop on First-Principles Electronic Structure Calculations, 52, Kashiwa, Japan, November 2015.

14. ◯Shohei Takeda, Kenji Nawa, Kohji Nakamura, Kazuhiro Sano, Toru Akiyama, Tomonori Ito:
"Spin-polarized carriers of transition metal dichalcogenides tuned by electric and magnetic fields"
Symposium on Nanotechnology and Nanoscience (Division E), 27, Mie University, Tsu, Japan, November 2015.

15. ◯Takahiro Ito, Kenji Nawa, Kohji Nakamura, Toru Akiyama, Tomonori Ito:
"Intrinsic spin Hall conductivity in Pt-based noble metal superlattices: first principles study"
Symposium on Nanotechnology and Nanoscience (Division E), 28, Mie University, Tsu, Japan, November 2015.

16. ◯Kento Yamamoto, Kenji Nawa, Kohji Nakamura, Toru Akiyama, Tomonori Ito:
"Magnetocrystalline anisotropy of Co/Pt(111) thin films: role of interface structures"
Symposium on Nanotechnology and Nanoscience (Division E), 31, Mie University, Tsu, Japan, November 2015.

17. ◯Kenji Nawa, Yushi Ikeura, Kohji Nakamura, Toru Akiyama, Tomonori Ito, Tamio Oguchi, Michael Weinert:
"Magnetocrystalline anisotropy in rare-earth metal ultra-thin films"
2016 Joint MMM-Intermag Conference, HI-15, San Diego, United States of America, January 2016.

18. ◯Kenji Nawa, Kohji Nakamura, Toru Akiyama, Tomonori Ito, Michael Weinert:
"Effective on-site Coulomb interaction and electron configurations in transition-metal complexes from constraint density functional theory"
APS March Meeting 2016, B20.015, Baltimore, United States of America, March 2016.

19. ◯Takahiro Ito, Kenji Nawa, Kohji Nakamura, Toru Akiyama, Tomonori Ito, Teruo Ono:
"Role of atomic-layer alignment in intrinsic spin Hall conductivity of Pt-based superlattices"

The 18th International Conference on Crystal Growth and Epitaxy, ThP-T05-5, Nagoya, Japan, August 2016.

20. ◯Kento Yamamoto, Kenji Nawa, Kohji Nakamura, Toru Akiyama, Tomonori Ito, Teruo Ono:
"Dzyaloshinskii-Moriya interaction at metallic bilayer interfaces"
The 18th International Conference on Crystal Growth and Epitaxy, ThP-T05-3, Nagoya, Japan, August 2016.

21. ◯Kenji Nawa, Toru Akiyama, Tomonori Ito, Kohji Nakamura:
"Electronic structures and magnetism in 5*d* transition-metal phthalocyanines"
6th Spin-Polarized Scanning Tunneling Microscopy International Conference, Chiba, Japan, August 2016.

22. Kohji Nakamura, ◯Kenji Nawa:
"Role of spin-orbit coupling in electric field effect on magnetocrystalline anisotropy of metal thin films"
The 2nd ImPACT International Symposium on Spintronics Memory, Circuit and Storage, 35, Tsukuba, Japan, September 2016.

23. ◯Kenji Nawa, Toru Akiyama, Tomonori Ito, Tamio Oguchi, Michael Weinert, Kohji Nakamura:
"Interfacial magnetic anisotropy in rare-earth metal ultra-thin films"
61th Annual Conference on Magnetism and Magnetic Materials, AI-05, New Orleans, United States of America, October–November 2016.

24. ◯Takahiro Ito, Kenji Nawa, Abdul-Muizz Tri Pradipto, Toru Akiyama, Tomonori Ito, Teruo Ono, Kohji Nakamura:
"Role of atomic-layer alignments to intrinsic spin Hall conductivity in Pt-based superlattices film"
61th Annual Conference on Magnetism and Magnetic Materials, CR-08, New Orleans, United States of America, October–November 2016.

25. ◯Kento Yamamoto, Kenji Nawa, Abdul-Muizz Tri Pradipto, Toru Akiyama, Tomonori Ito, Teruo Ono, Kohji Nakamura:
"Interfacial Dzyaloshinskii-Moriya interaction and orbital magnetic moments of metallic multilayer films"
61th Annual Conference on Magnetism and Magnetic Materials, FR-04, New Orleans, United States of America, October–November 2016.

26. ◯Kohei Nozaki, Kenji Nawa, Abdul-Muizz Tri Pradipto, Toru Akiyama, Tomonori Ito, Kohji Nakamura:
"Atomic-layer alignment tuning for magnetism in Au-Fe multilayer thin-film on MgO(001)"
Symposium on Nanotechnology and Nanoscience (Division E), 09, Tsu, Japan, November 2016.

27. ◯Takahiro Nomura, Kenji Nawa, Abdul-Muizz Tri Pradipto, Toru Akiyama, Tomonori Ito, Kohji Nakamura:
"Systematic investigation of magnetocrystalline anisotropy in 3*d*, 4*d*, and 5*d* transition-metal thin-films"
Symposium on Nanotechnology and Nanoscience (Division E), 10, Tsu, Japan, November 2016.

28. ◯Kenji Nawa, Kohji Nakamura:
"First principles calculations for effective on-site Coulomb interaction in transition metal

oxides and rare-earth metals"
Colloquium 2016, Oguhi Laboratory, ISIR, Osaka University, Suita, Japan, December 2016 (Seminar).

29. Arsham Ghasemi, Demie Kepaptsoglou, Kenji Nawa, Susannah Speller, Pedro Galindo, Quentin Ramasse, Kohji Nakamura, Thorsten Hesjedal, Vlado Lazarov:
"Van der Waals interfaces: TI/superconductor and semiconductor"
Psi-k workshop on Atomic scale materials microscopy: theory meets experiment, C7, York, United Kingdom, June 2017.

30. Keisuke Mobayashi, Kenji Nawa, Abdul-Muizz Tri Pradipto, Toru Akiyama, Tomonori Ito, Tamio Oguchi, Kohji Nakamura:
"On-site Coulomb interaction of transition-metal monoxide thin films from linear response theory"
Junjiro Kanamori Memorial International Symposium –New Horizon of Magnetism–, P88, Hongo, Japan, September 2017.

31. ◯Kenji Nawa, Toru Akiyama, Tomonori Ito, Tamio Oguchi, Michael Weinert, Kohji Nakamura:
"Electronic structures and magnetism in organometallic molecules of $3d$, $4d$, and $5d$ transition-metal phthalocyanines"
Psi-k CECAM Resarch Conference AB-INITIO SPIN-ORBITRONICS, P-12, Montesilvano, Italy, September 2017.

Domestic Conferences, Meetings, and Seminars

1. ◯名和憲嗣, 北岡幸恵, 中村浩次, 秋山亨, 伊藤智徳:
" 遷移金属メタロセン分子の多重項構造の第一原理計算"
三重大学-大阪大学ジョイント研究会「第一理計算による物質設計」, 津, 2013 年 9 月.

2. ◯名和憲嗣, 北岡幸恵, 中村浩次, 秋山亨, 伊藤智徳:
" 遷移金属メタロセン分子の多重項構造の第一原理計算"
日本物理学会 2013 年秋季大会, 27pPSA-42, 徳島, 2013 年 9 月.

3. ◯名和憲嗣, 北岡幸恵, 中村浩次, 秋山亨, 伊藤智徳:
" 遷移金属メタロセン分子の多重項構造の第一原理計算"
日本物理学会第 69 回年次大会, 28pPSA-34, 湘南, 2014 年 3 月.

4. ◯名和憲嗣, 北岡幸恵, 中村浩次, 秋山亨, 伊藤智徳, 山田豊和:
" 電子配置制御による有機金属分子設計と磁性"
新学術領域研究分子アーキテクトニクス第 3 回領域会議, A03-10, 天童, 2014 年 6 月.

5. ◯名和憲嗣, 北岡幸恵, 中村浩次, 秋山亨, 伊藤智徳:
" 遷移金属メタロセン分子の電子配置と磁気異方性"
日本物理学会 2014 年秋季大会, 9pPSA-97, 春日井, 2014 年 9 月.

6. ◯ 池浦雄志, 名和憲嗣, 中村浩次, 秋山亨, 伊藤智徳:
" 希土類金属長薄膜の電子構造と磁性"
日本物理学会 2014 年秋季大会, 7pPSA-79, 春日井, 2014 年 9 月.

7. ◯ 竹田昌平, 名和憲嗣, 中村浩次, 佐野和博, 秋山亨, 伊藤智徳:
" 外部電場下における MoS_2 薄膜の電子構造とキャリア分布"
日本物理学会 2014 年秋季大会, 9aPS-61, 春日井, 2014 年 9 月.

8. ◯名和憲嗣:
” 全電子フルポテンシャル線形化補強平面波法による強相関電子系の有効オンサイトクーロン相互作用パラメータの導出”
第 2 回三重大学–大阪大学ジョイント研究会「第一原理計算による物質設計」, 近江八幡, 2014 年 10 月.

9. ◯ 中村浩次, 名和憲嗣, 北岡幸恵:
” 有機金属錯体の基底状態解析：拘束密度汎関数理論による d 軌道電子配置に関する再考”
元素戦略 CREST 合同研究会「物性理論と量子化学の接点 ∼ 相対論の視点を中心として」, 神戸, 2014 年 12 月.

10. ◯名和憲嗣, 北岡幸恵, 中村浩次, 秋山亨, 伊藤智徳:
” 有機金属分子における強相関効果と電子配置”
千葉大学テニュアトラック教員主催セミナー「単一分子が秘める新たな可能性 ∼ 持続可能社会実現へのキーマテリアル探索 ∼」, 千葉, 2015 年 3 月.

11. ◯ 北岡幸恵, 名和憲嗣, 中村浩次:
”Fe フタロシアニン分子における基底状態の電子構造と遷移”
千葉大学テニュアトラック教員主催セミナー「単一分子が秘める新たな可能性 ∼ 持続可能社会実現へのキーマテリアル探索 ∼」, 千葉, 2015 年 3 月.

12. ◯名和憲嗣, 中村浩次, 秋山亨, 伊藤智徳:
”FLAPW 法による有効オンサイトクーロン相互作用の第一原理計算と磁性材料の電子構造”
日本物理学会第 70 回年次大会, 21aPS-80, 高田馬場, 2015 年 3 月.

13. ◯ 池浦雄志, 名和憲嗣, 中村浩次, 秋山亨, 伊藤智徳:
” 希土類金属超薄膜における結晶磁気異方性の第一原理計算”
日本物理学会第 70 回年次大会, 21aPS-80, 高田馬場, 2015 年 3 月.

14. ◯ 竹田昌平, 名和憲嗣, 中村浩次, 佐野和博, 秋山亨, 伊藤智徳:
”WSe_2 薄膜におけるバレー構造の害ば効果に関する第一原理計算”
日本物理学会第 70 回年次大会, 21aPS-80, 高田馬場, 2015 年 3 月.

15. ◯名和憲嗣, 中村浩次, 秋山亨, 伊藤智徳:
” 有機金属分子メタロセン及びフタロシアニンの基底電子配置探索”
第 76 回応用物理学会秋季学術講演会, 15p-2N-17, 名古屋, 2015 年 9 月.

16. ◯名和憲嗣, 中村浩次, 秋山亨, 伊藤智徳:
” 遷移金属酸化物における有効オンサイトクーロン相互作用：拘束密度汎関数理論による再考”
日本物理学会 2015 年秋季大会, 19pCM-7, 吹田, 2015 年 9 月.

17. ◯ 池浦雄志, 名和憲嗣, 中村浩次, 秋山亨, 伊藤智徳:
” 希土類金属長薄膜における結晶磁気異方性の理論的予測”
日本物理学会 2015 年秋季大会, 19aCG-10, 吹田, 2015 年 9 月.

18. ◯ 竹田昌平, 名和憲嗣, 中村浩次, 佐野和博, 秋山亨, 伊藤智徳:
” 希土類金属長薄膜における結晶磁気異方性の理論的予測”
日本物理学会 2015 年秋季大会, 17pAH-5, 吹田, 2015 年 9 月.

19. ◯ 伊藤貴博, 名和憲嗣, 中村浩次, 秋山亨, 伊藤智徳, 小野輝男:
” 金属薄膜におけるスピンホール効果の第一原理計算”
日本物理学会 2015 年秋季大会, 16pPSA-20, 吹田, 2015 年 9 月.

20. ◯ 山本拳土, 名和憲嗣, 中村浩次, 秋山亨, 伊藤智徳, 小野輝男:
”Co/Pt(111) における界面構造と結晶磁気異方性”
日本物理学会 2015 年秋季大会, 16pPSA-10, 吹田, 2015 年 9 月.

21. ◯名和憲嗣, 池浦雄志, 中村浩次, 秋山亨, 伊藤智徳, 小口多美夫:
” 希土類金属超薄膜の結晶磁気異方性と基板効果”
科研費特別推進研究「スピンオービトロニクス」平成 27 年度報告会, 2-1, 小樽, 2016 年 2 月.

22. ◯ 伊藤貴博, 名和憲嗣, 中村浩次, 秋山亨, 伊藤智徳, 小野輝男:
” 非対称構造を有する金属多層膜のスピンホール効果”
科研費特別推進研究「スピンオービトロニクス」平成 27 年度報告会, 1-1, 小樽, 2016 年 2 月.

23. ◯ 山本拳土, 名和憲嗣, 中村浩次, 秋山亨, 伊藤智徳, 小野輝男:
”2 層膜における界面ジャロシンスキー・守谷相互力の第一原理計算”
科研費特別推進研究「スピンオービトロニクス」平成 27 年度報告会, 3-3, 小樽, 2016 年 2 月.

24. ◯名和憲嗣, 池浦雄志, 中村浩次, 秋山亨, 伊藤智徳, 小口多美夫:
” 希土類金属超薄膜における結晶磁気異方性の第一原理計算”
第 63 回応用物理学会春季学術講演会, 22a-W241-4, 大岡山, 2016 年 3 月.

25. ◯ 伊藤貴博, 名和憲嗣, 中村浩次, 秋山亨, 伊藤智徳, 小野輝男:
” 非対称構造を有する金属多層膜のスピンホール効果”
日本物理学会第 71 回年次大会, 19pPSB-29, 仙台, 2016 年 3 月.

26. ◯ 山本拳土, 名和憲嗣, 中村浩次, 秋山亨, 伊藤智徳, 小野輝男:
”2 層膜における界面ジャロシンスキー・守谷相互作用の第一原理計算”
日本物理学会第 71 回年次大会, 19pPSB-18, 仙台, 2016 年 3 月.

27. ◯名和憲嗣, 秋山亨, 伊藤智徳, 中村浩次:
” 希土類金属を活用した磁性制御と材料設計”
物質・デバイス領域研究拠点展開研究 B「次世代スピントロニクス材料の設計と開発」研究会, 仙台, 2016 年 8 月.

28. Kohji Nakamura, ◯Kenji Nawa, Toru Akiyama, Tomonori Ito:
”Electric field effect on magnetocrystalline anisotropy, exchange stiffness, and Dzyaloshinskii-Moriya interaction in magnetic metal thin films”
第 40 回日本磁気学会学術講演会, 06aA-12, 金沢, 2016 年 9 月.

29. ◯名和憲嗣, 秋山亨, 伊藤智徳, 中村浩次:
” 希土類金属における有効オンサイトクーロン相互作用の第一原理計算”
日本物理学会 2016 年秋季大会, 13pAP-12, 金沢, 2016 年 9 月.

30. ◯Abdul-Muizz Tri Pradipto, Kenji Nawa, Toru Akiyama, Tomonori Ito, Teruo Ono, Kohji Nakamura:
”Atomic layer thickness-dependence of electric field-induced modification to the magnetic and transport properties of Fe(001) films”
日本物理学会 2016 年秋季大会, 13PSA-41, 金沢, 2016 年 9 月.

31. ◯ 伊藤貴博, 名和憲嗣, Abdul-Muizz Tri Pradipto, 秋山亨, 伊藤智徳, 小野輝男, 中村浩次:
” 金属超格子膜のスピンホール効果に対する原子層配列の役割”
日本物理学会 2016 年秋季大会, 13pPSA-23, 金沢, 2016 年 9 月.

32. ◯ 山本拳土, 名和憲嗣, Abdul-Muizz Tri Pradipto, 秋山亨, 伊藤智徳, 小野輝男, 中村浩次:
”3d/5d 金属に二層膜における界面ジャロシンスキー・守谷相互作用力と軌道磁気モーメント”
日本物理学会 2016 年秋季大会, 15aAP-2, 金沢, 2016 年 9 月.

33. ◯ 野崎航平, 名和憲嗣, Abdul-Muizz Tri Pradipto, 秋山亨, 伊藤智徳, 小野輝男, 小口多美夫, 中村浩次:
”Fe 基遷移金属薄膜/MgO における原子層配列と磁気的性質の第一原理計算”
日本物理学会 2016 年秋季大会, 13pPSA-6, 金沢, 2016 年 9 月.

34. ◯ 野村昂宏, 名和憲嗣, Abdul-Muizz Tri Pradipto, 秋山亨, 伊藤智徳, 小野輝男, 中村浩次:
”3d/4d/5d 金属超薄膜における結晶磁気異方性と電界効果の第一原理計算”
日本物理学会 2016 年秋季大会, 15aAP-2, 金沢, 2016 年 9 月.

35. ◯名和憲嗣:
”Interfacial magnetocrystalline anisotropy in ultra-thin films of rare-earth metals”
環境エネルギー応用を目指した計算マテリアルデザイン研究会, 南紀勝浦, 2016 年 11 月.

36. ◯名和憲嗣, 中村浩次:
” 希土類金属の電子構造と磁性に関する第一原理計算”
物質・デバイス領域研究拠点展開研究 B 第 2 回「次世代スピントロニクス材料の設計と開発」研究会, 吹田, 2016 年 12 月.

37. ◯名和憲嗣, 中村浩次:
” 強相関電子系材料の理論的設計に向けた有効オンサイトクーロン相互作用の第一原理計算”
ナノテクイニシャティブ研究会「マテリアルズ・インフォマティクス・ネットワーク」, 神戸, 2017 年 1 月.

38. ◯ 伊藤貴博, Abdul-Muizz Tri Pradipto, 名和憲嗣, 秋山亨, 伊藤智徳, 中村浩次:
” 金属多層膜のスピンホール効果に関する原子層配列の役割”
スピンオービトロニクス特別推進研究会, 2-4, 小樽, 2017 年 2 月.

39. ◯ 山本拳土, Abdul-Muizz Tri Pradipto, 名和憲嗣, 秋山亨, 伊藤智徳, 中村浩次:
”3d/5d 金属薄膜における界面ジャロシンスキー・守谷相互作用の第一原理計算”
スピンオービトロニクス特別推進研究会, 2-5, 小樽, 2017 年 2 月.

40. ◯ 野崎航平, Abdul-Muizz Tri Pradipto, 名和憲嗣, 秋山亨, 伊藤智徳, 中村浩次:
” 遷移金属多層膜の磁気的性質と原子層配列の関係”
スピンオービトロニクス特別推進研究会, 2-6, 小樽, 2017 年 2 月.

41. ◯ 野村昂宏, Abdul-Muizz Tri Pradipto, 名和憲嗣, 秋山亨, 伊藤智徳, 中村浩次:
”Fe/MgO 界面磁気異方性に対する超薄膜挿入の効果”
スピンオービトロニクス特別推進研究会, 2-7, 小樽, 2017 年 2 月.

42. ◯名和憲嗣, 秋山亨, 伊藤智徳, 中村浩次:
” 希土類金属における有効オンサイトクーロン相互作用の第一原理的導出と電子構造”
日本物理学会第 72 回年次大会, 18aC41-11, 豊中, 2017 年 3 月.

43. ◯名和憲嗣:
” 次世代スピントロニクス材料の設計と第一原理計算手法の開発”
卓越型リサーチセンターキックオフシンポジウム「研究の探化と地域連携の創生」, 津, 2017 年 5 月.

44. ◯名和憲嗣, 中村浩次, 小口多美夫:
” 次世代スピンエレクトロニクスに向けた有機金属錯体材料の設計：第一原理計算によるアプローチ”
第 5 回アラアンス若手研究交流会 〜共同研究の輪を広げる〜, P-26, 横浜, 2017 年 8 月.